Call No.	BINDING INSTRUCTIONS	INTERLIBRARY INSTRUCTIONS
E9791 1993 583	Author: Williamson, Jr., R. Title: COLOR: M.S.	Dept. RUSH PERMABIND PAMPHLET GIFT POCKET FOR MAP COVERS Front Both REFERENCE Other
	Special Instructions - Bindery or Repair	
	1/20/95	

L-279

THE GEOLOGY OF THE MINERAL HILL AREA, MISSION MINE, PIMA COUNTY, ARIZONA

by

ROBERT LINN WILLIAMSON, JR.

A Thesis submitted to the Faculty of the
DEPARTMENT OF GEOSCIENCES
In partial fulfillment of the Requirements
For the Degree of
MASTER OF SCIENCE
IN GEOSCIENCES
In the Graduate College
UNIVERSITY OF ARIZONA

1 9 9 3

STATEMENT BY AUTHOR

This thesis has been submitted in partial fulfillment of requirements for an advanced degree at the University of Arizona and is deposited in the University Library to be made available to borrowers under rules of the Library.

Brief quotations from this thesis are allowable without special permission, provided that accurate acknowledgment of source is made. Requests for permission for extended quotation from or reproduction of this manuscript in whole or in part may be granted by the head of the major department or the Dean of the Graduate College when in his or her judgement the proposed use of the material is in the interests of scholarship. In all other instances, however, permission must be obtained from the author.

SIGNED: Robert P. Williamson

APPROVAL BY THESIS DIRECTOR

This thesis has been approved on the date shown below:

John M. Guilbert

Dr. John M. Guilbert
Professor of Geology

December 6, 1993
Date

ACKNOWLEDGMENTS

I wish to thank the management and staff of ASARCO Mission Unit for their funding and support. I would especially like to thank Bob Cummings, without whose support this study would not have been possible, as well as Bill Williams and Bob Smith for their help and excellent suggestions, Mac MacCauley and Heath Howe for computer support, and the men of the sample prep lab for their careful and precise workmanship in preparing my samples for analysis.

I would also like to thank my advisor, Dr. John Guilbert, for his help in defining this project, as well as his continual support as the project took shape, and for his always constructive critical review of my writing and work.

I wish to thank Dr. Mary Poulton, whose expertise and never ending helpfulness and support made the neural network analysis possible. Thanks also goes to my other committee members, Dr. Spence Titley and Dr. Mark Barton, for their review of this manuscript.

Last but certainly not least, I would like to thank my wife Jeannie for her constant encouragement and perpetual understanding through the long process of preparing this thesis.

TABLE OF CONTENTS

TABLE OF CONTENTS (CONT.)

LIST OF ILLUSTRATIONS

LIST OF ILLUSTRATIONS (CONT.)

LIST OF TABLES

ABSTRACT

THE GEOLOGY OF THE MINERAL HILL AREA, MISSION MINE, PIMA COUNTY, ARIZONA

Robert Linn Williamson, Jr.

The University of Arizona, 1993

Director: Dr. John M. Guilbert

The Mission Mine, 32 kilometers southwest of Tucson, Arizona, is developed on a porphyry copper skarn with ore hosted in the Permian Epitaph, Scherrer, and Concha Formations and the Triassic Rodolfo Formation. The western portion of the orebody, the Mineral Hill area, has distinct geologic and structural differences from the Mission pit sequence. Cross-sections constructed from recent drill hole data revealed that three major faults are responsible for the differing geology and stratigraphy. Two of these cause carbonate rocks whose formation identity was previously unknown to be emplaced in the project area. Geochemical analysis of known carbonate formations and of the unknown carbonates was used to attempt classification of the unknowns by determining normative mineral compositions, and by using neural networks, a computer algorithm previously successful in classifying complex patterns. The normative mineral compositions were too similar to be useful, but neural networks were moderately successful

in correctly classifying unknowns whose formation name could be deduced by stratigraphic means. Sections of the Cambrian Abrigo, Devonian Martin, and Permian Rainvalley Formations, previously unrecognized at Mission, were identified by neural network and stratigraphic data.

INTRODUCTION

The Mission mine is located in the Pima mining district approximately 32 kilometers southwest of Tucson, Arizona, on the eastern pediment of the Sierrita mountains. The mine is developed in a sediment-hosted porphyry copper skarn orebody in a sequence of Permian and Triassic sediments striking E-NE and dipping southeasterly that are intruded by a Tertiary (Laramide) quartz monzonite porphyry. The Upper Permian limestones, dolomites, and sandstones have been altered to marble, calc-silicate skarn, and quartzite. The overlying Triassic clastic sediments have undergone recrystallization and some hydrothermal alteration. The porphyry stock has undergone potassium-silicate and sericitic alteration. The general geology and stratigraphy of the Mission-Pima orebody is well known, having been studied by a series of authors (Jansen, 1982).

History and Production

The Pima mining district has had a long history of production, beginning in the late 1700's when the Spaniards were known to have operated several small mines there. Intermittent production from several small underground mines, notably the Daisy, Palo Verde, and San Xavier, continued through the 1940's. In 1950, geophysical work conducted by

R.E. Thurmond and W.E. Heinrichs, Jr. of the United Geophysical Company led to the discovery of the Pima orebody to the south of what would later be discovered as the Mission orebody. Subsequent geologic analysis by Kenyon Richard and J. Harold Courtwright of American Smelting and Refining Co. (ASARCO) led to the discovery of the Mission orebody in the late 1950s. The Pima Mining Company (Cyprus Mines, Union Oil, and Utah Construction and Mining Company) commenced open pit mining on the Pima orebody in 1955, and ASARCO began mining operations on the Mission orebody in 1959. By the early 1960's, it had become apparent to workers that the Pima and Mission mines were operating on one continuous orebody. Four organizationally separate mines formerly operated on this orebody, the Pima, Mission, Palo Verde, and San Xavier South, but since the mid-1980s they have been acquired and integrated into one large open pit operation, the Mission Complex operated by ASARCO Inc.

Combined production to date has been approximately 514 million tons at an average grade of 0.62 % Cu. Currently ASARCO is producing approximately 60,000 tons per day at an average grade of 0.65 % Cu.

Statement of Problem

The western portion of the orebody, informally known as the Mineral Hill area (Fig. 1), does not appear to involve the

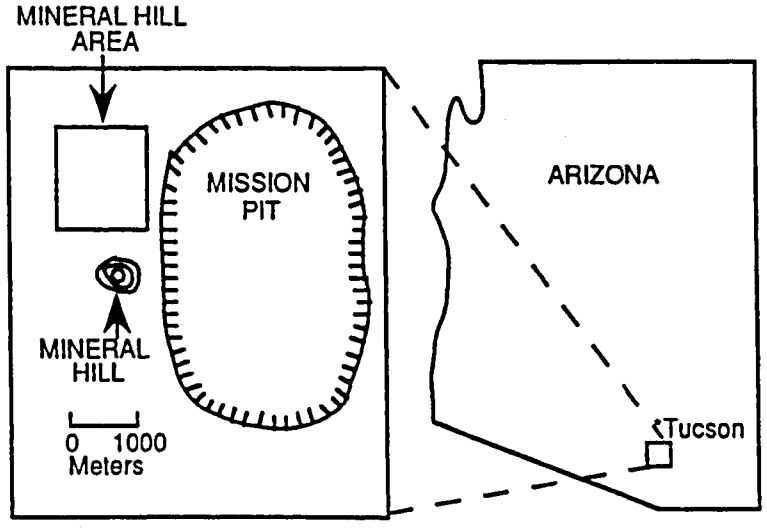

Figure 1. Location of Mineral Hill project area in relation to Mission pit

same stratigraphic succession found in the Mission pit proper. This discrepancy is a result of two things: (1) disruption caused by the intrusion of Laramide quartz monzonite porphyry into the Paleozoic sequence, and (2) post-intrusive block movements on several NW-trending high-angle normal faults, as well as faulting associated with the transport of the orebody ten kilometers northward along the Tertiary San Xavier thrust fault (Cooper, 1960). The identity of some of the Paleozoic carbonate units west of the high-angle normal faults has been unknown to past workers due to lack of surface outcrop and drill hole data and to the effects of metamorphism on the rocks. The non-carbonate rocks are generally distinctive enough to be recognizable from drill core within the project area. The purpose of this study has been to identify the obscured units and to delineate the structure and stratigraphy of the Mineral Hill area, as well as to determine the validity of some of the methods used for such identifications.

The major ore-bearing units to the east of one of the high-

angle structures, the Concha, Scherrer, and Epitaph Formations, have been displaced on the west side as a result of the faulting. Identification of the unknown units to the west may allow an approximation of the amount of displacement along the fault and possibly give some insight to ASARCO geologists as to the location of these ore bearing units west of the fault, if in fact they still exist. Also, it has been suggested by past workers that this structure, the Daisy fault (Figs. 21, 24-27, 31), may be the upsection continuation of the Twin Buttes fault, which breaks up the Paleozoic section in the western portion of the Twin Buttes mine ten kilometers to the south. Barter and Kelly (1982) estimate a minimum displacement of 1067 meters (3500 feet) along the Twin Buttes fault. Identification of units to the west of the Daisy fault may allow an estimate of displacement along the Daisy and therefore strengthen or refute the suggestion of correlation of these two faults.

A literature search revealed that whole-rock geochemical analyses have never been published on the southern Arizona Paleozoic carbonate section, and new data reported here may prove valuable for future research. Using this data in a neural network analysis to attempt to classify the formations geochemically is an application never previously attempted, and the success of this venture should prove instructive for future neural network and stratigraphic researchers.

Method of treatment

The problem of identification and delineation of the otherwise unrecognizable Paleozoic meta-carbonate units was addressed using two methods in conjunction: (1) by using recent extensive drill-hole data to construct cross-sections and level maps, and (2) by using whole-rock geochemistry to attempt to identify the major stratigraphic units.

In an effort to delineate ore reserves and assist in mine planning, the ASARCO Mission Unit has during the last several years drilled many vertical holes in the Mineral Hill area. Logging by the author of approximately 4300 meters of reverse-circulation chips and 2000 meters of diamond-drill core, considered with approximately 3000 meters of older drill hole logs by previous workers, allowed the construction of an extensive series of N-S and E-W cross-sections set 61 meters apart (Fig. 2). Level or plan maps were subsequently constructed using the cross-section data. The geochemical survey consisted of taking samples from outcrop of 9 carbonate units known in the area, the Abrigo, Martin, Escabrosa, Horquilla, Colina, Epitaph, Scherrer, Concha, and Rainvalley Formations (Fig.3), as well as samples within the Mission pit

Figure 2

CROSS-SECTION AND DRILL HOLE LOCATIONS MINERAL HILL AREA, MISSION MINE

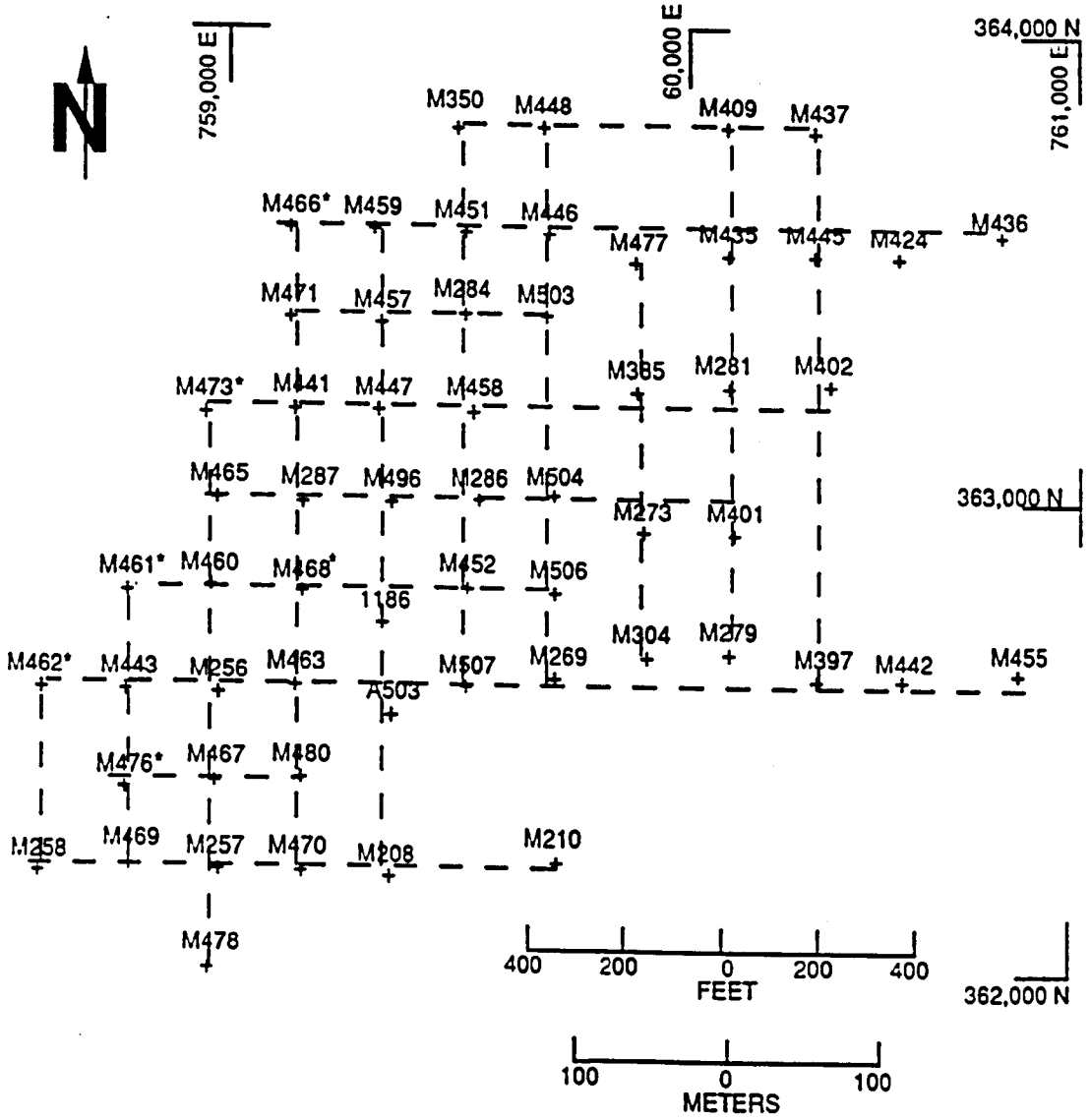

EXPLANATION

+ DRILL HOLE LOCATIONS (NUMBERED ACCORDING TO MISSION SCHEME)

* GEOCHEMICAL ASSAYS FOR NEURAL NETWORKS

— — CROSS-SECTION LOCATIONS

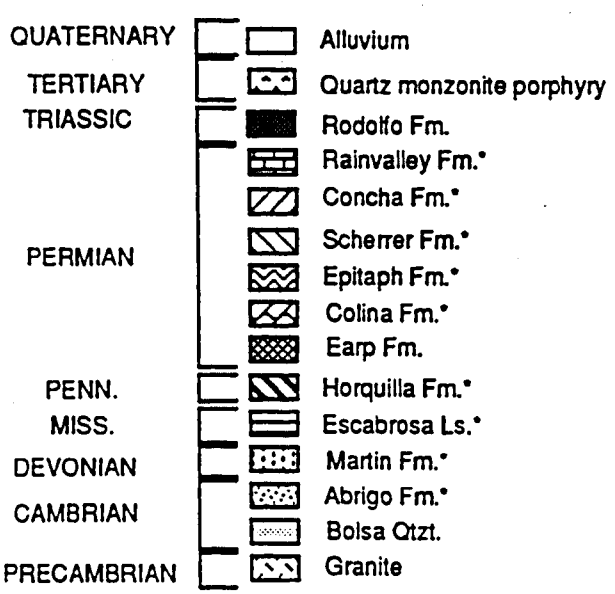

Figure 3. Stratigraphic column of rocks known in Mission area

* Formations sampled for geochemical study

and unknowns from drill core within the project area. A total of 80 samples were analyzed for 51 elements by four independent means, and classification by formation was attempted by two means, first using Sednorm, a program to calculate normative mineralogy for sedimentary rocks based on chemical analyses (Cohen and Ward, 1991), and secondly by using neural networks, a category of computer algorithms that has been shown to be successful in classification of complex patterns elsewhere. The classification that the neural network gave to the unknowns was then used in conjunction with the stratigraphic data to determine the identity of specific units and to determine the validity of the neural network classifications, particularly where other clues to the identity of a particular unit exist.

SUMMARY OF THE GENERAL GEOLOGY OF THE MISSION-PIMA OREBODY

The general geology and stratigraphy of the Mission orebody have been studied many times since its discovery in the mid-1950's, and the following is only a brief summary. Readers

desiring a more detailed description of individual rock unit characteristics and mine stratigraphy and structure are directed to Jansen (1982).

The Mission orebody is now recognized as being allocthonous, having been displaced by low-angle faulting and moved 10 kilometers northward, as first suggested by Cooper (1960). The orebody occurs in an overturned sequence of upper Paleozoic (Permian) metasedimentary strata that lie in fault contact with granitoid rocks presumed to be Laramide (early Tertiary) in age. The Paleozoic strata, which consist of the Epitaph, Concha, and Scherrer Formations, are in turn overlain on an angular unconformity by Triassic clastic rocks assigned by Himes (1973) to the Rodolfo formation. The Paleozoic sequence has been deformed into broad, gentle, NW-trending folds. On the western side of the Mission orebody is a sill-like intrusion of quartz monzonite porphyry of Laramide age (c.a. 58 m.y.) (Shafiqullah and Langlois, 1978).

Figure 4 shows a stratigraphic column of the original sedimentary rocks and their generalized metamorphic equivalents at Mission. The vast majority (90-95 percent) of mineralization occurs in the altered sediments rather than in the quartz monzonite porphyry. The mineralization is hypogene sulfide, primarily chalcopyrite with minor bornite. Minor amounts of "oxide" ores, primarily chrysocolla with minor malachite, azurite, and tenorite, occur

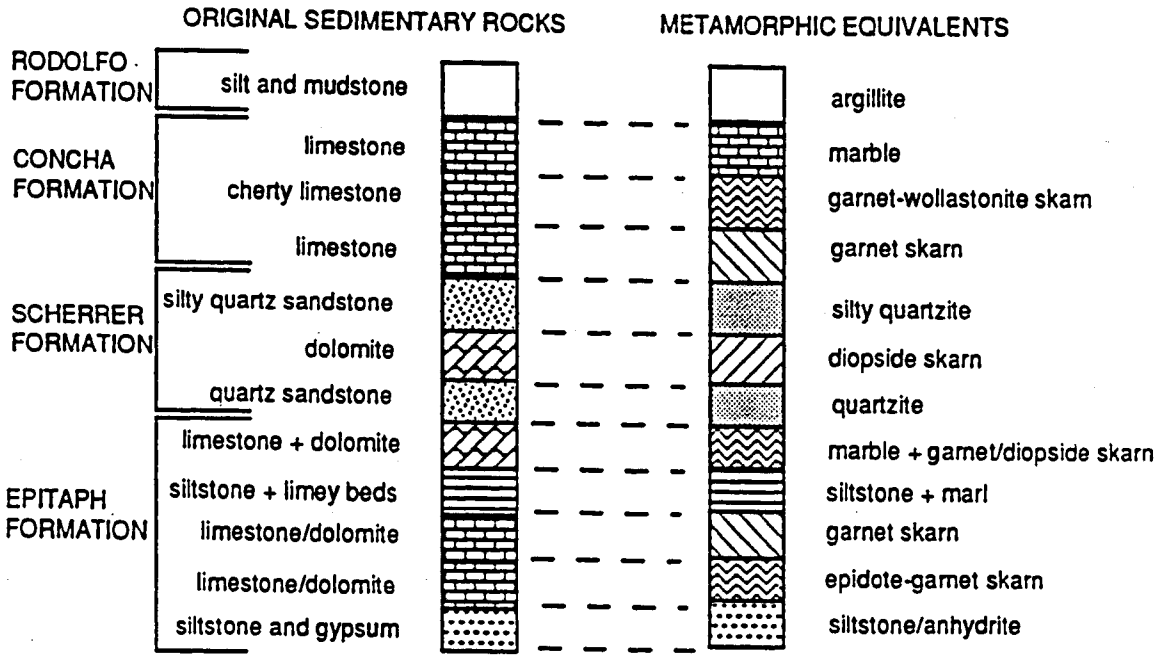

Figure 4. Stratigraphic column of original sedimentary rocks and their metamorphic equivalents at Mission

in the upper 60-70 meters of the orebody directly below the alluvium, but this "oxide" ore is not being processed by ASARCO at this time.

EPITAPH FORMATION

Approximately 75 meters of thickness of the Epitaph formation is present in the overturned Mission mine sequence, compared to 225 meters in the type section in central Cochise County, Arizona. The section bears little resemblance to the type section, due to lateral variation in the composition of the formation and the effects of metamorphism. The principal basis of correlation is the presence, within the unit at

Mission, of beds of anhydrite that are unique in the upper Paleozoic to the Epitaph formation (Jansen, 1982).

The youngest, topographically lowest unit is 15 to 20 meters of anhydrite interbedded with siltstone, followed by 7 to 10 meters of green-brown epidote-garnet skarn. The next higher (older) unit consists of 5 to 11 meters of light brown garnet skarn. Above is about 22 meters of light to dark green siltstone and marl. Within this unit carbonates are locally silicated to light brown garnet. The oldest, topographically highest unit is 11 to 22 meters of brown garnet skarn mixed with marble. Locally within the carbonate units, dolomitic beds are altered to light to dark green diopside ($CaMgSi_2O_6$) rather than the grossularite-andradite series ($Ca_3Al_2(SiO_4)_3$)-($Ca_3Fe_2(SiO_4)_3$) garnet that replaced limestone (Gale, 1965). The altered carbonate units generally contain ore-grade sulfides.

SCHERRER FORMATION

Within the Mission mine, the Scherrer formation consists of an upper (older), light-colored orthoquartzite unit up to 50 meters thick, a 10 to 20 meter-thick middle dolomite unit altered to light to dark green fine-grained diopside, and a lower (younger) 10 to 20 meter-thick unit of grey to brown quartzite, which is sometimes absent. The upper contact with the older Epitaph formation is commonly faulted, but exposures

in the east-central part of the mine show stratigraphic contacts (Jansen, 1982). The diopside commonly contains ore-grade disseminated chalcopyrite.

CONCHA FORMATION

The thickness of the Concha formation at Mission (Fig. 4) is 150 to 170 meters, about that measured from the type locality in Cochise County. Mesozoic erosion and thinning that affected both the Epitaph and Scherrer formations did not affect the Concha due to its topographically lower position. The upper 25-50 meters is green garnet of grossularite-andradite composition (Gale, 1965). The lower part of the formation is variously altered thick-bedded marble with zones of wollastonite ($CaSiO_3$)-garnet, probably originally chert beds within the limestone. The Concha formation is an important ore-bearing formation at Mission, with zones of disseminated to massive chalcopyrite-bornite in the garnet and garnet-wollastonite skarns.

RODOLFO FORMATION

Himes (1973) proposed that the siliceous argillites, arkose, and local basal pebble conglomerates which lie above the Paleozoic metasediments on an angular unconformity belong to the middle siltstone member of the Triassic Rodolfo Formation described by Cooper (1971). This formation is also

an important host to sulfide ore, usually fracture-controlled chalcopyrite, although generally at a lower ore grade than the Paleozoic rocks. Notable within the Rodolfo Formation at Mission are pods of hydrothermally altered epidote skarn, usually containing higher-grade ore than the surrounding argillite.

QUARTZ MONZONITE PORPHYRY

Gale (1965) describes the quartz monzonite at Mission as being typical of porphyry copper plutons. It consists of subhedral phenocrysts of 30 percent plagioclase, 10 percent orthoclase, 5 percent biotite, and 1-2 percent quartz in a sub-graphic, fine-grained K-feldspar-quartz groundmass. The porphyry stock is ubiquitously potassium-silicate altered and weakly sericitized with no apparent alteration zoning. Weak silicification also occurs, particularly in areas where extensive quartz veining exists.

Barter and Kelly (1982) describe three types of quartz monzonite porphyry at Twin Buttes, 10 kilometers to the south, namely xenolithic, aphanitic, and aplitic types. Their descriptions are somewhat sketchy, but the porphyry at Mission most closely resembles their description of the aplitic type. Plagioclase phenocrysts have been pervasively replaced by sericite, generally with visible remnant texture. K-feldspar phenocrysts remain fresh. Biotite phenocrysts may be either

unaltered, weakly sericitized, or chloritized, commonly showing chlorite alteration rims around fresh biotite. Biotite phenocrysts are generally either sericitized or chloritized within a single sample, although fresh and altered biotite phenocrysts do occur within a single sample. Quartz veinlets, barren or with pyrite-chalcopyrite, average 1-2 volume percent of the rock. Commonly potassic alteration haloes exist around the veinlets, with secondary K-feldspar much greater than secondary biotite, with silicification increased in areas where veinlets greater than 5-10 mm. wide exist. Thin gypsum veinlets, less than 5 mm. wide, occur randomly in volumes up to 1-2 percent. Gale (1965) estimated pyrite-chalcopyrite ratios at 3:2 to 3:1. Only rarely does chalcopyrite concentration exceed 1.0 volume percent, usually averaging 0.15-0.3 percent copper. Molybdenite seemingly occurs randomly in minor concentrations at an average of less than 0.15 percent Mo associated with quartz veinlets or as "paint" on fractures.

Overall, rock type, alteration, copper grade, and sulfide ratios at Mission are similar to the porphyry stock complex at Twin Buttes (Einaudi, 1982).

GEOLOGY OF THE PALEOZOIC CARBONATE UNITS

Nine Paleozoic carbonate units known to exist in the Pima district (Fig. 3) were analyzed for the Sednorm (Cohen and

Ward, 1991) and neural network studies. Following is a summary of the stratigraphy of these units, listed by decreasing age, information on the sampling for this study, and whole-rock geochemical analyses used in the Sednorm and neural network studies. Please refer to Figs. 3 and 4.

ABRIGO FORMATION

The Cambrian Abrigo formation, named by Ransome (1904), is a carbonate-dominated sequence. The type section of the Abrigo in the Mule Mountains near Bisbee, Arizona was remeasured by Hayes and Landis (1965) and subdivided into four members. These, in ascending order, are a lower siliciclastic mudstone, a middle siliciclastic-carbonate sequence, an upper dolomitic sandstone and sandy dolostone, and locally uppermost Copper Queen limestone.

The lower member is late Middle Cambrian and is from 70 to 200 meters thick (Hayes, 1978). It consists of interbedded bioturbated silty shale and limestone in the south grading into siltstone and fine-grained sandstone to the north (Hayes and Cone, 1975). Several localities commonly feature cross-stratification and trace fossils. Carbonate facies include intraformational conglomerate, algal grainstone, peloidal packstone, and rare mudcracked wackestone (Hayes and Cone, 1975).

The middle member is 42 to 94 meters thick, although it is

absent in many areas due to post-Cambrian erosion (Hayes, 1978). This member consists of thin-bedded limestone and dolomitic limestone in the south, grading into sandstone and dolostone northward. At the northern limit of its exposure the member is a fine grained quartz arenite (Hayes and Cone, 1975). Intraformational limestone conglomerate and mudcracked carbonate mudstone are common (Hayes, 1978).

The upper sandy member is late Cambrian and varies from 30 to 55 meters thick. To the east, the sandy member grades into the Coronado sandstone. This member consists of dolomitic sandstone and sandy dolostone, with dolomite increasing towards the south and west (Hayes and Cone, 1975). Limestones, typically grainstones and packstones, are rare.

The Late Cambrian Copper Queen limestone member gradationally overlies the upper sandy member, and is present only in easternmost Arizona, where it is up to 45 meters thick. At the type section it consists of thinly bedded, sandy to silty limestone (Hayes and Cone, 1975). Elsewhere, it is a sandy dolostone.

Sampling and Analysis

The Abrigo formation samples collected for analysis are from an unnamed hill approximately 300 meters west of Mineral Hill where approximately 80 meters of the middle siliciclastic-carbonate member outcrops. At this location as well as on Mineral Hill where the Martin, Escabrosa, and

Horquilla Formation samples were collected, the rocks have undergone thermal metamorphism but are still recognizable by formation and hopefully are still geochemically representative of the original sedimentary rocks. The samples were collected upwards through the section perpendicular to bedding at intervals of 10 to 20 meters, depending on availability of carbonate beds to sample. All samples were collected in the carbonate beds rather than the clastics for the purposes of this study. In the project area clastics are generally identifiable by unit from hand sample, while the carbonates are more problematic, and the objective of the neural network and sednorm studies was to identify the carbonates. The samples collected were large enough for two hand sample suites plus the 20 kg. required for analysis.

Table 1 shows the analyses of the five Abrigo samples. All results are in parts per million (ppm) unless specified otherwise, except for the INAA gold (Au) assays, which are in parts per billion. For the purpose of averaging as well as for the neural networks study, one-half of the detection limit was used instead of zero where the analysis was below the detection limit. Also, since the XRF analyses reported values of common elements as oxides, assays of these elements by ICP and INAA have been converted to oxides for standardization of reporting and for use in the neural networks study.

TABLE 1
WHOLE-ROCK GEOCHEMICAL ANALYSES - ABRIGO FORMATION

ANALYSIS	SMPL. 1	SMPL. 2	SMPL. 3	SMPL. 4	SMPL.5	AVG.
ICP Ag	0.6	<0.1	<0.1	0.2	<0.1	0.19
ICP Al_2O_3	1.44 %	0.26 %	0.26 %	1.13 %	0.74 %	0.77 %
ICP As	<3.0	<3.0	<3.0	4.0	6.0	2.9
ICP Ba	10	44	33	18	65	34
ICP Be	0.9	<0.5	<0.5	<0.5	<0.5	0.38
ICP Bi	<3.0	<3.0	<3.0	<3.0	<3.0	<3.0
ICP Cd	<1.0	<1.0	<1.0	<1.0	<1.0	<1.0
ICP Co	<1.0	<1.0	<1.0	<1.0	<1.0	<1.0
ICP Cr	39	6	10	19	15	17.8
ICP Cu	8.7	15.3	28.0	15.9	153.0	44.18
ICP Fe_2O_3	0.67 %	0.11 %	0.13 %	0.74 %	0.49 %	0.43 %
ICP K_2O	0.11 %	0.084 %	0.024 %	0.084 %	0.29 %	0.12 %
ICP Li	8.0	1.0	1.0	11.0	5.0	5.2
ICP MgO	3.15 %	0.40 %	0.50 %	3.32 %	1.23 %	1.72 %
ICP MnO	0.30 %	0.05 %	0.05 %	0.09 %	0.08 %	0.11 %
ICP Mo	2.0	1.0	<1.0	1.0	<1.0	1.0
ICP Na_2O	0.41 %	0.04 %	0.03 %	0.04 %	0.09 %	0.12 %
ICP Ni	11.0	2.0	<1.0	6.0	4.0	4.7
ICP P_2O_5	0.09 %	0.02 %	0.02 %	0.09 %	<.02 %	0.04 %
ICP Pb	93.0	9.0	10.0	4.0	3.0	23.8
ICP Sb	<5.0	<5.0	<5.0	<5.0	<5.0	<5.0
ICP Sc	1.5	<0.5	<0.5	1.5	0.8	0.46
ICP Sn	<10.0	<10.0	<10.0	<10.0	<10.0	<10.0
ICP Sr	185.0	404.0	555.0	455.0	878.0	495.4
ICP TiO_2	0.10 %	0.02 %	0.02 %	0.10 %	0.03 %	0.05 %
ICP V	22.0	13.0	6.0	21.0	13.0	15.0
ICP W	20.0	<10.0	<10.0	<10.0	<10.0	8.0

TABLE 1 (CONT.)
WHOLE-ROCK GEOCHEMICAL ANALYSES - ABRIGO FORMATION

ANALYSIS	SAMPLE 1	SAMPLE 2	SAMPLE 3	SAMPLE 4	SAMPLE 5	AVERAGE
ICP Y	8.5	8.3	3.6	8.8	5.1	6.9
ICP Zn	270.0	15.0	14.0	61.0	180.0	108.0
ICP Zr	7.5	3.1	4.0	13.0	4.9	6.5
INAA Ag	<5.0	<5.0	<5.0	<5.0	<5.0	<5.0
INAA As	7.0	2.0	4.0	11.0	6.0	5.8
INAA Au	<5.0	<5.0	<5.0	<5.0	<5.0	<5.0
INAA Ba	<100.0	<100.0	<100.0	<100.0	<100.0	<100.0
INAA Br	<1.0	<1.0	<1.0	<1.0	1.0	0.6
INAA CaO	42.0 %	53.2 %	53.2 %	46.2 %	46.2 %	48.2 %
INAA Co	<5.0	<5.0	<5.0	<5.0	<5.0	<5.0
INAA Cr	40.0	10.0	10.0	20.0	10.0	18.0
INAA Cs	<3.0	<3.0	<3.0	<3.0	<3.0	<3.0
INAA Fe_2O_3	0.86 %	0.14 %	0.14 %	0.86 %	0.57 %	0.51 %
INAA Hf	2.0	<1.0	<1.0	2.0	1.0	1.2
INAA Mo	<5.0	<5.0	<5.0	<5.0	<5.0	<5.0
INAA Na_2O	4725	<675	<675	<675	945	1336.5
INAA Ni	<100	<100	<100	<100	<100	<100
INAA Rb	<30.0	<30.0	<30.0	<30.0	<30.0	<30.0
INAA Sb	1.5	0.2	0.4	1.2	1.0	0.86
INAA Sc	1.9	0.5	0.3	1.8	0.9	1.08
INAA Se	<5.0	<5.0	<5.0	<5.0	<5.0	<5.0
INAA Sr	<500.0	<500.0	500.0	700.0	1000.0	540.0
INAA Ta	<1.0	<1.0	<1.0	<1.0	<1.0	<1.0
INAA Th	1.9	0.6	0.5	1.8	0.9	1.14
INAA U	2.1	1.0	2.1	1.7	1.0	1.58
INAA W	21.0	<4.0	<4.0	5.0	13.0	8.6
INAA Zn	270.0	<50.0	<50.0	60.0	200.0	116.0

TABLE 1 (CONT.)
WHOLE-ROCK GEOCHEMICAL ANALYSES - ABRIGO FORMATION

ANALYSIS	SMPL.1	SMPL.2	SMPL.3	SMPL.4	SMPL.5	AVERAGE
INAA La	8.0	12.0	3.0	11.0	6.0	8.0
INAA Ce	9.0	20.0	5.0	20.0	10.0	12.8
INAA Nd	<10.0	10.0	<10.0	10.0	<10.0	6.0
INAA Sm	1.4	1.7	<0.5	1.8	0.9	1.41
INAA Eu	0.4	0.3	0.3	0.5	0.4	0.38
INAA Tb	<0.5	<0.5	<0.5	<0.5	<0.5	<0.5
INAA Yb	0.7	0.5	0.2	0.8	0.4	0.52
INAA Lu	0.10	0.08	<0.05	0.11	0.06	0.075
INAA Ir	<20	<20	<20	<20	<20	<20
XRF1 SiO_2	22.3 %	2.79 %	4.71 %	12.0 %	7.74 %	9.91 %
XRF1 Al_2O_3	1.54 %	0.33 %	0.29 %	1.37 %	0.74 %	0.85 %
XRF1 Fe_2O_3	0.80 %	0.11 %	0.13 %	0.86 %	0.51 %	0.48 %
XRF1 CaO	41.3 %	54.2 %	53.3 %	45.7 %	49.2 %	48.7 %
XRF1 MgO	3.88 %	0.25 %	0.32 %	3.89 %	1.05 %	1.88 %
XRF1 Na_2O	0.10 %	0.15 %	0.15 %	0.15 %	0.13 %	0.14 %
XRF1 K_2O	0.12 %	0.13 %	0.07 %	0.11 %	0.32 %	0.15 %
XRF1 TiO_2	0.15 %	0.04 %	0.03 %	0.15 %	0.07 %	0.09 %
XRF1 P_2O_5	0.10 %	0.06 %	0.06 %	0.11 %	0.04 %	0.07 %
XRF1 SO_3	0.02 %	0.02 %	0.02 %	0.02 %	0.03 %	0.02 %
XRF2 Cu	0.06 %	0.04 %	0.02 %	0.06 %	0.07 %	0.05 %
XRF2 Mo	.001 %	.003 %	.003 %	.002 %	.002 %	.002 %
XRF2 Fe_2O_3	0.29 %	.001 %	.001 %	0.43 %	0.14 %	0.17 %
XRF2 Zn	0.12 %	0.06 %	0.04 %	0.08 %	0.10 %	0.08 %
XRF2 Al_2O_3	0.80 %	.001 %	.001 %	1.0 %	0.60 %	0.48 %
XRF2 SiO_2	21.5 %	5.80 %	7.90 %	15.5 %	11.0 %	12.3 %
XRF2 CaO	40.9 %	54.1 %	52.8 %	44.6 %	48.9 %	48.3 %
XRF2 SO_3	<0.01	<0.01	<0.01	<0.01	<0.01	<0.01

MARTIN FORMATION

The Devonian Martin formation, the most widely recognized Devonian unit in Arizona, was originally named the Martin Limestone from a predominantly limestone and dolomite sequence in the Bisbee area of southeast Arizona by Ransome (1904). Teichert (1965) defined two members of the Martin formation: a thin basal Beckers Butte member and the overlying Jerome member, which constitutes most of the formation.

The Beckers Butte member is a thin sequence of quartz sandstone to granule conglomerate with minor dolomite and shale at the base of the Martin formation. It is up to 40 meters thick and rests unconformably on Precambrian or Cambrian rocks in central and southern Arizona.

The Jerome member, named for the type section in Jerome, Arizona, is generally between 75 and 140 meters thick. Three units or informal members are recognized in the Jerome member. The lower unit is a fine-grained dark-gray fetid dolomite mudstone up to 12 meters thick. The middle unit is a distinctive light-gray aphanitic dolomitic mudstone up to 55 meters thick. A marker bed up to two meters thick of reddish-brown sandstone or sandy dolomite occurs locally near the top. The upper unit is the thickest part of the member, being up to 96 meters. This unit is gray to brownish-gray dolomite or limestone, having a skeletal wackestone or packstone texture.

Sampling and Analysis

The Martin Formation samples collected for analysis are from the western side of Mineral Hill, where approximately 50 meters of the lower and middle units of the Jerome member outcrop. The samples were collected perpendicular to bedding downwards through the section at approximately 10 meter intervals, beginning just below the disconformable Martin-Escabrosa contact. Table 2 shows the analyses of the five Martin samples.

TABLE 2
WHOLE-ROCK GEOCHEMICAL ANALYSES - MARTIN FORMATION

ANALYSIS	SMPL. 1	SMPL. 2	SMPL.3	SMPL.4	SMPL. 5	AVG.
ICP Ag	<0.1	<0.1	<0.1	<0.1	<0.1	0.05
ICP Al_2O_3	0.075 %	1.68 %	3.44 %	1.74 %	0.32 %	1.45 %
ICP As	6.0	<3.0	<3.0	<3.0	11.0	4.3
ICP Ba	5.0	15.0	62.0	22.0	9.0	22.6
ICP Be	<0.5	<0.5	1.5	<0.5	<0.5	0.5
ICP Bi	<3.0	<3.0	<3.0	<3.0	<3.0	1.5
ICP Cd	<1.0	<1.0	<1.0	<1.0	<1.0	0.5
ICP Co	<1.0	<1.0	<1.0	<1 0	<1.0	0.5
ICP Cr	3.0	11.0	16.0	9.0	3.0	8.4
ICP Cu	12.2	20.8	11.6	27.0	22.6	18.8
ICP Fe_2O_3	0.23 %	0.63 %	1.47 %	1.10 %	0.2 %	0.73 %
ICP K_2O	0.012 %	0.072 %	1.68 %	0.25 %	0.084 %	0.42 %
ICP Li	2.0	3.0	13.0	5.0	3.0	5.2
ICP MgO	16.4 %	13.1 %	15.6 %	12.8 %	1.53 %	11.9 %
ICP MnO	0.013 %	0.065 %	0.04 %	.065 %	0.013 %	0.04 %
ICP Mo	2.0	9.0	2.0	3.0	2.0	3.6
ICP Na_2O	0.014 %	0.014 %	0.09 %	0.03 %	0.03 %	0.04 %
ICP Ni	1.0	5.0	8.0	4.0	3.0	4.2
ICP P_2O_5	<0.02 %	0.02 %	0.07 %	0.05 %	<0.02 %	0.03 %
ICP Pb	<2.0	3.0	<2.0	6.0	4.0	3.0
ICP Sb	<5.0	<5.0	<5.0	<5.0	<5.0	2.5
ICP Sc	<0.5	2.0	3.4	1.9	<0.5	1.6
ICP Sn	<10.0	<10.0	<10.0	<10.0	<10.0	<10.0
ICP Sr	83.6	162.0	98.3	177.0	268.0	157.8
ICP TiO_2	<0.02 %	0.10 %	0.15 %	0.08 %	<0.02 %	0.07 %
ICP V	6.0	13.0	35.0	26.0	8.0	17.6
ICP W	<10.0	<10.0	<10.0	<10.0	<10.0	<10.0

TABLE 2 (CONT.)
WHOLE-ROCK GEOCHEMICAL ANALYSES - MARTIN FORMATION

ANALYSIS	SAMPLE 1	SAMPLE 2	SAMPLE 3	SAMPLE 4	SAMPLE 5	AVERAGE
ICP Y	0.5	10.0	8.9	6.8	1.3	5.5
ICP Zn	25.0	37.0	7.2	39.0	12.0	24.0
ICP Zr	1.5	32.0	15.0	20.0	3.8	14.5
INAA Ag	<5.0	<5.0	<5.0	<5.0	<5.0	<5.0
INAA As	3.0	5.0	2.0	2.0	8.0	4.0
INAA Au	<5.0	<5.0	<5.0	<5.0	<5.0	<5.0
INAA Ba	<100	<100	<100	100	<100	60.0
INAA Br	<1.0	1.0	<1.0	<1.0	1.0	0.7
INAA CaO	35.0 %	33.6 %	26.6 %	37.8 %	53.2 %	44.2 %
INAA Co	<5.0	<5.0	<5.0	<5.0	<5.0	<5.0
INAA Cr	<10	10.0	20.0	10.0	<10	10.0
INAA Cs	<3.0	<3.0	12.0	3.0	<3.0	3.9
INAA Fe_2O_3	0.29 %	0.86 %	1.72 %	1.43 %	0.29 %	0.92 %
INAA Hf	0.5	1.0	1.0	1.0	0.5	0.8
INAA Mo	<5.0	7.0	<5.0	<5.0	<5.0	3.4
INAA Na_2O	<675	<675	1080	<675	<675	486.0
INAA Ni	<100	<100	<100	100	<100	60.0
INAA Rb	<30	<30	70	<30	<30	26.0
INAA Sb	0.2	<0.2	0.3	0.2	0.3	0.22
INAA Sc	0.1	2.3	3.9	2.3	0.4	1.8
INAA Se	<5.0	<5.0	<5.0	<5.0	<5.0	<5.0
INAA Sr	<500	<500	<500	<500	<500	<500
INAA Ta	<1.0	<1.0	<1.0	<1.0	<1.0	<1.0
INAA Th	<0.5	2.3	3.4	1.9	<0.5	1.62
INAA U	<0.5	2.5	3.7	3.1	0.7	2.05
INAA W	<4.0	9.0	<4.0	7.0	<4.0	4.4
INAA Zn	<50.0	50.0	<50.0	60.0	<50.0	37.0

TABLE 2 (CONT.)
WHOLE-ROCK GEOCHEMICAL ANALYSES - MARTIN FORMATION

ANALYSIS	SMPL.1	SMPL. 2	SMPL.3	SMPL.4	SMPL.5	AVERAGE
INAA La	<1.0	12.0	10.0	9.0	2.0	6.7
INAA Ce	<3.0	22.0	20.0	17.0	3.0	12.7
INAA Nd	<10	10	10	10	<10	8.0
INAA Sm	<0.5	1.9	2.0	1.5	<0.5	1.2
INAA Eu	<0.2	0.3	0.6	0.4	0.2	0.32
INAA Tb	<0.5	<0.5	<0.5	<0.5	<0.5	<0.5
INAA Yb	<0.2	0.9	0.8	0.6	<0.2	0.5
INAA Lu	<0.05	0.13	0.12	0.10	<0.05	0.08
INAA Ir	<20	<20	<20	<20	<20	<20
XRF1 SiO_2	0.5 %	10.23 %	17.0 %	9.3 %	0.93 %	7.59 %
XRF1 Al_2O_3	0.16 %	1.85 %	3.49 %	1.75 %	0.46 %	1.54 %
XRF1 Fe_2O_3	0.30 %	0.86 %	1.70 %	1.42 %	0.20 %	0.90 %
XRF1 CaO	40.3 %	37.3 %	30.2 %	38.5 %	54.2 %	40.1 %
XRF1 MgO	24.1 %	18.2 %	6.73 %	18.9 %	2.54 %	14.1 %
XRF1 Na_2O	0.17 %	0.10 %	0.08 %	0.17 %	0.16 %	0.14 %
XRF1 K_2O	0.06 %	0.09 %	1.54 %	0.25 %	0.17 %	0.42 %
XRF1 TiO_2	0.02 %	0.0 %	0.12 %	0.14 %	0.04 %	0.06 %
XRF1 P_2O_5	0.04 %	0.0 %	0.09 %	0.05 %	0.04 %	0.04 %
XRF1 SO_3	0.03 %	0.07 %	0.16 %	0.02 %	0.02 %	0.06 %
XRF2 Cu	0.04 %	0.06 %	0.03 %	0.02 %	0.02 %	0.03 %
XRF2 Mo	.009 %	.005 %	.003 %	.004 %	.004 %	.005 %
XRF2 Fe_2O_3	<.01 %	2.29 %	1.57 %	<.01 %	<.01 %	0.77 %
XRF2 Zn	0.10 %	0.12 %	0.08 %	0.05 %	0.04 %	0.08 %
XRF2 Al_2O_3	.001 %	1.0 %	1.8 %	1.1 %	0.1 %	0.80 %
XRF2 SiO_2	3.3 %	13.8 %	19.7 %	13.1 %	4.2 %	10.8 %
XRF2 CaO	41.1 %	36.9 %	27.8 %	36.8 %	54.0 %	39.3 %
XRF2 SO_3	<.01 %	<.01 %	<0.1 %	<.01 %	<.01 %	<.01 %

ESCABROSA LIMESTONE

The Mississippian Escabrosa limestone was named by Ransome (1904) for Mississippian strata in the Mule Mountains in southeast Arizona. Armstrong (1962) raised the Escabrosa to group status and divided it into a lower Keating formation and an upper Hachita formation. At its type section in the Mule Mountains, the Escabrosa is mainly a light-gray thick-bedded crinoidal limestone. In the Chiricahua Mountains, the lower two-thirds of the Escabrosa, the Keating formation of Armstrong (1962), is a dark-gray mudstone with a basal crinoidal grainstone. It is massive in the lower part and thin-bedded and cherty in the upper part (Norby, 1971). The upper one-third of the Escabrosa, the Hachita formation of Armstrong (1962), consists of a light-gray, thick-bedded to massive crinoidal grainstone.

The Escabrosa lies disconformably above Late Devonian strata and is overlain unconformably by Pennsylvanian strata except in extreme southeast Arizona where it is conformably overlain by the Paradise formation.

Sampling and Analysis

The Escabrosa Limestone samples collected for analysis are from the western slope of Mineral Hill, where approximately 60 meters of thick bedded light to medium grey marbleized limestone outcrop. Whether this outcropping represents the Keating or Hachita Formations of Armstrong (1962) is

undetermined due to disconformable upper and lower contacts. Sampling was done downwards through the section perpendicular to bedding at 10 to 15 meter intervals. Table 3 shows the analyses of the five Escabrosa samples.

TABLE 3
WHOLE-ROCK GEOCHEMICAL ANALYSES - ESCABROSA LIMESTONE

ANALYSIS	SMPL. 1	SMPL.2	SMPL.3	SMPL.4	SMPL.5	AVERAGE
ICP Ag	<0.1	<0.1	<0.1	0.2	<0.1	0.08
ICP Al_2O_3	0.08 %	0.08 %	0.08 %	0.38 %	0.08 %	0.14 %
ICP As	<3.0	<3.0	<3.0	<3.0	<3.0	<3.0
ICP Ba	5.0	5.0	4.0	6.0	4.0	4.8
ICP Be	<0.5	<0.5	<0.5	<0.5	<0.5	<0.5
ICP Bi	<3.0	<3.0	<3.0	<3.0	<3.0	<3.0
ICP Cd	<1.0	<1.0	<1.0	<1.0	<1.0	<1.0
ICP Co	<1.0	<1.0	<1.0	<1.0	<1.0	<1.0
ICP Cr	6.0	4.0	4.0	5.0	6.0	5.0
ICP Cu	4.8	4.9	5.7	16.2	8.5	8.0
ICP Fe_2O_3	0.04 %	0.11 %	0.17 %	0.11 %	0.07 %	0.10 %
ICP K_2O	0.02 %	0.02 %	0.02 %	0.05 %	0.04 %	0.03 %
ICP Li	4.0	5.0	5.0	5.0	3.0	4.4
ICP MgO	0.15 %	3.0 %	3.98 %	0.6 %	0.3 %	1.61 %
ICP MnO	0.013 %	.026 %	.026 %	0.01 %	.013 %	.018 %
ICP Mo	2.0	1.0	1.0	<1.0	<1.0	1.0
ICP Na_2O	.014 %	.014 %	.014 %	.014 %	.014 %	.014 %
ICP Ni	<1.0	6.0	2.0	1.0	1.0	2.1
ICP P_2O_5	<0.02 %	.023 %	.023 %	<.02	<.02	0.01 %
ICP Pb	5.0	3.0	<2.0	3.0	4.0	3.2
ICP Sb	<5.0	<5.0	<5.0	<5.0	<5.0	<5.0
ICP Sc	<0.5	<0.5	<0.5	<0.5	<0.5	<0.5
ICP Sn	<10.0	<10.0	<10.0	<10.0	<10.0	<10.0
ICP Sr	134.0	130.0	145.0	216.0	226.0	170.2
ICP TiO_2	<0.02 %	<.02 %	<.02 %	<.02 %	<.02 %	<.02 %
ICP V	3.0	3.0	4.0	4.0	<2.0	3.0
ICP W	<10.0	<10.0	<10.0	<10.0	<10.0	<10.0

TABLE 3 (CONT.)
WHOLE-ROCK GEOCHEMICAL ANALYSES - ESCABROSA LIMESTONE

ANALYSIS	SAMPLE 1	SAMPLE 2	SAMPLE 3	SAMPLE 4	SAMPLE 5	AVERAGE
ICP Y	8.5	9.6	9.2	1.9	2.0	6.24
ICP Zn	8.9	16.0	11.0	39.0	7.8	16.54
ICP Zr	0.9	1.0	1.0	1.9	2.0	1.36
INAA Ag	<5.0	<5.0	<5.0	<5.0	<5.0	<5.0
INAA As	<2.0	<2.0	<2.0	2.0	<2.0	1.2
INAA Au	<5.0	<5.0	<5.0	<5.0	<5.0	<5.0
INAA Ba	<100	<100	<100	<100	<100	<100
INAA Br	<1.0	<1.0	<1.0	<1.0	<1.0	<1.0
INAA CaO	53.2 %	50.4 %	48.5 %	51.8 %	54.6 %	51.7 %
INAA Co	<5.0	<5.0	<5.0	<5.0	<5.0	<5.0
INAA Cr	<10.0	10.0	<10.0	10.0	<10.0	7.0
INAA Cs	<3.0	<3.0	<3.0	<3.0	<3.0	<3.0
INAA Fe_2O_3	0.07 %	0.14 %	0.29 %	0.14 %	0.14 %	0.16 %
INAA Hf	<1.0	<1.0	<1.0	<1.0	<1.0	<1.0
INAA Mo	<5.0	<5.0	<5.0	<5.0	<5.0	<5.0
INAA Na_2O	<675	<675	<675	<675	<675	<675
INAA Ni	<100	<100	<100	<100	<100	<100
INAA Rb	<30	<30	<30	<30	<30	<30
INAA Sb	<0.2	<0.2	0.2	0.4	<0.2	0.18
INAA Sc	0.2	0.2	0.2	0.4	0.1	0.22
INAA Se	<5.0	<5.0	<5.0	<5.0	<5.0	<5.0
INAA Sr	<500	<500	<500	<500	500	300
INAA Ta	<1.0	<1.0	<1.0	<1.0	<1.0	<1.0
INAA Th	<0.5	<0.5	<0.5	<0.5	<0.5	<0.5
INAA U	0.5	0.6	<0.5	0.6	<0.5	0.44
INAA W	<4.0	<4.0	<4.0	<4.0	<4.0	<4.0
INAA Zn	<50	<50	<50	50	<50	30

TABLE 3 (CONT.)
WHOLE-ROCK GEOCHEMICAL ANALYSES - ESCABROSA LIMESTONE

ANALYSIS	SMPL.1	SMPL.2	SMPL.3	SMPL. 4	SMPL.5	AVERAGE
INAA La	2.0	3.0	3.0	2.0	1.0	2.2
INAA Ce	<3.0	<3.0	<3.0	3.0	<3.0	1.8
INAA Nd	<10	<10	<10	<10	<10	<10
INAA Sm	<0.5	<0.5	<0.5	<0.5	<0.5	<0.5
INAA Eu	0.2	0.2	0.2	<0.2	0.2	0.18
INAA Tb	<0.5	<0.5	<0.5	<0.5	<0.5	<0.5
INAA Yb	0.3	0.4	0.3	0.2	<0.2	0.26
INAA Lu	<0.05	0.05	<0.05	<0.05	<0.05	0.03
INAA Ir	<20	<20	<20	<20	<20	<20
XRF1 SiO_2	0.92 %	0.99 %	1.38 %	2.14 %	0.77 %	1.24 %
XRF1 Al_2O_3	0.17 %	0.17 %	0.17 %	0.33 %	0.17 %	0.20 %
XRF1 Fe_2O_3	0.03 %	0.11 %	0.17 %	0.11 %	0.07 %	0.10 %
XRF1 CaO	56.1 %	53.1 %	52.0 %	54.5 %	55.8 %	54.3 %
XRF1 MgO	0.0 %	3.8 %	5.1 %	0.6 %	0.2 %	1.9 %
XRF1 Na_2O	0.16 %	0.16 %	0.16 %	0.16 %	0.15 %	0.16 %
XRF1 K_2O	0.07 %	0.07 %	0.06 %	0.09 %	0.08 %	.074 %
XRF1 TiO_2	0.02 %	0.02 %	0.02 %	0.03 %	0.02 %	0.02 %
XRF1 P_2O_5	0.05 %	0.06 %	0.05 %	0.04 %	0.03 %	.046 %
XRF1 SO_3	0.02 %	0.02 %	0.02 %	0.02 %	0.02 %	0.02 %
XRF2 Cu	0.04 %	0.02 %	0.02 %	0.04 %	0.02 %	0.03 %
XRF2 Mo	.004 %	.004 %	.004 %	.003 %	.004 %	.004 %
XRF2 Fe_2O_3	<.01 %	<.01 %	<.01 %	<.01 %	<.01 %	<.01 %
XRF2 Zn	0.06 %	0.05 %	0.05 %	0.06 %	0.05 %	.054 %
XRF2 Al_2O_3	.001 %	.001 %	.001 %	.001 %	.001 %	.001 %
XRF2 SiO_2	4.0 %	4.3 %	4.5 %	5.1 %	3.9 %	4.4 %
XRF2 CaO	55.9 %	52.9 %	52.1 %	54.1 %	55.5 %	54.1 %
XRF2 SO_3	<.01 %	<.01 %	<.01 %	<.01 %	<.01 %	<.01 %

BLACK PRINCE LIMESTONE/PARADISE FORMATION

The Black Prince outcrops only as a thin "marker bed" in the Mission area, and the Paradise formation is not known in the Mission area, so they were not sampled and will not be described here.

HORQUILLA FORMATION

The Pennsylvanian Horquilla formation is the basal member of the Naco group of Gilluly et al. (1954). It was named for a dominantly carbonate sequence exposed near Horquilla Peak in the Tombstone Hills. At the type section the Horquilla is about 330 meters (1000 feet) thick. The Horquilla consists of cyclically interbedded dark gray cherty and fossiliferous limestone with minor mudstone and siltstone. The Horquilla contains more interbeds of red and green mudstone than the underlying Escabrosa (Bryant, 1968). One of the characteristics that distinguishes the Horquilla from the Escabrosa is the presence of medium to large fusulinids that are completely absent from the Escabrosa. The Horquilla is also much more fossiliferous than the Escabrosa with a much greater variety. The tiny-tubed colonial coral Chaetetes occurs only in the Horquilla and Black Prince. The frequency and thickness of clastic beds increase up-section as the Horquilla grades into the overlying Earp formation. The Horquilla rests disconformably upon the Black Prince or Escabrosa limestones in southern Arizona, except in extreme

southeastern Arizona where it rests disconformably on the Paradise Formation.

Sampling and Analysis

The Horquilla Formation samples collected for analysis are from the eastern slope, crest, and upper western slope of Mineral Hill where approximately 100 meters of the Horquilla Formation outcrops. Sampling was done at approximately 20 meter intervals downwards through the section perpendicular to bedding. All samples were collected in the carbonate rather than the clastic beds for the purposes of this study. Table 4 shows the results of the four analyses run on the five Horquilla samples.

EARP FORMATION

The Earp Formation is not known in the Mission area, so it was not sampled and will not be described here.

TABLE 4
WHOLE-ROCK GEOCHEMICAL ANALYSES - HORQUILLA FORMATION

ANALYSIS	SMPL.1	SMPL.2	SMPL.3	SMPL.4	SMPL.5	AVERAGE
ICP Ag	<0.1	0.2	<0.1	<0.1	<0.1	0.08
ICP Al_2O_3	1.55 %	0.72 %	0.74 %	0.09 %	0.34 %	0.69 %
ICP As	5.0	<3.0	<3.0	<3.0	<3.0	2.2
ICP Ba	30.0	38.0	41.0	7.0	8.0	24.8
ICP Be	<0.5	<0.5	<0.5	<0.5	<0.5	<0.5
ICP Bi	<3.0	3.0	6.0	<3.0	<3.0	2.7
ICP Cd	<1.0	<1.0	<1.0	1.0	<1.0	0.6
ICP Co	<1.0	<1.0	<1.0	<1.0	<1.0	<1.0
ICP Cr	29.0	15.0	21.0	8.0	6.0	15.8
ICP Cu	73.9	97.5	24.5	14.4	20.7	46.0
ICP Fe_2O_3	0.59 %	0.4 %	0.33 %	0.19 %	0.17 %	0.34 %
ICP K_2O	0.16 %	0.11 %	0.05 %	0.05 %	0.05 %	0.08 %
ICP Li	4.0	4.0	4.0	1.0	3.0	3.2
ICP MgO	1.83 %	1.66 %	1.35 %	0.38 %	0.70 %	1.18 %
ICP MnO	0.05 %	0.05 %	0.04 %	0.03 %	0.01 %	0.04 %
ICP Mo	4.0	<1.0	<1.0	<1.0	<1.0	1.2
ICP Na_2O	0.14 %	0.18 %	0.03 %	0.04 %	0.18 %	0.11 %
ICP Ni	10.0	4.0	6.0	4.0	5.0	5.8
ICP P_2O_5	0.05 %	<.02 %	0.02 %	<.02 %	0.07 %	0.03 %
ICP Pb	7.0	10.0	21.0	3.0	<2.0	8.4
ICP Sb	<5.0	<5.0	<5.0	<5.0	<5.0	<5.0
ICP Sc	1.5	0.9	0.9	<0.5	<0.5	0.76
ICP Sn	<10.0	<10.0	<10.0	<10.0	<10.0	<10.0
ICP Sr	669.0	722.0	908.0	363.0	327.0	597.8
ICP TiO_2	0.10 %	0.05 %	0.05 %	<.02 %	0.02 %	0.05 %
ICP V	23.0	13.0	16.0	11.0	16.0	15.8
ICP W	<10.0	<10.0	<10.0	<10.0	<10.0	<10.0

TABLE 4 (CONT.)
WHOLE-ROCK GEOCHEMICAL ANALYSES - HORQUILLA FORMATION

ANALYSIS	SAMPLE 1	SAMPLE 2	SAMPLE 3	SAMPLE 4	SAMPLE 5	AVERAGE
ICP Y	7.3	5.8	4.8	3.3	4.3	5.1
ICP Zn	84.0	66.0	44.0	53.0	13.0	52.0
ICP Zr	11.0	5.3	5.9	1.3	1.7	5.0
INAA Ag	<5.0	<5.0	<5.0	<5.0	<5.0	<5.0
INAA As	5.0	3.0	2.0	<2.0	<2.0	2.4
INAA Au	<5.0	<5.0	<5.0	<5.0	<5.0	<5.0
INAA Ba	<100	<100	<100	<100	<100	<100
INAA Br	<1.0	<1.0	1.0	<1.0	<1.0	0.6
INAA CaO	49.0 %	49.0 %	53.2 %	56.0 %	49.0 %	51.2 %
INAA Co	<5.0	<5.0	<5.0	<5.0	<5.0	<5.0
INAA Cr	30.0	20.0	30.0	10.0	<10.0	19.0
INAA Cs	<3.0	3.0	<3.0	<3.0	<3.0	1.8
INAA Fe_2O_3	0.72 %	0.43 %	0.43 %	0.29 %	0.29 %	0.43 %
INAA Hf	3.0	<1.0	<1.0	<1.0	<1.0	1.0
INAA Mo	<5.0	<5.0	<5.0	<5.0	<5.0	<5.0
INAA Na_2O	1485	1755	<675	<675	1755	1134
INAA Ni	<100	<100	<100	<100	<100	<100
INAA Rb	<30	<30	<30	<30	<30	<30
INAA Sb	0.3	0.3	0.4	0.2	<0.2	0.3
INAA Sc	1.6	0.9	1.0	0.1	0.4	0.8
INAA Se	<5.0	<5.0	<5.0	<5.0	<5.0	<5.0
INAA Sr	700	700	1100	<500	<500	600
INAA Ta	<1.0	<1.0	<1.0	<1.0	<1.0	<1.0
INAA Th	2.2	1.0	0.9	<0.5	<0.5	0.9
INAA U	2.3	0.7	<0.5	6.4	5.0	2.9
INAA W	<4.0	<4.0	<4.0	<4.0	<4.0	<4.0
INAA Zn	90.0	60.0	60.0	60.0	<50.0	59.0

TABLE 4 (CONT.)
WHOLE-ROCK GEOCHEMICAL ANALYSES - HORQUILLA FORMATION

ANALYSIS	SMPL.1	SMPL.2	SMPL.3	SMPL.4	SMPL.5	AVERAGE
INAA La	9.0	6.0	5.0	2.0	4.0	5.2
INAA Ce	14.0	10.0	9.0	<3.0	3.0	7.5
INAA Nd	10.0	<10.0	<10.0	<10.0	<10.0	6.0
INAA Sm	1.3	0.9	0.7	<0.5	<0.5	0.68
INAA Eu	0.4	0.3	0.2	<0.2	0.4	0.3
INAA Tb	<0.5	<0.5	<0.5	<0.5	<0.5	<0.5
INAA Yb	0.6	0.4	0.3	<0.2	0.2	0.3
INAA Lu	0.10	0.06	0.05	<0.05	<0.05	0.05
INAA Ir	<20.0	<20.0	<20.0	<20.0	<20.0	<20.0
XRF1 SiO_2	11.6 %	7.6 %	4.6 %	2.9 %	4.5 %	6.24 %
XRF1 Al_2O_3	1.5 %	0.8 %	0.7 %	0.2 %	0.2 %	0.70 %
XRF1 Fe_2O_3	0.75 %	0.44 %	0.38 %	0.18 %	0.15 %	0.38 %
XRF1 CaO	47.2 %	49.9 %	51.9 %	54.3 %	53.0 %	51.3 %
XRF1 MgO	1.76 %	1.58 %	1.03 %	0.14 %	0.35 %	0.97 %
XRF1 Na_2O	0.14 %	0.14 %	0.14 %	0.14 %	0.13 %	0.14 %
XRF1 K_2O	0.17 %	0.13 %	0.07 %	0.07 %	0.08 %	0.10 %
XRF1 TiO_2	0.15 %	0.07 %	0.06 %	0.02 %	0.03 %	0.07 %
XRF1 P_2O_5	0.08 %	0.04 %	0.05 %	0.05 %	0.08 %	0.06 %
XRF1 SO_3	0.02 %	0.02 %	0.02 %	0.02 %	0.02 %	0.02 %
XRF2 Cu	0.07 %	0.04 %	0.03 %	0.02 %	0.04 %	0.04 %
XRF2 Mo	.003 %	.003 %	.003 %	.003 %	.003 %	.003 %
XRF2 Fe_2O_3	0.14 %	.001 %	.001 %	.001 %	.001 %	0.03 %
XRF2 Zn	0.09 %	0.05 %	0.05 %	0.05 %	0.08 %	0.06 %
XRF2 Al_2O_3	1.0 %	0.5 %	0.4 %	.001 %	0.1 %	0.4 %
XRF2 SiO_2	13.5 %	10.0 %	7.6 %	6.1 %	7.6 %	8.96 %
XRF2 CaO	47.2 %	49.8 %	51.7 %	53.9 %	52.5 %	51.0 %
XRF2 SO_3	<.01 %	<.01 %	<.01 %	<.01 %	<.01 %	<.01 %

COLINA FORMATION

The Lower Permian Colina limestone, whose type section is at Colina Ridge in the Tombstone Hills a few kilometers SW of Tombstone, Arizona, was named by Gilluly et al. (1954). The thickness of the Colina Formation varies from 200 meters at the type section to 61 meters in other mountain ranges in southeastern Arizona due to the nature of its contact with the overlying Epitaph Formation. The contact between the Colina and the Epitaph formation is of a chemical rather than a sedimentological nature, consisting of an irregular dolomitization boundary not confined to a given stratigraphic horizon. In many places limestones of the Colina Formation grade laterally into dolomites of the Epitaph, making the choice of boundary and thickness largely dependent on the extent of dolomitization (Bryant, 1968).

The Colina lacks a well-developed cyclicity, being composed of a uniform sequence of thick-bedded to massive dark-gray to black limestone (Bryant, 1968). One of the most diagnostic features of the Colina is the very dark gray to black color on a fresh surface and the tendency to be much lighter on a weathered surface (Bryant, 1968).

Sampling and Analysis

The Colina Formation samples collected for analysis are from the eastern slope of Cienega Ridge in the Empire mountains in Section 8, T18S, R17E, approximately two

kilometers to the west of Total Wreck Ridge. At this location the Colina formation is approximately 120 meters thick. Sampling was done at approximately 20 meter intervals upwards through the section perpendicular to bedding. Table 5 shows the analyses of the five Colina samples.

TABLE 5
WHOLE-ROCK GEOCHEMICAL ANALYSES - COLINA FORMATION

ANALYSIS	SMPL.1	SMPL.2	SMPL.3	SMPL.4	SMPL.5	AVERAGE
ICP Ag	<0.1	0.2	<0.1	<0.1	<0.1	0.08
ICP Al_2O_3	0.32 %	1.12 %	0.55 %	0.62 %	2.04 %	0.93 %
ICP As	<3.0	3.0	<3.0	<3.0	<3.0	1.8
ICP Ba	29.0	36.0	18.0	16.0	40.0	27.8
ICP Be	<0.5	<0.5	<0.5	<0.5	<0.5	<0.5
ICP Bi	<3.0	<3.0	<3.0	<3.0	<3.0	<3.0
ICP Cd	<1.0	<1.0	<1.0	<1.0	<1.0	<1.0
ICP Co	<1.0	<1.0	<1.0	<1.0	<1.0	<1.0
ICP Cr	7.0	18.0	9.0	11.0	19.0	12.8
ICP Cu	5.9	8.3	5.1	9.6	10.9	8.0
ICP Fe_2O_3	0.4 %	0.5 %	0.26 %	0.33 %	0.53 %	0.40 %
ICP K_2O	0.14 %	0.43 %	0.19 %	0.25 %	0.29 %	0.26 %
ICP Li	3.0	13.0	6.0	7.0	7.0	7.2
ICP MgO	12.8 %	9.8 %	4.7 %	18.3 %	16.6 %	12.4 %
ICP MnO	0.04 %	0.01 %	0.01 %	0.01 %	0.01 %	0.02 %
ICP Mo	1.0	3.0	1.0	2.0	1.0	1.6
ICP Na_2O	0.01 %	0.03 %	0.03 %	0.03 %	0.02 %	0.02 %
ICP Ni	4.0	6.0	3.0	3.0	6.0	4.4
ICP P_2O_5	<.02 %	0.07 %	<.02 %	<.02 %	0.05 %	0.03 %
ICP Pb	<2.0	5.0	<2.0	3.0	19.0	5.8
ICP Sb	<5.0	<5.0	<5.0	<5.0	<5.0	<5.0
ICP Sc	<0.5	1.0	0.6	0.9	1.7	0.89
ICP Sn	<10.0	<10.0	<10.0	<10.0	<10.0	<10.0
ICP Sr	186.0	168.0	237.0	135.0	122.0	169.6
ICP TiO_2	0.02 %	0.10 %	0.03 %	0.05 %	0.12 %	0.06 %
ICP V	9.0	19.0	6.0	11.0	15.0	12.0
ICP W	<10.0	<10.0	<10.0	<10.0	<10.0	<10.0

TABLE 5 (CONT.)
WHOLE-ROCK GEOCHEMICAL ANALYSES - COLINA FORMATION

ANALYSIS	SAMPLE 1	SAMPLE 2	SAMPLE 3	SAMPLE 4	SAMPLE 5	AVERAGE
ICP Y	1.7	4.5	2.7	5.2	6.5	4.1
ICP Zn	15.0	3.4	4.7	4.1	25.0	10.4
ICP Zr	6.2	8.5	3.3	11.0	41.0	14.0
INAA Ag	<5.0	<5.0	<5.0	<5.0	<5.0	<5.0
INAA As	<2.0	<2.0	2.0	<2.0	5.0	2.0
INAA Au	<5.0	<5.0	<5.0	<5.0	<5.0	<5.0
INAA Ba	<100	<100	<100	<100	<100	<100
INAA Br	<1.0	<1.0	1.0	<1.0	1.0	0.7
INAA CaO	35.0 %	37.8 %	46.2 %	29.4 %	28.0 %	35.3 %
INAA Co	<5.0	<5.0	<5.0	<5.0	<5.0	<5.0
INAA Cr	10.0	20.0	10.0	10.0	20.0	14.0
INAA Cs	<3.0	<3.0	<3.0	<3.0	3.0	1.8
INAA Fe_2O_3	0.43 %	0.57 %	0.29 %	0.43 %	0.72 %	0.49 %
INAA Hf	<1.0	2.0	1.0	2.0	2.0	1.5
INAA Mo	<5.0	<5.0	<5.0	<5.0	<5.0	<5.0
INAA Na_2O	<675	675	<675	<675	<675	405
INAA Ni	<100	<100	<100	<100	<100	<100
INAA Rb	<30.0	<30.0	<30.0	<30.0	<30.0	<30.0
INAA Sb	0.2	0.2	0.2	0.3	1.3	0.4
INAA Sc	0.4	1.1	0.6	1.0	2.1	1.04
INAA Se	<5.0	<5.0	<5.0	<5.0	<5.0	<5.0
INAA Sr	<500	<500	<500	<500	<500	<500
INAA Ta	<1.0	<1.0	<1.0	<1.0	<1.0	<1.0
INAA Th	<0.5	1.3	0.8	1.3	1.6	1.05
INAA U	1.4	3.9	1.2	2.9	1.9	2.3
INAA W	<4.0	<4.0	<4.0	<4.0	<4.0	<4.0
INAA Zn	<50.0	<50.0	<50.0	<50.0	<50.0	<50.0

TABLE 5 (CONT.)
WHOLE-ROCK GEOCHEMICAL ANALYSES - COLINA FORMATION

ANALYSIS	SMPL.1	SMPL.2	SMPL.3	SMPL.4	SMPL.5	AVERAGE
INAA La	2.0	5.0	3.0	6.0	8.0	4.8
INAA Ce	5.0	11.0	7.0	12.0	16.0	10.2
INAA Nd	<10.0	<10.0	<10.0	<10.0	<10.0	<10.0
INAA Sm	<0.5	0.9	0.6	1.2	1.3	0.85
INAA Eu	0.2	0.3	0.5	0.3	0.5	0.36
INAA Tb	<0.5	<0.5	<0.5	<0.5	<0.5	<0.5
INAA Yb	<0.2	0.5	0.3	0.6	0.6	0.42
INAA Lu	<0.05	0.08	<0.05	0.09	0.09	0.06
INAA Ir	<20	<20	<20	<20	<20	<20
XRF1 SiO_2	4.19 %	16.8 %	4.30 %	7.84 %	15.4 %	9.70 %
XRF1 Al_2O_3	0.41 %	1.16 %	0.67 %	0.89 %	1.89 %	1.0 %
XRF1 Fe_2O_3	0.51 %	0.64 %	0.24 %	0.64 %	0.72 %	0.55 %
XRF1 CaO	41.7 %	38.7 %	49.4 %	35.5 %	32.7 %	39.6 %
XRF1 MgO	18.8 %	13.2 %	6.1 %	26.8 %	27.0 %	18.4 %
XRF1 Na_2O	0.16 %	0.12 %	0.13 %	0.14 %	0.14 %	0.14 %
XRF1 K_2O	0.16 %	0.38 %	0.23 %	0.26 %	0.26 %	0.26 %
XRF1 TiO_2	0.05 %	0.14 %	0.06 %	0.16 %	0.25 %	0.13 %
XRF1 P_2O_5	0.04 %	0.07 %	0.04 %	0.04 %	0.06 %	0.05 %
XRF1 SO_3	0.02 %	0.0 %	0.02 %	0.01 %	0.02 %	0.01 %
XRF2 Cu	0.01 %	0.04 %	0.07 %	0.05 %	0.01 %	0.04 %
XRF2 Mo	.005 %	.002 %	.003 %	.007 %	.004 %	.004 %
XRF2 Fe_2O_3	<.01 %	<.01 %	<.01 %	<.01 %	0.43 %	0.09 %
XRF2 Zn	0.05 %	0.09 %	0.11 %	0.12 %	0.05 %	0.08 %
XRF2 Al_2O_3	0.1 %	0.6 %	0.3 %	0.5 %	1.1 %	0.5 %
XRF2 SiO_2	7.7 %	18.3 %	7.5 %	10.0 %	17.2 %	12.1 %
XRF2 CaO	42.3 %	38.3 %	49.5 %	35.9 %	31.2 %	39.4 %
XRF2 SO_3	<.01 %	<.01 %	<.01 %	<.01 %	<.01 %	<.01 %

EPITAPH FORMATION

The Lower Permian Epitaph formation consists of interbedded dolomite, fine clastics, limestone, and evaporites, and ranges in thickness from 305 to 457 meters. In the type section near Tombstone, Arizona, the lower 80 meters is dolomite and the upper 160 meters is alternating limestone, mudstone, and dolomite. In other parts of Arizona, the Epitaph is more variable, containing gypsum in the Twin Buttes area and in the Whetstone and Empire Mountains. One of the most distinctive features of the Epitaph dolomites is the abundance of knots, blebs, and geodes of quartz and calcite, ranging from a few millimeters to a few centimeters in diameter. No other formation in the Paleozoic is southeastern Arizona has these blebs and geodes in quantity except the Rainvalley Formation, which is much higher in the section (Bryant, 1968).

The Epitaph formation has been mapped only at scattered localities in Cochise, Pima, and Santa Cruz Counties. Its absence at other locations in the area poses what is probably the major enigma of southeast Arizona Paleozoic stratigraphy (Blakey, 1989), as locations where the Epitaph is absent do not show thickening of the conformably underlying and overlying strata.

Sampling and Analysis

The Epitaph Formation samples collected for analysis are from the lower eastern slope of Total Wreck Ridge in the

Empire Mountains in Sections 8 and 17, T18S, R17E. The section of Epitaph Formation at this location is approximately 450 meters thick. Sampling was done upwards through the section perpendicular to bedding at approximately 80 meter intervals, depending on availability of carbonate beds to sample. All samples were collected in the carbonate beds rather than in the clastics or evaporites for purposes of this study, as previously explained. Table 6 shows the analyses of the five Epitaph samples.

TABLE 6
WHOLE-ROCK GEOCHEMICAL ANALYSES - EPITAPH FORMATION

ANALYSIS	SMPL.1	SMPL.2	SMPL.3	SMPL.4	SMPL.5	AVERAGE
ICP Ag	<0.1	<0.1	<0.1	<0.1	<0.1	<0.1
ICP Al_2O_3	1.66 %	0.36 %	0.08 %	0.70 %	2.40 %	1.04 %
ICP As	9.0	3.0	6.0	<3.0	<3.0	4.2
ICP Ba	39.0	8.0	14.0	92.0	140.0	58.6
ICP Be	<0.5	<0.5	<0.5	<0.5	0.6	0.32
ICP Bi	<3.0	<3.0	<3.0	<3.0	<3.0	<3.0
ICP Cd	<1.0	<1.0	<1.0	<1.0	<1.0	<1.0
ICP Co	<1.0	<1.0	<1.0	<1.0	<1.0	<1.0
ICP Cr	25.0	15.0	8.0	9.0	24.0	16.2
ICP Cu	23.0	8.4	6.4	7.4	21.2	13.3
ICP Fe_2O_3	0.93 %	0.16 %	0.29 %	0.50 %	0.68 %	0.51 %
ICP K_2O	0.46 %	0.07 %	0.01 %	0.08 %	1.02 %	0.33 %
ICP Li	16.0	6.0	4.0	10.0	21.0	11.4
ICP MgO	13.5 %	1.99 %	18.3 %	10.5 %	12.6 %	11.4 %
ICP MnO	0.03 %	0.01 %	0.05 %	0.05 %	0.03 %	0.03 %
ICP Mo	3.0	3.0	<1.0	2.0	2.0	2.1
ICP Na_2O	0.03 %	0.01 %	0.01 %	0.03 %	0.08 %	0.03 %
ICP Ni	7.0	5.0	<1.0	4.0	5.0	4.3
ICP P_2O_5	0.05 %	0.02 %	<.02 %	<.02 %	0.05 %	0.03 %
ICP Pb	29.0	4.0	35.0	3.0	2.0	14.6
ICP Sb	<5.0	<5.0	<5.0	<5.0	<5.0	<5.0
ICP Sc	0.9	<0.5	<0.5	<0.5	1.7	0.67
ICP Sn	<10.0	<10.0	<10.0	<10.0	<10.0	<10.0
ICP Sr	212.0	278.0	94.7	240.0	514.0	267.7
ICP TiO_2	0.07 %	<.02 %	<.02 %	0.03 %	0.23 %	0.07 %
ICP V	15.0	15.0	12.0	13.0	12.0	13.4
ICP W	<10.0	<10.0	<10.0	<10.0	<10.0	<10.0

TABLE 6 (CONT.)
WHOLE-ROCK GEOCHEMICAL ANALYSES - EPITAPH FORMATION

ANALYSIS	SMPL.1	SMPL.2	SMPL.3	SMPL.4	SMPL.5	AVERAGE
ICP Y	5.7	3.7	2.1	4.1	10.0	5.1
ICP Zn	15.0	7.8	36.0	10.0	32.0	20.2
ICP Zr	6.8	4.0	1.6	1.7	5.4	3.9
INAA Ag	<5.0	<5.0	<5.0	<5.0	<5.0	<5.0
INAA As	5.0	<2.0	2.0	2.0	3.0	2.6
INAA Au	<5.0	<5.0	<5.0	<5.0	<5.0	<5.0
INAA Ba	100	<100	100	100	200	110
INAA Br	1.0	<1.0	1.0	<1.0	<1.0	0.7
INAA CaO	21.0 %	46.2 %	29.4 %	37.8 %	21.0 %	31.1 %
INAA Co	<5.0	<5.0	<5.0	<5.0	<5.0	<5.0
INAA Cr	30.0	10.0	10.0	10.0	20.0	16.0
INAA Cs	<3.0	<3.0	<3.0	<3.0	10.0	3.2
INAA Fe_2O_3	1.0 %	0.14 %	0.29 %	0.57 %	0.71 %	0.54 %
INAA Hf	2.0	<1.0	<1.0	<1.0	4.0	1.5
INAA Mo	<5.0	<5.0	<5.0	<5.0	<5.0	<5.0
INAA Na_2O	<675	<675	<675	<675	810	432
INAA Ni	<100	<100	<100	<100	<100	<100
INAA Rb	<30.0	<30.0	<30.0	<30.0	40.0	20.0
INAA Sb	0.9	0.8	0.4	0.4	2.4	0.98
INAA Sc	1.1	0.4	0.1	0.7	1.9	0.84
INAA Se	<5.0	<5.0	<5.0	<5.0	<5.0	<5.0
INAA Sr	<500	<500	<500	<500	<500	<500
INAA Ta	<1.0	<1.0	<1.0	<1.0	<1.0	<1.0
INAA Th	1.5	0.5	<0.5	0.5	2.4	1.03
INAA U	1.3	2.1	<0.5	0.5	1.4	1.11
INAA W	<4.0	<4.0	<4.0	<4.0	<4.0	<4.0
INAA Zn	<50.0	<50.0	<50.0	<50.0	<50.0	<50.0

TABLE 6 (CONT.)
WHOLE-ROCK GEOCHEMICAL ANALYSES - EPITAPH FORMATION

ANALYSIS	SMPL.1	SMPL.2	SMPL.3	SMPL.4	SMPL.5	AVERAGE
INAA La	6.0	3.0	2.0	4.0	9.0	4.8
INAA Ce	9.0	5.0	4.0	7.0	16.0	8.2
INAA Nd	<10.0	<10.0	<10.0	10.0	10.0	7.0
INAA Sm	1.1	<0.5	<0.5	0.8	1.8	0.8
INAA Eu	0.5	0.2	0.2	0.3	0.4	0.32
INAA Tb	<0.5	<0.5	<0.5	<0.5	<0.5	<0.5
INAA Yb	0.6	0.2	<0.2	0.3	1.1	0.46
INAA Lu	0.08	0.05	<0.05	0.05	0.16	0.07
INAA Ir	<20.0	<20.0	<20.0	<20.0	<20.0	<20.0
XRF1 SiO_2	26.1 %	4.21 %	1.32 %	5.22 %	35.2 %	14.4 %
XRF1 Al_2O_3	1.59 %	0.52 %	0.25 %	0.76 %	2.20 %	1.06 %
XRF1 Fe_2O_3	1.42 %	0.18 %	0.46 %	0.59 %	0.96 %	0.72 %
XRF1 CaO	29.1 %	51.9 %	39.0 %	43.2 %	26.7 %	38.0 %
XRF1 MgO	18.1 %	3.79 %	24.5 %	14.8 %	19.6 %	16.2 %
XRF1 Na_2O	0.18 %	0.17 %	0.17 %	0.17 %	0.17 %	0.17 %
XRF1 K_2O	0.33 %	0.09 %	0.05 %	0.10 %	0.64 %	0.24 %
XRF1 TiO_2	0.17 %	0.05 %	0.03 %	0.07 %	0.36 %	0.14 %
XRF1 P_2O_5	0.05 %	0.06 %	0.04 %	0.04 %	0.05 %	0.05 %
XRF1 SO_3	0.02 %	0.02 %	0.02 %	0.02 %	0.03 %	0.02 %
XRF2 Cu	0.01 %	0.02 %	0.01 %	0.03 %	0.01 %	0.02 %
XRF2 Mo	.006 %	.003 %	.008 %	.004 %	.002 %	.005 %
XRF2 Fe_2O_3	0.57 %	<.01 %	<.01 %	0.29 %	0.57 %	0.29 %
XRF2 Zn	0.04 %	0.05 %	0.06 %	0.08 %	0.04 %	0.05 %
XRF2 Al_2O_3	1.1 %	0.2 %	<.01 %	0.4 %	1.2 %	0.58 %
XRF2 SiO_2	28.2 %	6.6 %	3.6 %	8.7 %	37.9 %	17.0 %
XRF2 CaO	25.2 %	52.2 %	40.0 %	42.6 %	22.0 %	36.4 %
XRF2 SO_3	<.01 %	<.01 %	<.01 %	<.01 %	<.01 %	<.01 %

SCHERRER FORMATION

The Middle Permian Scherrer formation was named by Gilluly et al. (1954) for strata exposed at Scherrer Ridge in the Gunnison Hills, near Texas Canyon in Cochise County. At the type section, the formation consists of 20 meters of basal siltstone redbeds, 100 meters of lower silty quartz sandstone, 50 meters of middle dolomitic carbonate, and 50 meters of upper quartz arenite sandstone. The sandstones are mostly fine to medium grained, well rounded and well sorted. Cross bedding is a common feature. Small brown iron oxide spots from the weathering of a preexisting iron mineral occur as pits and nodes that are characteristic and seem to be diagnostic of the Scherrer throughout its outcrop area. The formation thins to the west and southwest of the type section.

Where present, the underlying Epitaph formation grades into the basal redbeds of the Scherrer. The contact with the overlying Concha formation is sharp.

Sampling and Analysis

The Scherrer Formation samples collected for analysis are from the upper eastern slope of Total Wreck Ridge in Sections 8 and 17, T18S, R17E, in the Empire Mountains. The entire section of the Scherrer is about 200 meters thick at this location, but samples were only collected in the approximately 50 meters of carbonate in the middle of the formation.

Samples were collected about 10 to 15 meters apart, upwards through the section perpendicular to bedding. Due to the lack of good outcrop to sample, only three samples were collected from the Scherrer formation. Table 7 shows the analyses of the three Scherrer samples.

TABLE 7
WHOLE-ROCK GEOCHEMICAL ANALYSES - SCHERRER FORMATION

ANALYSIS	SAMPLE 1	SAMPLE 2	SAMPLE 3	AVERAGE
ICP Ag	0.1	<0.1	<0.1	0.07
ICP Al_2O_3	0.55 %	0.36 %	0.49 %	0.47 %
ICP As	<3.0	<3.0	4.0	2.3
ICP Ba	8.0	10.0	7.0	8.3
ICP Be	<0.5	<0.5	<0.5	<0.5
ICP Bi	<3.0	<3.0	<3.0	<3.0
ICP Cd	<1.0	<1.0	1.0	0.67
ICP Co	<1.0	<1.0	<1.0	<1.0
ICP Cr	13.0	13.0	13.0	13.0
ICP Cu	12.7	4.4	6.9	8.0
ICP Fe_2O_3	0.54 %	0.19 %	0.43 %	0.39 %
ICP K_2O	0.01 %	0.05 %	0.012 %	0.02 %
ICP Li	5.0	8.0	5.0	6.0
ICP MgO	16.6 %	3.15 %	16.6 %	5.53 %
ICP MnO	0.09 %	0.01 %	0.04 %	0.05 %
ICP Mo	2.0	2.0	1.0	1.67
ICP Na_2O	0.03 %	0.01 %	0.03 %	0.23 %
ICP Ni	2.0	3.0	5.0	3.3
ICP P_2O_5	0.05 %	<0.02 %	0.02 %	0.026 %
ICP Pb	3.0	<2.0	3.0	2.3
ICP Sb	<5.0	<5.0	<5.0	<5.0
ICP Sc	<0.5	<0.5	<0.5	<0.5
ICP Sn	<10.0	<10.0	<10.0	<10.0
ICP Sr	133.0	385.0	183.0	233.7
ICP TiO_2	<0.02 %	<0.02 %	<0.02 %	<0.02 %
ICP V	13.0	17.0	26.0	18.7
ICP W	<10.0	<10.0	<10.0	<10.0

TABLE 7 (CONT.)
WHOLE-ROCK GEOCHEMICAL ANALYSES - SCHERRER FORMATION

ANALYSIS	SAMPLE 1	SAMPLE 2	SAMPLE 3	AVERAGE
ICP Y	3.7	2.5	3.4	3.2
ICP Zn	27.0	6.0	30.0	21.0
ICP Zr	2.5	2.8	2.4	2.57
INAA Ag	<5.0	<5.0	<5.0	<5.0
INAA As	<2.0	<2.0	2.0	1.33
INAA Au	<5.0	<5.0	<5.0	<5.0
INAA Ba	<100	<100	<100	<100
INAA Br	<1.0	1.0	1.0	0.83
INAA CaO	29.4 %	49.0 %	28.0 %	35.5 %
INAA Co	<5.0	<5.0	<5.0	<5.0
INAA Cr	10.0	20.0	10.0	13.33
INAA Cs	<3.0	<3.0	<3.0	<3.0
INAA Fe_2O_3	0.72 %	0.14 %	0.57 %	0.48 %
INAA Hf	1.0	<1.0	<1.0	0.67
INAA Mo	<5.0	<5.0	<5.0	<5.0
INAA Na_2O	<675	<675	<675	<675
INAA Ni	<100	<100	<100	<100
INAA Rb	<30.0	<30.0	<30.0	<30.0
INAA Sb	1.9	0.4	0.9	1.07
INAA Sc	0.4	0.4	0.5	0.43
INAA Se	<5.0	<5.0	<5.0	<5.0
INAA Sr	<500	<500	<500	<500
INAA Ta	<1.0	<1.0	<1.0	<1.0
INAA Th	0.6	0.5	<0.5	0.45
INAA U	0.9	1.9	2.5	1.77
INAA W	<4.0	<4.0	<4.0	<4.0
INAA Zn	<50.0	<50.0	<50.0	<50.0

TABLE 7 (CONT.)
WHOLE-ROCK GEOCHEMICAL ANALYSES - SCHERRER FORMATION

ANALYSIS	SAMPLE 1	SAMPLE 2	SAMPLE 3	AVERAGE
INAA La	5.0	2.0	5.0	4.0
INAA Ce	8.0	3.0	8.0	6.3
INAA Nd	<10.0	<10.0	<10.0	<10.0
INAA Sm	0.7	<0.5	0.6	0.52
INAA Eu	0.2	0.2	0.4	0.27
INAA Tb	<0.5	<0.5	<0.5	<0.5
INAA Yb	0.3	0.2	0.2	0.23
INAA Lu	0.05	<0.05	<0.05	0.03
INAA Ir	<20.0	<20.0	<20.0	<20.0
XRF1 SiO_2	9.58 %	3.47 %	3.42 %	5.49 %
XRF1 Al_2O_3	0.59 %	0.48 %	0.55 %	0.54 %
XRF1 Fe_2O_3	0.78 %	0.19 %	0.52 %	0.50 %
XRF1 CaO	35.34 %	51.20 %	38.53 %	41.69 %
XRF1 MgO	24.98 %	5.24 %	24.02 %	18.08 %
XRF1 Na_2O	0.18 %	0.16 %	0.17 %	0.17 %
XRF1 K_2O	0.01 %	0.07 %	0.03 %	0.037 %
XRF1 TiO_2	0.08 %	0.04 %	0.06 %	0.06 %
XRF1 P_2O_5	0.07 %	0.05 %	0.05 %	0.057 %
XRF1 SO_3	0.02 %	0.02 %	0.02 %	0.02 %
XRF2 Cu	0.01 %	0.04 %	0.04 %	0.03 %
XRF2 Mo	0.008 %	0.004 %	0.008 %	0.007 %
XRF2 Fe_2O_3	0.57 %	<0.01 %	0.14 %	0.24 %
XRF2 Zn	0.05 %	0.06 %	0.09 %	0.07 %
XRF2 Al_2O_3	0.2 %	0.1 %	0.2 %	0.167 %
XRF2 SiO_2	14.0 %	6.2 %	7.2 %	9.13 %
XRF2 CaO	34.1 %	51.7 %	38.1 %	41.3 %
XRF2 SO_3	<0.01 %	<0.01 %	<0.01 %	<0.01 %

CONCHA FORMATION

The upper Middle Permian Concha limestone was named by Gilluly et al. (1954) for about 40 meters of cherty fossiliferous limestone exposed at Concha Ridge in the Gunnison Hills, near Texas Canyon in Cochise County. A reference section 174 meters thick was described by Bryant and McClymonds (1961) in the Mustang Mountains, approximately 15 kilometers NW of Sierra Vista, Arizona. The base of the Concha is sandy or silty limestone or dolomitic limestone, grading upward into thick-bedded medium to dark gray cherty limestone. The Concha Formation has fewer clastic rocks than any other Paleozoic formation in southeastern Arizona, and is probably the most cherty and fossiliferous (Bryant, 1968). Its upper contact with the Rainvalley formation is gradational.

The Concha formation outcrops throughout southeastern Arizona and southwestern New Mexico except where removed by post-Paleozoic erosion. In central and western Cochise County its thickness is a relatively constant 150 meters, thinning slightly to the west and southwest (Bryant and McClymonds, 1961).

Sampling and Analysis

Concha Formation samples one through five collected for analysis are from Helmet Peak, approximately three kilometers southwest of the Mission Complex and seven kilometers

northwest of the Twin Buttes Mine. The section at Helmet Peak is about 150 meters thick, and samples were collected 20 to 25 meters apart downwards through the section perpendicular to bedding. Sample six was collected at the base of the Concha formation section on Total Wreck Ridge a few meters above the contact with the Scherrer Formation. The sixth sample was collected to determine if there was any notable difference in the geochemistry of the Concha Formation at different locations. The geochemistry of sample six was similar to that of samples one through three collected on Helmet Peak, and it was included in the study along with the other Concha samples. Table 8 shows the analyses of the six Concha samples.

TABLE 8
WHOLE-ROCK GEOCHEMICAL ANALYSES - CONCHA FORMATION

ANALYSIS	SAMPLE 1	SAMPLE 2	SAMPLE 3
ICP Ag	<0.1	<0.1	0.2
ICP Al_2O_3	0.06 %	0.38 %	0.41 %
ICP As	5.0	5.0	11.0
ICP Ba	34.0	45.0	29.0
ICP Be	<0.5	<0.5	<0.5
ICP Bi	<3.0	3.0	<3.0
ICP Cd	<1.0	<1.0	<1.0
ICP Co	<1.0	<1.0	<1.0
ICP Cr	13.0	33.0	19.0
ICP Cu	3.8	6.1	7.8
ICP Fe_2O_3	0.07 %	0.36 %	0.35 %
ICP K_2O	0.01 %	0.11 %	0.12 %
ICP Li	1.0	2.0	2.0
ICP MgO	0.20 %	3.82 %	0.75 %
ICP MnO	0.05 %	0.10 %	0.06 %
ICP Mo	1.0	3.0	4.0
ICP Na_2O	0.014 %	0.014 %	0.014 %
ICP Ni	4.0	5.0	12.0
ICP P_2O_5	0.07 %	0.44 %	0.16 %
ICP Pb	27.0	13.0	13.0
ICP Sb	<5.0	<5.0	<5.0
ICP Sc	<0.5	<0.5	<0.5
ICP Sn	<10.0	<10.0	<10.0
ICP Sr	266.0	298.0	301.0
ICP TiO_2	<0.02 %	<0.02 %	<0.02 %
ICP V	11.0	11.0	13.0
ICP W	<10.0	<10.0	<10.0

TABLE 8 (CONT.)
WHOLE-ROCK GEOCHEMICAL ANALYSES - CONCHA FORMATION

ANALYSIS	SAMPLE 4	SAMPLE 5	SAMPLE 6	AVERAGE
ICP Ag	<0.1	0.2	<0.1	0.1
ICP Al_2O_3	0.72 %	1.30 %	0.28 %	0.53 %
ICP As	7.0	<3.0	<3.0	5.2
ICP Ba	14.0	81.0	8.0	35.2
ICP Be	<0.5	0.7	<0.5	0.33
ICP Bi	<3.0	<3.0	3.0	2.0
ICP Cd	<1.0	<1.0	<1.0	<1.0
ICP Co	<1.0	<1.0	<1.0	<1.0
ICP Cr	47.0	19.0	15.0	24.3
ICP Cu	18.4	21.2	6.0	10.6
ICP Fe_2O_3	1.20 %	1.27 %	0.16 %	0.57 %
ICP K_2O	0.22 %	0.40 %	0.05 %	0.15 %
ICP Li	3.0	4.0	3.0	2.5
ICP MgO	14.3 %	12.5 %	0.65 %	5.37 %
ICP MnO	0.06 %	0.08 %	0.013 %	0.06 %
ICP Mo	2.0	4.0	<1.0	2.4
ICP Na_2O	0.03 %	0.03 %	0.014 %	0.02 %
ICP Ni	5.0	10.0	30	11.0
ICP P_2O_5	0.53 %	0.05 %	0.25 %	0.25 %
ICP Pb	16.0	5.0	4.0	13.0
ICP Sb	<5.0	<5.0	<5.0	<5.0
ICP Sc	0.7	0.8	<0.5	0.42
ICP Sn	<10.0	<10.0	<10.0	<10.0
ICP Sr	71.3	73.6	188.0	199.7
ICP TiO_2	0.02 %	0.03 %	<0.02 %	0.015 %
ICP V	17.0	10.0	12.0	12.3
ICP W	<10.0	<10.0	<10.0	<10.0

TABLE 8 (CONT.)
WHOLE-ROCK GEOCHEMICAL ANALYSES - CONCHA FORMATION

ANALYSIS	SAMPLE 1	SAMPLE 2	SAMPLE 3
ICP Y	3.9	4.8	4.5
ICP Zn	130.0	34.0	170.0
ICP Zr	1.1	3.4	2.5
INAA Ag	<5.0	<5.0	<5.0
INAA As	3.0	7.0	11.0
INAA Au	<5.0	6.0	<5.0
INAA Ba	<100	<100	<100
INAA Br	<1.0	1.0	<1.0
INAA CaO	51.8 %	42.0 %	42.0 %
INAA Co	<5.0	<5.0	<5.0
INAA Cr	20.0	40.0	20.0
INAA Cs	<3.0	<3.0	<3.0
INAA Fe_2O_3	0.14 %	0.43 %	0.43 %
INAA Hf	<1.0	<1.0	<1.0
INAA Mo	<5.0	<5.0	<5.0
INAA Na_2O	<675	<675	<675
INAA Ni	<100	<100	<100
INAA Rb	<30.0	<30.0	<30.0
INAA Sb	0.7	1.0	5.7
INAA Sc	0.1	0.4	0.5
INAA Se	<5.0	<5.0	<5.0
INAA Sr	<500	<500	<500
INAA Ta	<1.0	<1.0	<1.0
INAA Th	<0.5	0.5	<0.5
INAA U	1.2	1.5	1.6
INAA W	<4.0	<4.0	<4.0
INAA Zn	130	<50	160

TABLE 8 (CONT.)
WHOLE-ROCK GEOCHEMICAL ANALYSES - CONCHA FORMATION

ANALYSIS	SAMPLE 4	SAMPLE 5	SAMPLE 6	AVERAGE
ICP Y	6.9	3.1	6.5	4.95
ICP Zn	57.0	61.0	17.0	78.2
ICP Zr	6.6	6.9	1.8	3.72
INAA Ag	<5.0	<5.0	<5.0	<5.0
INAA As	6.0	3.0	<2.0	5.2
INAA Au	<5.0	<5.0	<5.0	3.1
INAA Ba	<100	<100	<100	<100
INAA Br	1.0	1.0	<1.0	0.75
INAA CaO	26.6 %	21.0 %	44.8 %	38.0 %
INAA Co	<5.0	<5.0	<5.0	<5.0
INAA Cr	60.0	20.0	10.0	28.3
INAA Cs	<3.0	<3.0	<3.0	<3.0
INAA Fe_2O_3	1.43 %	1.43 %	0.14 %	0.64 %
INAA Hf	1.0	1.0	<1.0	0.67
INAA Mo	<5.0	5.0	<5.0	2.9
INAA Na_2O	<675	<675	<675	<675
INAA Ni	<100	<100	<100	<100
INAA Rb	<30.0	<30.0	<30.0	<30.0
INAA Sb	1.0	1.0	0.2	1.6
INAA Sc	0.9	0.9	0.3	0.52
INAA Se	<5.0	<5.0	<5.0	<5.0
INAA Sr	<500	<500	<500	<500
INAA Ta	<1.0	<1.0	<1.0	<1.0
INAA Th	0.8	0.7	<0.5	0.46
INAA U	2.3	1.5	1.1	1.5
INAA W	<4.0	<4.0	<4.0	<4.0
INAA Zn	80.0	70.0	<50.0	81.7

TABLE 8 (CONT.)
WHOLE-ROCK GEOCHEMICAL ANALYSES - CONCHA FORMATION

ANALYSIS	SAMPLE 1	SAMPLE 2	SAMPLE 3
INAA La	2.0	4.0	3.0
INAA Ce	<3.0	<3.0	<3.0
INAA Nd	<10.0	<10.0	<10.0
INAA Sm	<0.5	<0.5	<0.5
INAA Eu	0.2	<0.2	0.3
INAA Tb	<0.5	<0.5	<0.5
INAA Yb	<0.2	0.2	0.2
INAA Lu	<0.05	<0.05	<0.05
INAA Ir	<20.0	<20.0	<20.0
XRF1 SiO_2	2.58 %	8.85 %	13.2 %
XRF1 Al_2O_3	0.15 %	0.50 %	0.54 %
XRF1 Fe_2O_3	0.12 %	0.48 %	0.58 %
XRF1 CaO	54.4 %	46.8 %	47.1 %
XRF1 MgO	0.22 %	4.96 %	0.87 %
XRF1 Na_2O	0.14 %	0.16 %	0.16 %
XRF1 K_2O	0.07 %	0.13 %	0.14 %
XRF1 TiO_2	0.02 %	0.04 %	0.04 %
XRF1 P_2O_5	0.10 %	0.42 %	0.17 %
XRF1 SO_3	0.02 %	0.02 %	0.02 %
XRF2 Cu	0.02 %	0.02 %	0.05 %
XRF2 Mo	0.004 %	0.004 %	0.003 %
XRF2 Fe_2O_3	<.01 %	<.01 %	<.01 %
XRF2 Zn	0.07 %	0.05 %	0.11 %
XRF2 Al_2O_3	0.001 %	0.2 %	0.2 %
XRF2 SiO_2	6.1 %	12.4 %	13.6 %
XRF2 CaO	54.0 %	46.4 %	47.6 %
XRF2 SO_3	<.01 %	<.01 %	<.01 %

TABLE 8 (CONT.)
WHOLE-ROCK GEOCHEMICAL ANALYSES - CONCHA FORMATION

ANALYSIS	SAMPLE 4	SAMPLE 5	SAMPLE 6	AVERAGE
INAA La	6.0	3.0	4.0	3.7
INAA Ce	7.0	6.0	3.0	3.4
INAA Nd	<10.0	<10.0	<10.0	<10.0
INAA Sm	0.7	0.6	<0.5	0.38
INAA Eu	0.3	0.3	0.2	0.23
INAA Tb	<0.5	<0.5	<0.5	<0.5
INAA Yb	0.5	0.3	0.3	0.27
INAA Lu	0.08	0.05	0.05	0.04
INAA Ir	<20.0	<20.0	<20.0	<20.0
XRF1 SiO_2	13.1 %	23.9 %	6.37 %	11.3 %
XRF1 Al_2O_3	0.83 %	1.41 %	0.42 %	0.64 %
XRF1 Fe_2O_3	1.72 %	2.01 %	0.30 %	0.87 %
XRF1 CaO	32.9 %	27.0 %	51.8 %	43.3 %
XRF1 MgO	22.1 %	17.2 %	0.73 %	7.68 %
XRF1 Na_2O	0.18 %	0.12 %	0.14 %	0.15 %
XRF1 K_2O	0.21 %	0.33 %	0.09 %	0.16 %
XRF1 TiO_2	0.10 %	0.0 %	0.04 %	0.04 %
XRF1 P_2O_5	0.49 %	0.0 %	0.27 %	0.29 %
XRF1 SO_3	0.02 %	0.06 %	0.02 %	0.03 %
XRF2 Cu	0.01 %	0.01 %	0.02 %	0.02 %
XRF2 Mo	0.007 %	0.006 %	0.003 %	0.005 %
XRF2 Fe_2O_3	1.29 %	1.29 %	<.01 %	0.43 %
XRF2 Zn	0.06 %	0.05 %	0.04 %	0.06 %
XRF2 Al_2O_3	0.50 %	1.0 %	0.2 %	0.35 %
XRF2 SiO_2	14.4 %	22.6 %	8.5 %	12.9 %
XRF2 CaO	32.0 %	27.7 %	51.9 %	43.3 %
XRF2 SO_3	<.01 %	<.01 %	<.01 %	<.01 %

RAINVALLEY FORMATION

The Rainvalley formation was established by Bryant and McClymonds (1961) for about 120 meters of thin-bedded black limestone, dolomitic limestone, and sandstone exposed above the Concha limestone in the Mustang Mountains, approximately 15 kilometers NW of Sierra Vista, Arizona. No complete section of the Rainvalley is known, the thickness being controlled by post-Rainvalley erosion. The maximum thickness is 160 meters in the eastern Empire Mountains. The limestones of the Rainvalley are thinner bedded, more dolomitic, and more silty than the Concha. Chert is less abundant but shows a greater tendency to occur in beds (Bryant, 1968). Some thin sandstone and siltstone beds also occur in the Rainvalley.

The top of the Rainvalley is everywhere an erosional surface overlain in angular unconformity by Cretaceous or Cenozoic strata.

Sampling and Analysis

The Rainvalley Formation samples collected for analysis are from the southern portion of Helmet Peak, three kilometers SW of the Mission Complex, where about 150 meters of the Rainvalley outcrops. The samples were collected upsection along the crest at 25 to 30 meter intervals perpendicular to bedding. Table 9 shows the results of the four analyses run on the five Rainvalley samples.

TABLE 9
WHOLE-ROCK GEOCHEMICAL ANALYSES - RAINVALLEY FORMATION

ANALYSIS	SMPL.1	SMPL.2	SMPL.3	SMPL.4	SMPL.5	AVERAGE
ICP Ag	<0.1	0.3	<0.1	0.5	0.8	0.34
ICP Al_2O_3	0.11 %	0.32 %	0.08 %	0.32 %	0.40 %	0.25 %
ICP As	15.0	10.0	7.0	9.0	11.0	10.4
ICP Ba	55.0	16.0	59.0	52.0	24.0	41.2
ICP Be	<0.5	<0.5	<0.5	0.6	0.6	0.39
ICP Bi	<3.0	<3.0	<3.0	<3.0	<3.0	<3.0
ICP Cd	<1.0	1.0	<1.0	<1.0	<1.0	0.6
ICP Co	<1.0	<1.0	<1.0	<1.0	<1.0	<1.0
ICP Cr	11.0	26.0	7.0	36.0	35.0	23.0
ICP Cu	11.9	17.8	4.9	8.1	19.0	12.3
ICP Fe_2O_3	0.49 %	0.72 %	0.17 %	0.34 %	0.76 %	0.49 %
ICP K_2O	0.02 %	0.08 %	0.02 %	0.06 %	0.10 %	0.06 %
ICP Li	2.0	2.0	<1.0	5.0	4.0	2.7
ICP MgO	15.3 %	16.6 %	4.8 %	0.23 %	15.8 %	10.5 %
ICP MnO	0.09 %	0.17 %	0.20 %	0.09 %	0.10 %	0.13 %
ICP Mo	2.0	3.0	<1.0	2.0	3.0	2.1
ICP Na_2O	0.04 %	0.03 %	0.01 %	0.01 %	0.04 %	0.03 %
ICP Ni	7.0	10.0	<1.0	5.0	8.0	6.1
ICP P_2O_5	0.02 %	0.09 %	<.02 %	0.16 %	0.14 %	0.08 %
ICP Pb	32.0	92.0	25.0	22.0	28.0	39.8
ICP Sb	<5.0	7.0	<5.0	<5.0	<5.0	3.4
ICP Sc	<0.5	<0.5	<0.5	0.5	0.5	0.35
ICP Sn	<10.0	<10.0	<10.0	<10.0	<10.0	<10.0
ICP Sr	146.0	84.5	157.0	199.0	88.7	135.0
ICP TiO_2	<.02 %	<.02 %	<.02 %	<.02 %	<.02 %	<.02 %
ICP V	5.0	10.0	7.0	13.0	14.0	9.8
ICP W	<10.0	<10.0	<10.0	<10.0	<10.0	<10.0

TABLE 9 (CONT.)
WHOLE-ROCK GEOCHEMICAL ANALYSES - RAINVALLEY FORMATION

ANALYSIS	SAMPLE 1	SAMPLE 2	SAMPLE 3	SAMPLE 4	SAMPLE 5	AVERAGE
ICP Y	1.0	1.5	2.3	7.0	3.8	3.1
ICP Zn	97.0	210.0	73.0	85.0	150.0	123.0
ICP Zr	1.4	1.9	1.7	2.9	2.0	2.0
INAA Ag	<5.0	<5.0	<5.0	<5.0	<5.0	<5.0
INAA As	10.0	12.0	7.0	13.0	14.0	11.2
INAA Au	<5.0	9.0	8.0	<5.0	<5.0	4.9
INAA Ba	100	<100	100.	100.0	<100	80.0
INAA Br	1.0	<1.0	<1.0	<1.0	1.0	0.7
INAA CaO	33.6 %	29.4 %	42.0 %	47.6 %	29.4 %	36.4 %
INAA Co	<5.0	<5.0	<5.0	<5.0	<5.0	<5.0
INAA Cr	10.0	30.0	10.0	40.0	40.0	26.0
INAA Cs	<3.0	<3.0	<3.0	<3.0	<3.0	<3.0
INAA Fe_2O_3	0.57 %	0.86 %	0.14 %	0.43 %	0.86 %	0.57 %
INAA Hf	<1.0	<1.0	<1.0	<1.0	<1.0	<1.0
INAA Mo	<5.0	<5.0	<5.0	<5.0	<5.0	<5.0
INAA Na_2O	<675	<675	<675	<675	<675	<675
INAA Ni	<100	<100	<100	<100	<100	<100
INAA Rb	<30.0	<30.0	<30.0	<30.0	<30.0	<30.0
INAA Sb	4.8	7.1	2.5	11.0	4.7	6.0
INAA Sc	0.1	0.2	0.4	0.7	0.7	0.42
INAA Se	<5.0	<5.0	<5.0	<5.0	<5.0	<5.0
INAA Sr	<500	<500	<500	<500	<500	<500
INAA Ta	<1.0	<1.0	<1.0	<1.0	<1.0	<1.0
INAA Th	<0.5	<0.5	<0.5	<0.5	<0.5	<0.5
INAA U	1.1	1.4	1.5	2.7	1.7	1.7
INAA W	<4.0	<4.0	<4.0	<4.0	<4.0	<4.0
INAA Zn	110.0	240.0	80.0	100.0	170.0	140.0

TABLE 9 (CONT.)
WHOLE-ROCK GEOCHEMICAL ANALYSES - RAINVALLEY FORMATION

ANALYSIS	SMPL.1	SMPL.2	SMPL.3	SMPL.4	SMPL. 5	AVERAGE
INAA La	1.0	1.0	1.0	5.0	3.0	2.2
INAA Ce	<3.0	<3.0	<3.0	4.0	3.0	2.3
INAA Nd	<10.0	<10.0	<10.0	<10.0	<10.0	<10.0
INAA Sm	<0.5	<0.5	<0.5	0.6	0.5	0.37
INAA Eu	0.2	<0.2	0.2	0.2	0.2	0.2
INAA Tb	<0.5	<0.5	<0.5	<0.5	<0.5	<0.5
INAA Yb	<0.2	<0.2	<0.2	0.4	0.3	0.2
INAA Lu	<0.05	<0.05	<0.05	0.05	0.05	0.035
INAA Ir	<20.0	<20.0	<20.0	<20.0	<20.0	<20.0
XRF1 SiO_2	1.43 %	3.04 %	0.20 %	14.2 %	9.8 %	5.73 %
XRF1 Al_2O_3	0.22 %	0.56 %	0.18 %	0.43 %	0.62 %	0.40 %
XRF1 Fe_2O_3	0.6 %	0.6 %	0.16 %	0.54 %	0.76 %	0.53 %
XRF1 CaO	40.3 %	38.4 %	51.4 %	46.7 %	35.9 %	42.5 %
XRF1 MgO	22.4 %	6.88 %	6.58 %	0.31 %	6.39 %	8.51 %
XRF1 Na_2O	0.16 %	0.07 %	0.15 %	0.15 %	0.08 %	0.12 %
XRF1 K_2O	0.06 %	0.16 %	0.07 %	0.11 %	0.17 %	0.11 %
XRF1 TiO_2	0.03 %	0.01 %	0.02 %	0.04 %	0.01 %	0.02 %
XRF1 P_2O_5	0.05 %	0.12 %	0.05 %	0.18 %	0.14 %	0.11 %
XRF1 SO_3	0.02 %	0.16 %	0.02 %	0.02 %	0.15 %	0.07 %
XRF2 Cu	0.01 %	0.01 %	0.08 %	0.02 %	0.03 %	0.03 %
XRF2 Mo	.008 %	.008 %	.005 %	.002 %	.007 %	.006 %
XRF2 Fe_2O_3	0.14 %	0.43 %	<.01 %	<.01 %	0.57 %	0.23 %
XRF2 Zn	0.07 %	0.11 %	0.14 %	0.05 %	0.13 %	0.10 %
XRF2 Al_2O_3	0.1 %	0.2 %	<.01 %	0.2 %	0.3 %	0.16 %
XRF2 SiO_2	5.1 %	4.1 %	3.4 %	17.9 %	12.2 %	8.54 %
XRF2 CaO	40.9 %	38.7 %	52.1 %	46.2 %	35.2 %	42.6 %
XRF2 SO_3	<.01 %	<.01 %	<.01 %	<.01 %	<.01 %	<.01 %

SEDNORM

Differences in the normative mineral compositions of the carbonate protolith units in the Paleozoic sequence were considered as a possible means of distinguishing between formations where sight-recognition criteria fail. If this method proved successful for known units, it could then be applied to the unknowns from the project area. In order to calculate the normative mineral compositions, a computer program titled SEDNORM-A PROGRAM TO CALCULATE A NORMATIVE MINERALOGY FOR SEDIMENTARY ROCKS BASED ON CHEMICAL ANALYSES (Cohen and Ward, 1991), written in standard FORTRAN 77, was attempted. Following transcription and debugging of the ten-page program, normative mineral distributions for all 80 samples were individually calculated, as well as averages for each formation. It was hoped that using the normative mineral compositions in conjunction with the neural networks would aid in classifying the unknowns. Next the geochemical analyses and Sednorm calculations were used to construct ternary diagrams for each formation (Figs. 5-13) to determine if the elemental and mineralogical plots for the individual formations were different enough to allow their use in classifying the unknowns from the project area.

Table 10 shows the average and ranges of normative mineral composition of each formation as calculated by Sednorm.

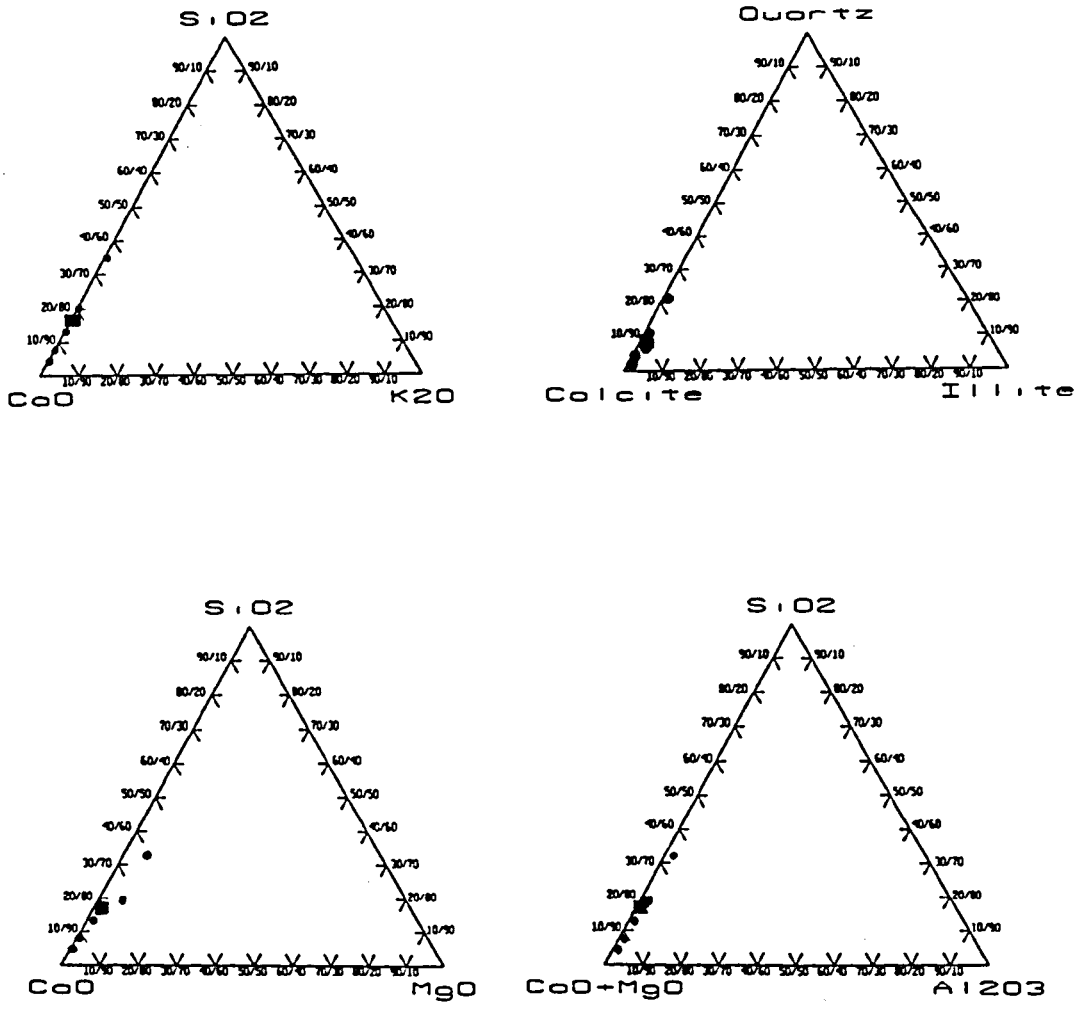

Figure 5. Ternary diagrams showing elemental and mineralogical distributions for the Abrigo Formation.

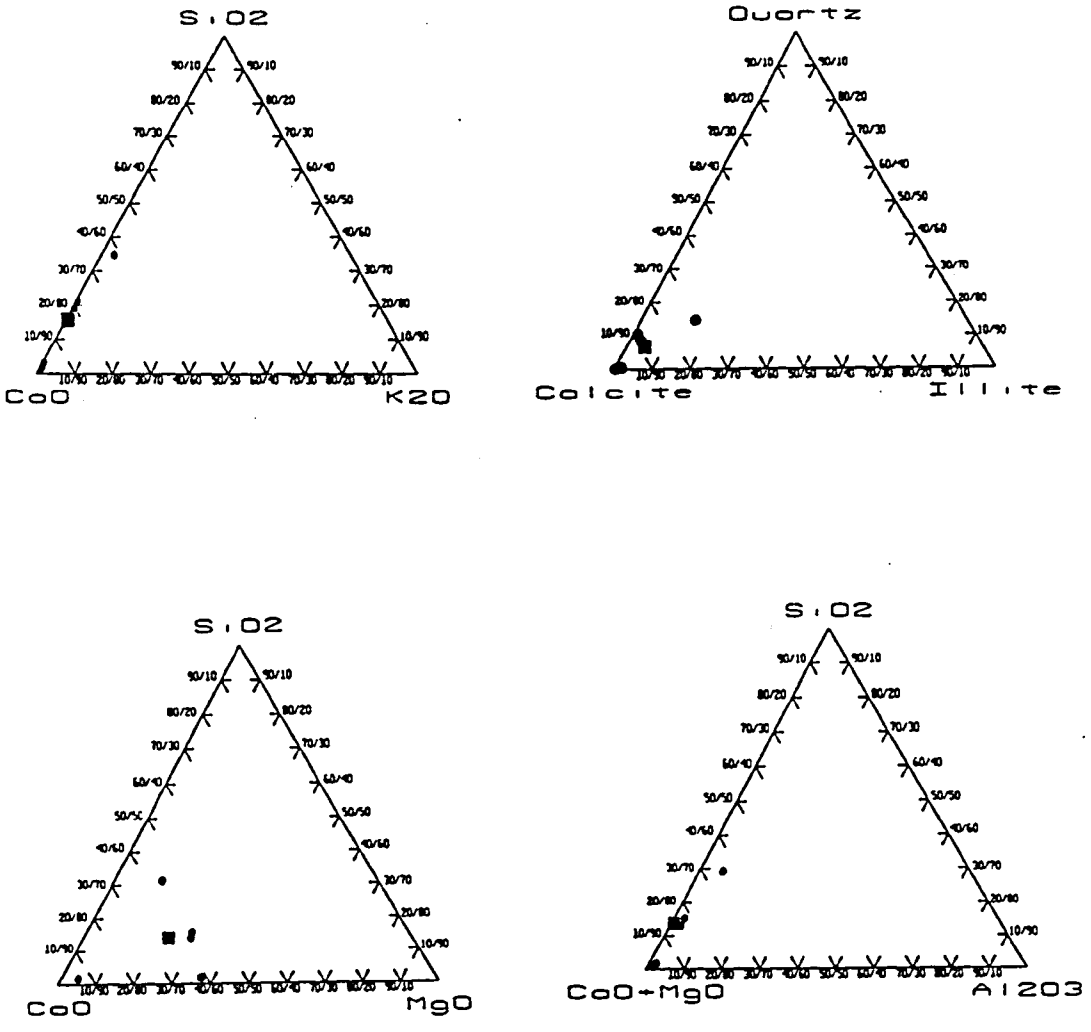

Figure 6. Ternary diagrams showing elemental and mineralogical distributions for the Martin Formation.

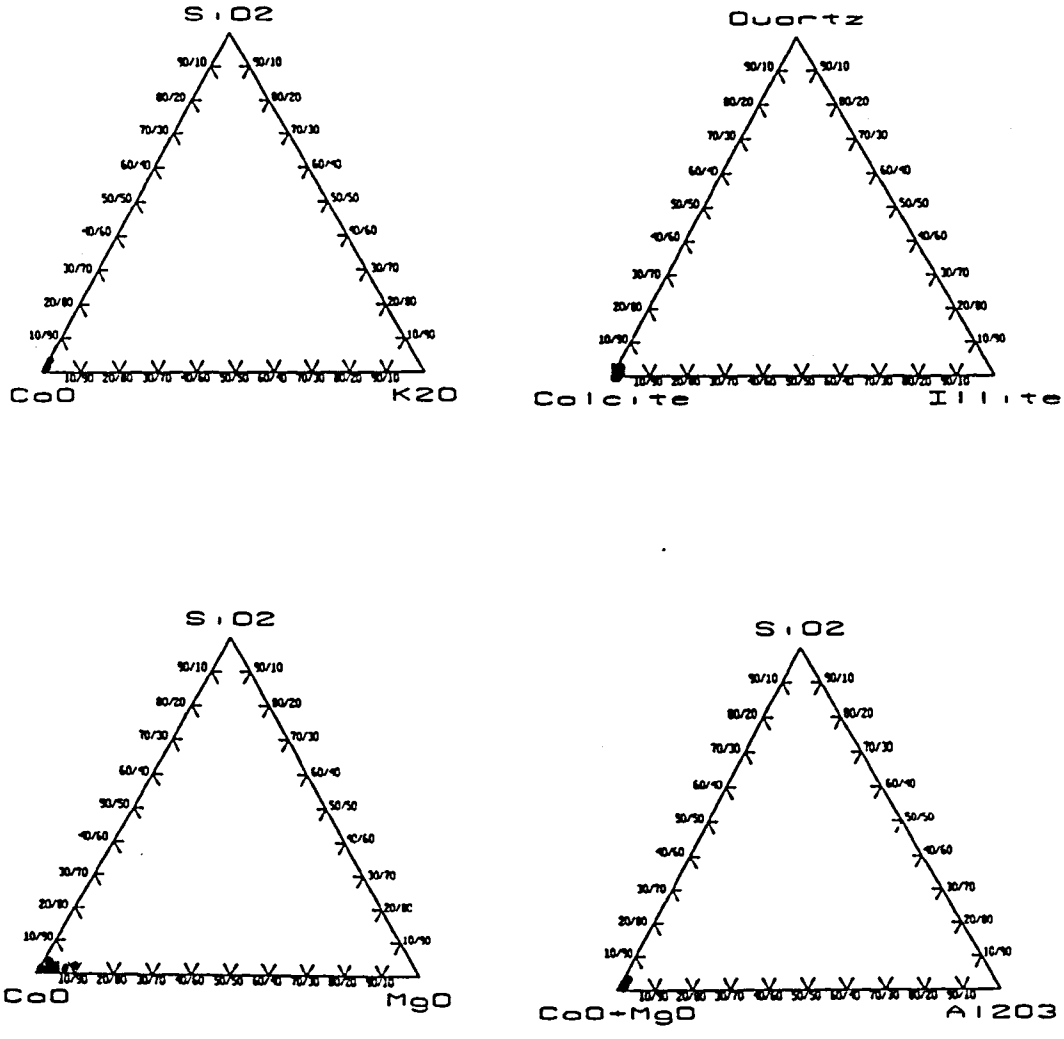

● = individual assays ■ = mean

Figure 7. Ternary diagrams showing elemental and mineralogical distributions for the Escabrosa Group.

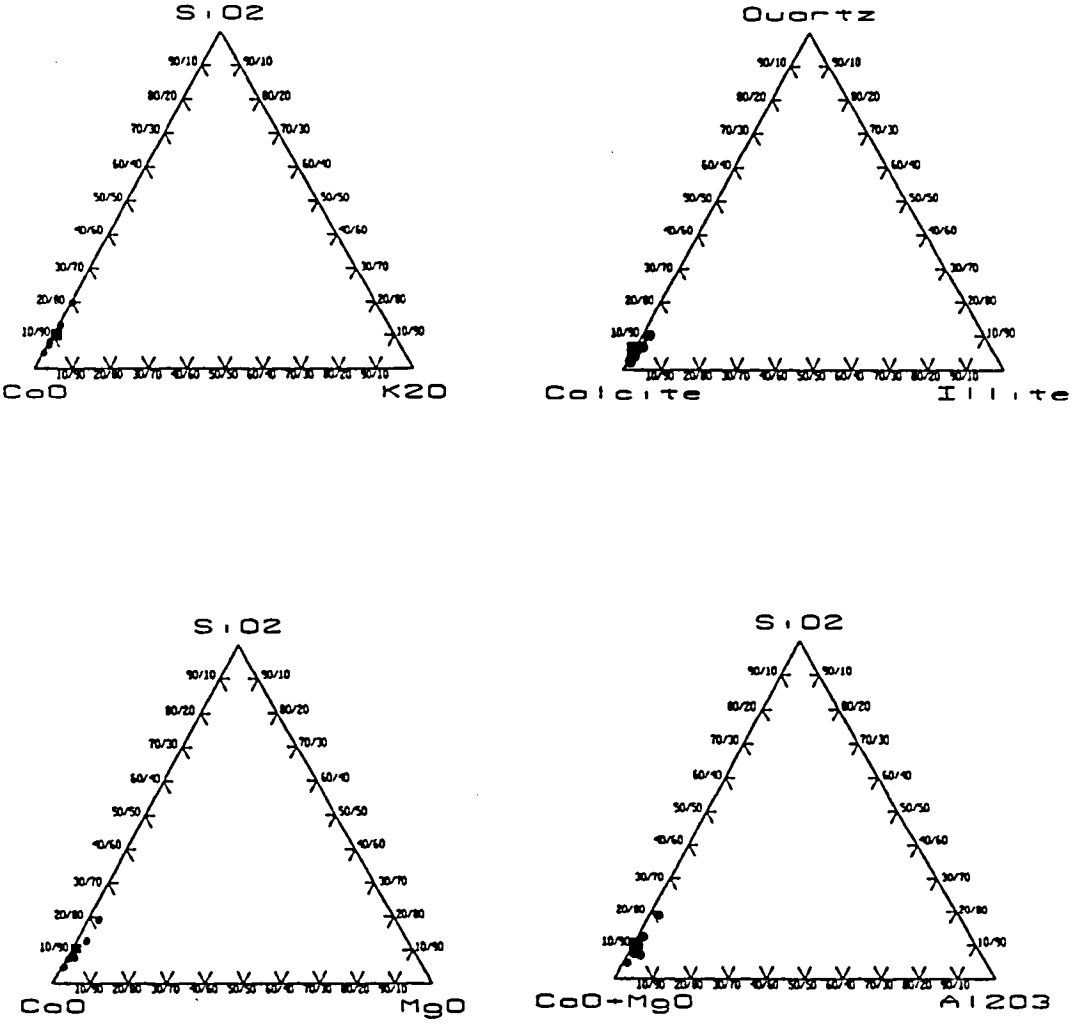

Figure 8. Ternary diagrams showing elemental and mineralogical distributions for the Horquilla Formation.

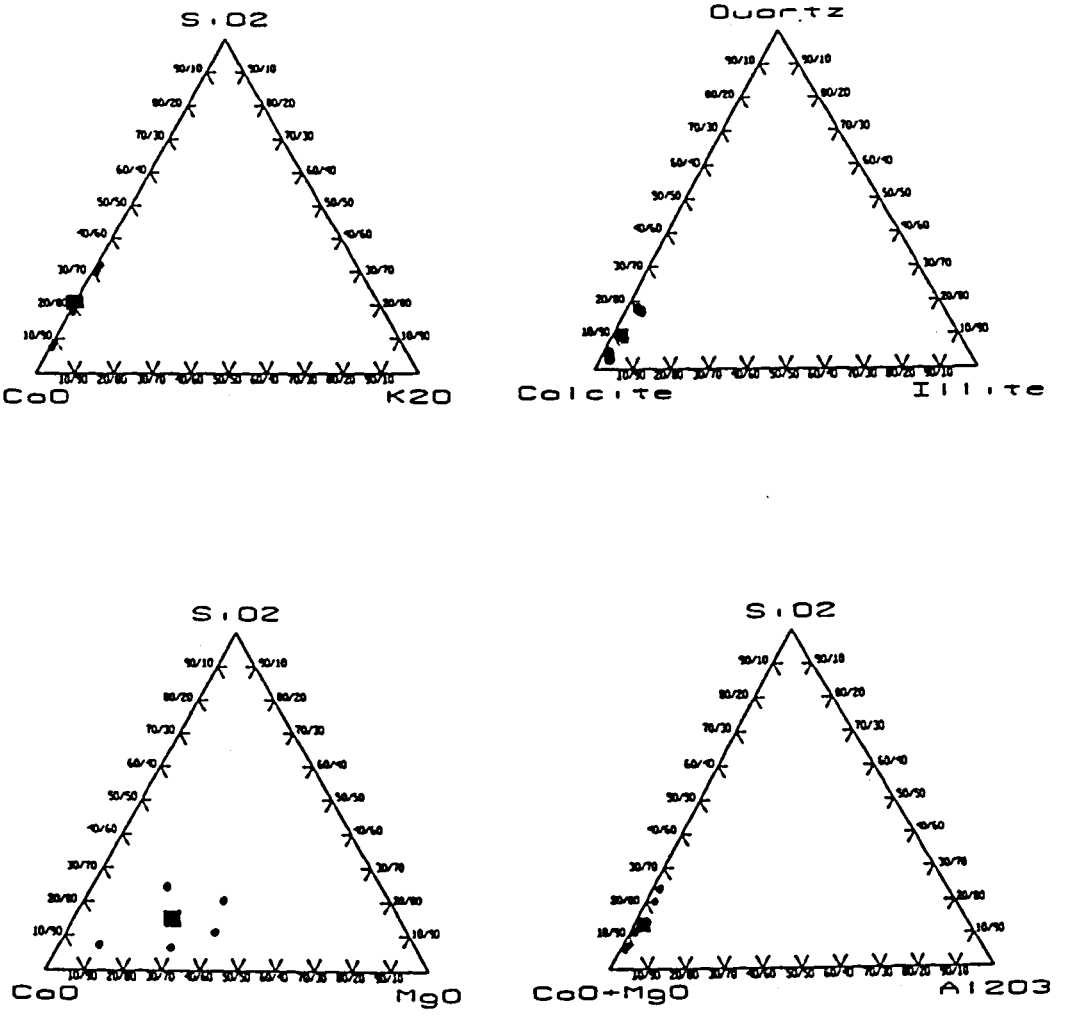

Figure 9. Ternary diagrams showing elemental and mineralogical distributions for the Colina Formation.

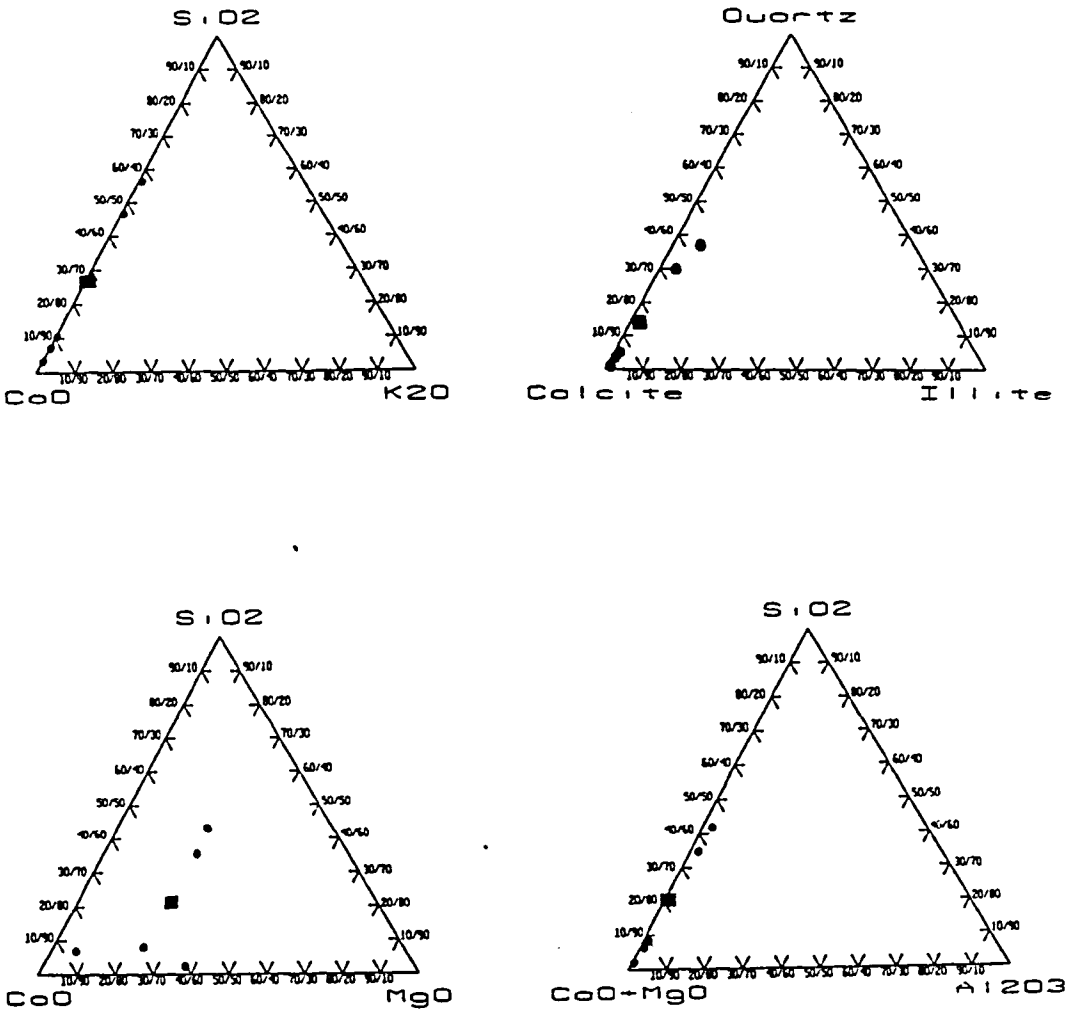

Figure 10. Ternary diagrams showing elemental and mineralogical distribution for the Epitaph Formation.

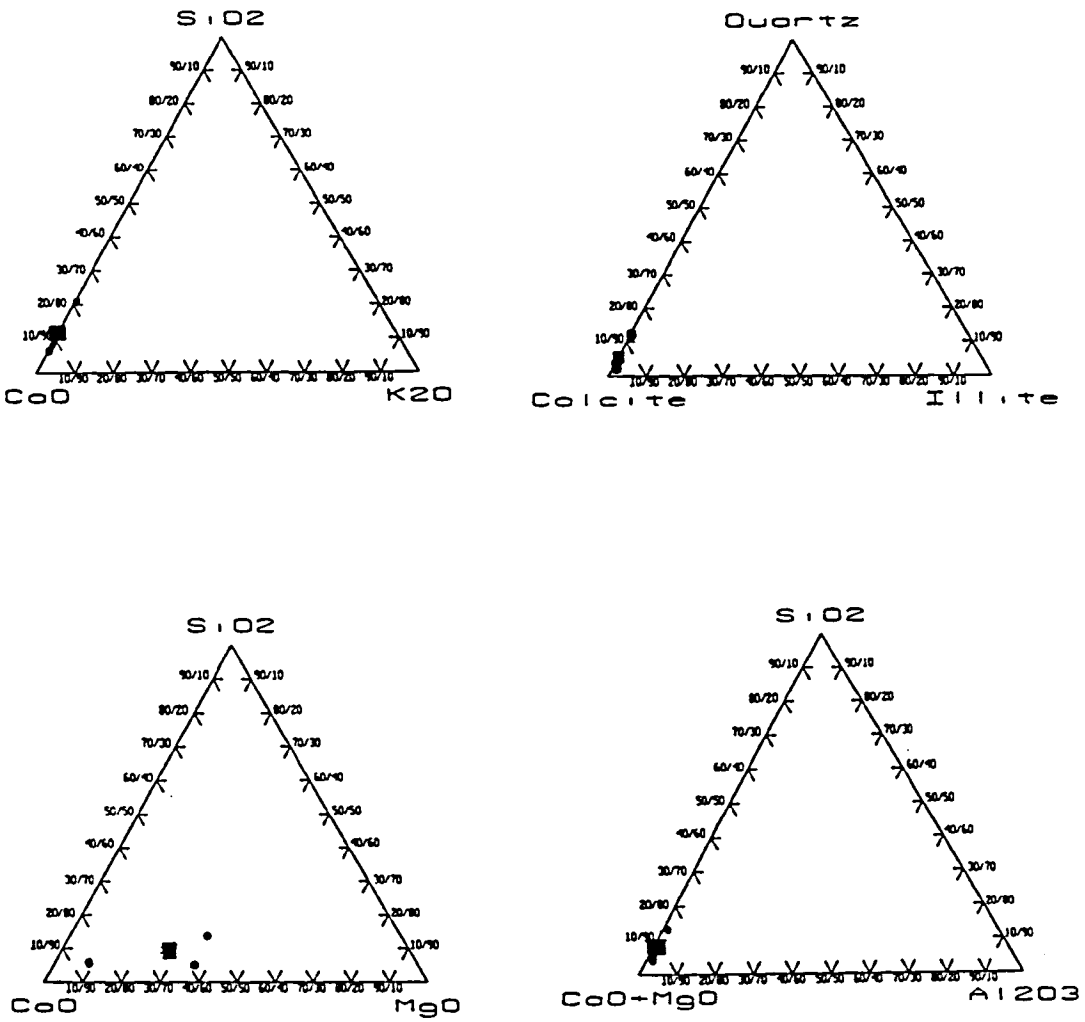

Figure 11. Ternary diagrams showing elemental and mineralogical distribution for the Scherrer Formation.

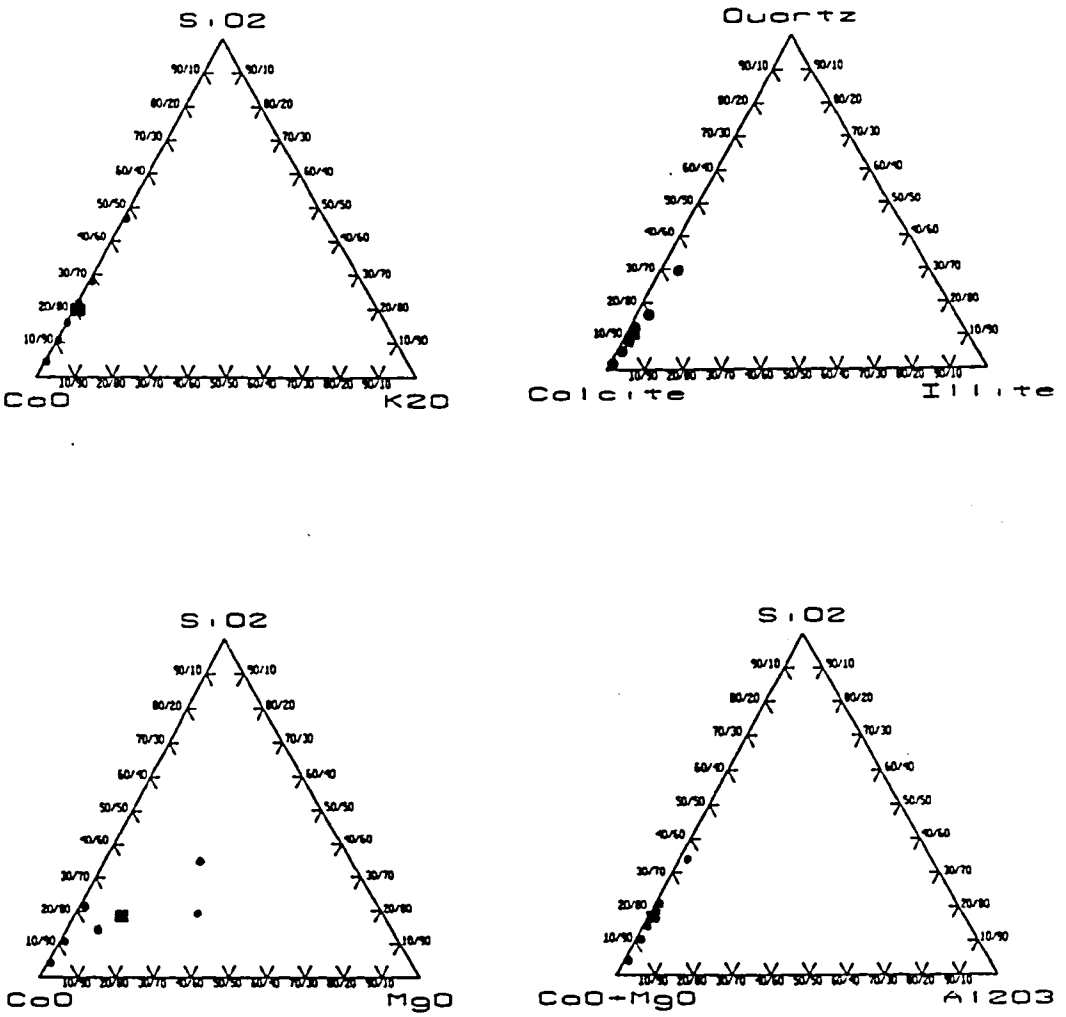

Figure 12. Ternary diagrams showing elemental and mineralogical distribution for the Concha Formation.

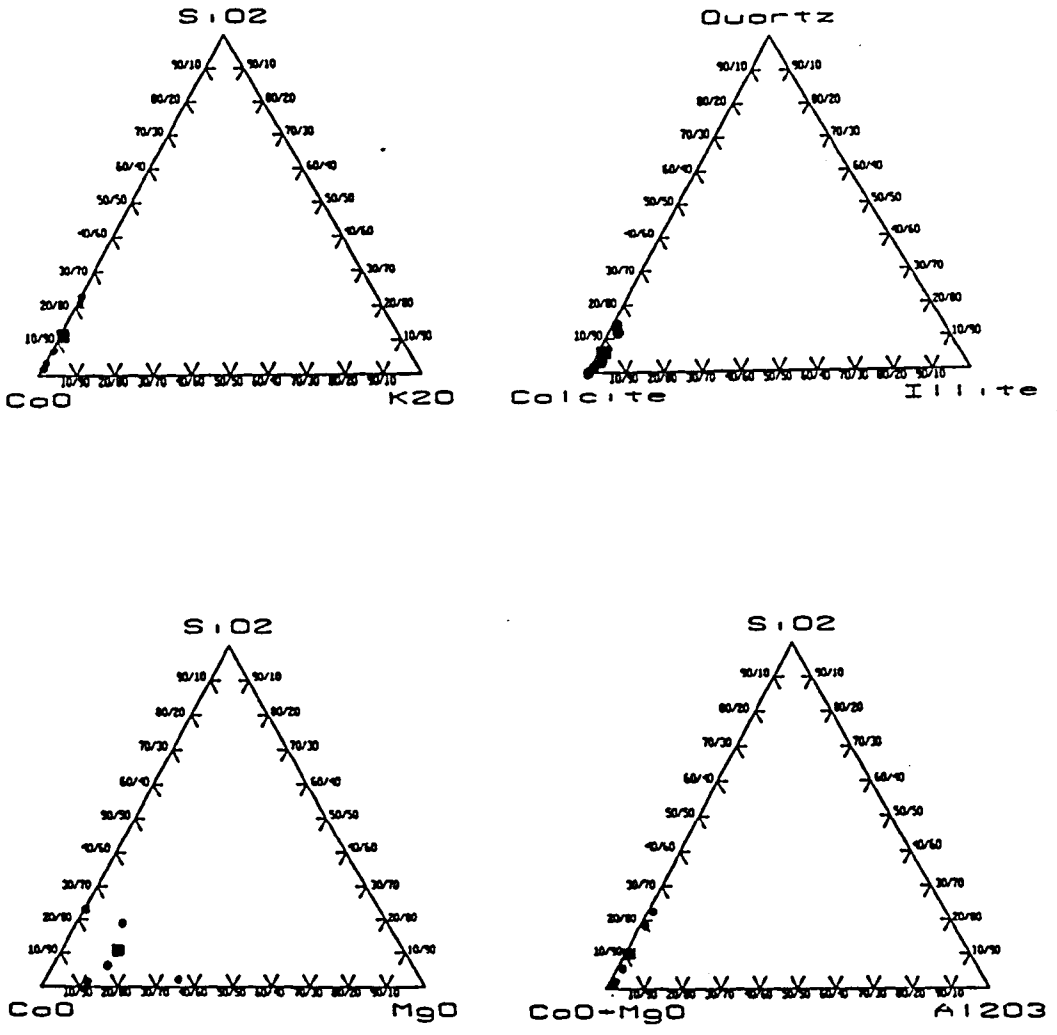

Figure 13. Ternary diagrams showing elemental and mineralogical distributions for the Rainvalley Formation.

TABLE 10
NORMATIVE MINERAL COMPOSITIONS AS COMPUTED BY SEDNORM

	FORMATIONS					
	ABRIGO		MARTIN		ESCABROSA	
MINERALS	BY MASS	BY VOL.	BY MASS	BY VOL.	BY MASS	BY VOL.
QUARTZ	8.38	8.52	5.0	5.0	0.88	0.92
RANGE	19.0 - 2.2		12.4 - 0.0		1.6 - 0.5	
ILLITE	1.24	1.20	3.30	3.10	0.58	0.58
RANGE	2.3 - 1.1		11.9 - 0.2		0.9 - 0.5	
KAOLINITE	1.04	1.06	1.06	1.06	0.0	0.0
RANGE	2.7 - 0.0		3.3 - 0.0		0.0	
CALCITE	85.1	84.8	64.8	63.7	94.4	94.1
RANGE	96.0 - 68.8		93.1 - 56.5		98.7 - 88.0	
MAGNESITE	3.78	4.06	25.5	26.8	3.90	4.20
RANGE	7.9 - 0.5		42.1 - 5.1		10.2 - 0.0	
APATITE	0.14	0.14	0.12	0.12	0.10	0.10
RANGE	0.2 - 0.1		0.3 - 0.0		0.1	
GIBBSITE	0.01	0.0	0.02	0.02	0.02	0.0
RANGE	0.01 - 0.0		0.1 - 0.0		0.1 - 0.0	
HEMATITE	0.14	0.04	0.02	0.0	0.0	0.0
RANGE	0.3 - 0.1		0.1 - 0.0		0.0	
GYPSUM	0.02	0.02	0.12	0.12	0.0	0.0
RANGE	0.1 - 0.0		0.4 - 0.0		0.0	
RUTILE	0.06	0.04	0.04	0.04	0.0	0.0
RANGE	0.1 - 0.0		0.1 - 0.0		0.0	
H_2O ADDED	0.54 %		0.78 %		0.04 %	
CO_2 ADDED	65.52 %		73.14 %		77.12 %	
EXCESS K AS OXIDE	0.04 %		0.18 %		0.0 %	

TABLE 10 (CONT.)
NORMATIVE MINERAL COMPOSITIONS AS COMPUTED BY SEDNORM

	FORMATIONS					
	HORQUILLA		COLINA		EPITAPH	
MINERALS	BY MASS	BY VOL.	BY MASS	BY VOL.	BY MASS	BY VOL.
QUARTZ	5.20	5.30	6.70	6.70	10.5	10.5
RANGE	9.4 - 2.6		12.9 - 3.0		24.8 - 0.8	
ILLITE	1.0	0.97	2.0	1.9	2.0	1.9
RANGE	1.7 - 0.6		3.1 - 1.1		5.0 - 0.4	
KAOLINITE	0.92	0.96	0.40	0.38	0.56	0.56
RANGE	2.3 - 0.0		2.0 - 0.0		1.0 - 0.2	
CALCITE	90.6	90.4	59.5	58.2	58.4	57.2
RANGE	96.3 - 82.5		82.8 - 43.6		87.5 - 37.2	
MAGNESITE	2.0	2.2	31.1	32.7	28.2	29.6
RANGE	3.6 - 0.3		43.6 - 12.1		41.9 - 7.5	
APATITE	0.14	0.14	0.10	0.10	0.10	0.10
RANGE	0.2 - 0.1		0.1		0.1	
GIBBSITE	0.0	0.0	0.02	0.0	0.06	0.02
RANGE	0.0		0.1 - 0.0		0.1 - 0.0	
HEMATITE	0.04	0.0	0.0	0.0	0.0	0.0
RANGE	0.1 - 0.0		0.0		0.0	
GYPSUM	0.0	0.0	0.0	0.0	0.02	0.02
RANGE	0.0		0.0		0.1 - 0.0	
RUTILE	0.06	0.02	0.06	0.02	0.10	0.06
RANGE	0.2 - 0.0		0.2 - 0.0		0.3 - 0.0	
H_2O ADDED	0.42 %		0.36 %		0.42 %	
CO_2 ADDED	69.4 %		74.2 %		69.3 %	
EXCESS K AS OXIDE	0.0 %		0.02 %		0.0 %	

TABLE 10 (CONT.)
NORMATIVE MINERAL COMPOSITIONS AS COMPUTED BY SEDNORM

	FORMATIONS					
	SCHERRER		CONCHA		RAINVALLEY	
MINERALS	BY MASS	BY VOL.	BY MASS	BY VOL.	BY MASS	BY VOL.
QUARTZ	3.9	3.9	9.6	9.7	5.42	5.48
RANGE	7.0 - 2.2		19.7 - 2.3		13.7 - 0.0	
ILLITE	0.33	0.30	1.50	1.40	1.14	1.08
RANGE	0.7 - 0.1		3.0 - 0.9		1.9 - 0.4	
KAOLINITE	0.83	0.83	0.30	0.30	0.08	0.08
RANGE	1.1 - 0.6		0.8 - 0.2		0.2 - 0.0	
CALCITE	63.6	62.3	73.7	73.1	75.8	74.9
RANGE	85.6 - 49.8		96.4 - 43.6		86.4 - 59.4	
MAGNESITE	30.9	32.5	14.25	15.0	16.9	17.9
RANGE	41.6 - 10.3		38.8 - 0.5		38.9 - 0.7	
APATITE	0.10	0.10	0.53	0.43	0.26	0.24
RANGE	0.1		1.0 - 0.0		0.4 - 0.1	
GIBBSITE	0.03	0.0	0.0	0.0	0.04	0.04
RANGE	0.1 - 0.0		0.0		0.1 - 0.0	
HEMATITE	0.03	0.0	0.07	0.02	0.14	0.08
RANGE	0.1 - 0.0		0.1 - 0.0		0.2 - 0.1	
GYPSUM	0.0	0.0	0.02	0.02	0.16	0.16
RANGE	0.0		0.1 - 0.0		0.4 - 0.0	
RUTILE	0.03	0.0	0.02	0.02	0.0	0.0
RANGE	0.1 - 0.0		0.1 - 0.0		0.0	
H_2O ADDED	0.43 %		0.23 %		0.22 %	
CO_2 ADDED	79.5 %		66.6 %		73.7 %	
EXCESS K AS OXIDE	0.0 %		0.0 %		0.02 %	

NEURAL NETWORK CLASSIFICATION OF LITHOLOGIC UNITS

Artificial neural network processing is a broad category of computer algorithms that solve several types of problems including classification, parameter estimation, parameter prediction, pattern recognition, completion, and association, filtering, and optimization. A neural network is a computer simulation of the way animals use neurons to process and store information. Neural networks can be simulated with sequential software, electronic circuits, or optical circuits. I used a software realization of the networks. An intriguing aspect of neural networks is their ability to perform well in doing the same types of tasks at which humans traditionally have performed well, such as pattern recognition. Neural networks have not solved problems that have remained previously intractable to humans. Rather they have, in some cases, provided faster, more accurate, more flexible solutions once a procedure has been learned. Like humans whose brain structure they imitate, artificial neural networks retain a degree of unpredictability. Unless every possible option is input, there is no way to be certain of the precise output. A related complication lies in the inability of artificial neural networks to "explain" how they solve problems. The internal representations that result from training are frequently so complex as to defy analysis, understandable

given our inability to explain how humans recognize visual patterns despite differences in distance, illumination, angle, and the passage of time. Another limitation of neural networks is their inability to classify inputs as unknown. The network will assign an output based on the output that is the closest approximation.

Neural networks are not programmed; they solve problems by learning from other solutions. Typically a neural network is given a "training set" consisting of a group of examples from which it can learn. The most commonly used training scenarios utilize "supervised learning", during which the network is presented with an input pattern together with the desired pattern of the output, the target output constituting the correct answer, or correct classification of the input data. In creating pathways from one to the other of these paired examples, the network adjusts the values of its internal pathways, or weights (Fig 14). If training is successful, the internal parameters are then adjusted such that the network can produce correct classifications in response to new input data patterns. Once trained, a network's

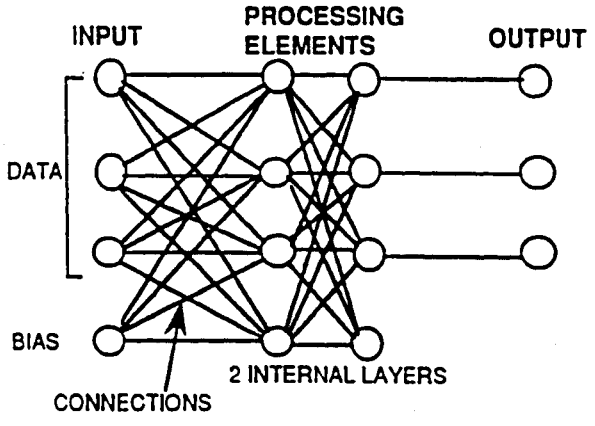

Figure 14. Flowchart of a neural network system

response can be insensitive to minor variations in its input. This ability to see through noise and distortion to the inherent pattern is vital to pattern recognition in a real-world environment. Usually, sets of training examples are presented repeatedly during training to allow the network to adjust its internal parameters gradually. The computer software responds to each example by randomly activating its circuits in a particular configuration. Any connections that produce a correct answer are reinforced and connections that produce an incorrect answer are weakened. After several thousand trials, the network activates only those circuits that produce the correct answer.

The foci of this part of the study were (1) to determine if neural networks could "learn" large, complex whole rock, major element geochemical profiles (patterns) of several Paleozoic carbonate formations and predict classifications from them of carbonate rocks whose geochemistry is known but whose formation identity is unclear, and (2) to determine if neural networks can discover which major rock-forming elements are most important in identifying lithologic units, especially in the structurally complex silicated carbonate Upper Paleozoic stratigraphic section of southern Arizona.

Artificial neural networks consist of three key components: processing elements (PEs), layers, and connections (Fig. 14). Artificial neural networks borrow the basic operating

procedures of their biological counterparts, the mammalian brain. A "neuron" or PE in a first layer receives some external stimulation that is weighted and passed through to the next layer of PEs. In my implementation of neural networks each PE received one element of the input pattern, i.e. one elemental assay from one sample. The signals coming into the PEs in the second layer were multiplied by the connection weights between the two layers and summed over all the connection weights. This sum is commonly referred to as the "activation" of the PE. The activation of the PE is modified by a transfer or activation function, and sent to the next layer of PEs. The exact form of the summation processes, transfer functions, and interconnection scheme varies according to the type of network. The memory of an artificial neural network is the values of the connection weights between PEs, that is, how they process new data in the context of the learning set. The reader is referred to several references on neural networks for more details (Caudill, 1988; Rumelhart et al, 1986; Anderson and Rosenfeld, 1989; Dayhoff, 1989; Wasserman, 1989.)

The several types of networks that work best for classification-type problems are the probabilistic neural network (Specht, 1990), the functional link network (Pao, 1989), the self-organizing map (Kohonen, 1988a), the learning vector quantization (Kohonen, 1988b), the counterpropagation

(Hecht-Nielsen, 1990), the adaptive resonance (Carpenter and Grossberg, 1987), and backpropagation (Rumelhart et al., 1986). Based on a comparison of algorithms by Poulton and Zaverton (1992) I selected the functional link (FL) and learning vector quantization (LVQ) networks for this study. The functional link network is a variant of the popular backpropagation neural network, and LVQ is a variant of the Kohonen (1988b) network. I will present only a short summary of the methods here.

BACKPROPAGATION / FUNCTIONAL LINK

Backpropagation can be regarded as a type of non-linear regression. The technique seeks a function that maps a set of input patterns to a set of output patterns with a minimum error. Derived independently by Werbos (1974) and Parker (1982), and popularized by Rumelhart et al. (1986), backpropagation is the most popular and best understood neural paradigm. It has, however, virtually no biological fidelity.

Figure 15 shows a three-layer backpropagation network. The input pattern X_{ip} is multiplied by the connection weights W_{ij}, leading to the hidden layer such that the sum at a given hidden-layer PE is

$$S_{jp}=\sum_i X_{ip}W_{ij}+\theta_j \qquad (1)$$

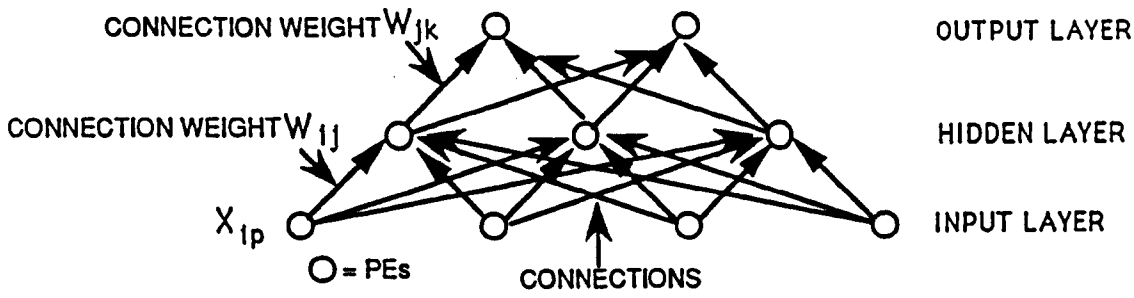

Figure 15. A three-layer backpropagation network

The sum S_j is modulated by a threshold function (TF) that is normally sigmoidal in shape (Fig. 16). This shape is recognized as being similar to the thresholding performed by biological neurons. The output of a PE is the result of applying the TF,

$$A_{jp}=f_j(S_{jp})=\frac{1}{1+e^{-S_{jp}}} \qquad (2)$$

where θ_j is a bias that shifts the threshold laterally. The bias unit has a constant value of 1.0 but trainable weights connected to each PE in the hidden and output layers. A gain term can also be applied to change the slope of the threshold. The activation of the hidden PE becomes the input to the next layer of PEs, the output layer (Figs. 14-15).

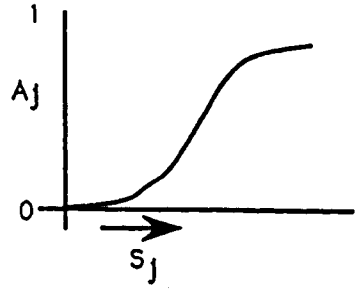

Figure 16. Threshold function shape

$$X_{jp} = A_{jp} \qquad (3)$$

The output pattern A_p is compared to the desired output

$$A_{kp}=f_k(S_{kp})=\frac{1}{1+e^{-S_{kp}}} \qquad (4)$$

$$S_{kp}=\sum_j X_{jp}W_{jk}+\theta_k \qquad (5)$$

pattern D_p to obtain the error E_p

$$E_p = (D_p - A_p) \qquad (6)$$

This error must be apportioned to all the connection weights in the network through the back-error propagation cycle. The delta weights between the output and hidden layers are computed as

$$\delta^o_{kp} = (D_{kp} - A_{kp})\ f'_k(A_{kp}) \qquad (7)$$

where f'_k is the derivative of the threshold function. In my example $f'_k = f_k(1 - f_k)$. For the hidden to input connections the error is

$$\delta^h_{jp}=f_j(A_{jp})\sum_k \delta^o_{kp}W_{jk} \qquad (8)$$

Since the error for the hidden PEs is unknown, we must use the sum of the delta weight, δ^o_{kp}, times connection weight from the output layer as the error. Weights are updated as

$$W_{ij}(t+1)=W_{ij}(t)+\eta\,\delta^h_{jp}X_{ip} \qquad (9)$$

and

$$W_{jk}(t+1) = W_{jk}(t) + \eta \delta^{o}_{kp} A_{jp} \qquad (10)$$

where t is an iteration number and η is a step size. After the weights are updated, one iteration is complete and the entire process is repeated until an acceptably small error, E_p,

$$E_p = \frac{1}{2} \sum_{k=1}^{m} \delta^{2o}_{kp} \qquad (11)$$

is achieved for each pattern. Weight updates are made after each pattern is presented or alternatively they can be accumulated over the entire training set or some subset thereof.

The role of the hidden layer has been described by Lapedes and Farber (1987) as forming decision functions or "bumps" in a manner analogous to the way a Fourier transform combines sine waves of varying amplitudes and frequencies to synthesize an arbitrary function. It is the role of the hidden PEs to generalize the input data. Too few hidden PEs will overgeneralize the mapping function, and too many PEs will fit the training data too closely (Geman et al. 1992). The error is often a quadratic function of the number of hidden PEs (Fig. 17) with a broad range of acceptable numbers of hidden

PEs.

The functional link network of Pao (1989) uses the same learning rule as standard backpropagation but seeks to improve performance by enhancing the input pattern. In some cases the enhancement makes hidden layers unnecessary. The functional links may be interaction or expansion terms. The interaction terms create an outer product from the input pattern; the expansion terms are typically a function such as sine or cosine. To produce the outer product expansion, an input pattern (x_1, x_2, x_3, x_4) would be expanded to (x_1, x_1x_2, x_1x_3, x_1x_4, x_2x_3, x_2x_4, x_3x_4, x_2, x_3, x_4). For n number of original elements in the input pattern, the outer product results in an additional (n(n-1))/2 elements. Such a large number of terms makes the functional link unwieldy for problems with large input patterns. The expansion with sines or cosines results in additions to the input pattern of say, $\sin(\pi x_1)$, $\sin(\pi x_2)$, $\sin(\pi x_3)$, $\sin(\pi x_4)$,up to $\sin(n\pi x_1)$,- - -, $\sin(n\pi x_4)$ for n expansions.

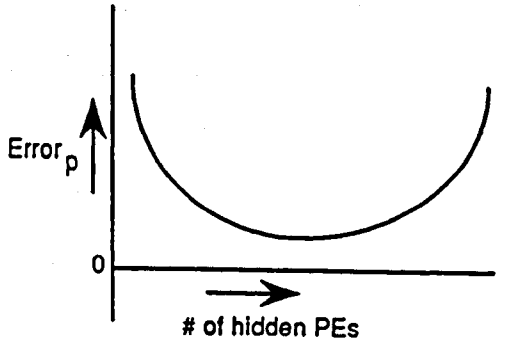

Figure 17. Shape of error function

Pao (1989) was able to synthesize a two-dimensional Gaussian function with a network containing functional expansion and outer product terms, but no hidden layers, in

half the time that it took a backpropagation network to run. I found it necessary to include a hidden layer in the functional link networks, because the functional expansion was not able to completely separate all the pattern classes. My functional link networks used an outer product plus three sine expansions and a hidden layer with nine PEs. No attempt was made to optimize the network and its size may have been excessive. A few trials to alter the number of sine expansions and number of hidden PEs resulted in no substantial changes in the results. The networks were all trained until the RMS (root mean square) error showed little change over several iterations.

LEARNING VECTOR QUANTIZATION

Learning vector quantization (LVQ) uses a Kohonen layer to perform the classification (Kohonen, 1988b). A Kohonen layer is organized quite differently than the backpropagation network previously described. Whereas backpropagation is a supervised network, meaning that an output pattern exists, a Kohonen layer is unsupervised (Fig. 18).

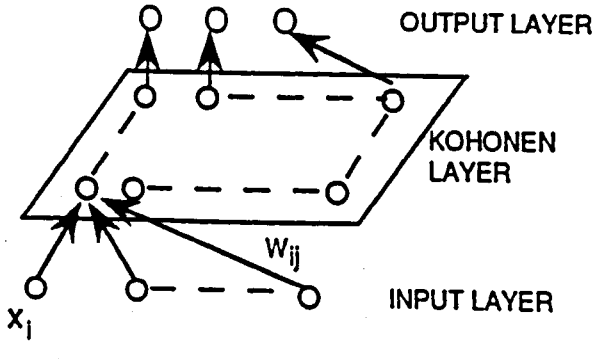

Figure 18. Illustration of Kohonen layer

Kohonen and LVQ networks use competitive learning. Only one PE is allowed to

fire so the PEs compete to determine which PE will remain active, determined as follows. In the Kohonen layer, the distance ∂_j, between a vector composed of the connection weights feeding each PE and the vector composed of the input pattern is calculated by

$$\partial_j = \| w_{ij} - x_i \| = \sqrt{\sum_{i=1}^{n} (W_{ij} - x_i)^2} \quad , \qquad (12)$$

where x is the input vector and W is the weight vector. The PE with the lowest value wins the competition.

Neighbors around the winning PE are identified and allowed to remain active as modified by the amplitude-distance function in figure 19 known as a "Mexican Hat" function. This type of network clusters the patterns in the training set so that the topology of the set is preserved in the Kohonen layer, that is, input patterns that are similar (i.e. a small distance apart) map to PEs in the Kohonen layer that are spatially near each other.

A modified Kohonen layer known as LVQ is a fast, efficient supervised classifier. It has a Kohonen layer assigned to each desired output class. Using the previously defined Euclidean distance formula (Eq. 12), the winning PE weight vector is adjusted as

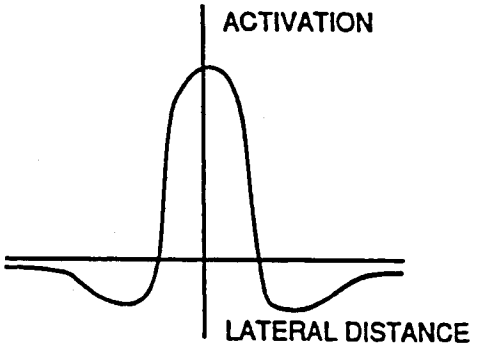

Figure 19. Amplitude-distance "Mexican Hat" function

$$W_{ij}(t + 1) = W_{ij}(t) + \eta_1(x - W_{ij}(t)) \qquad (13)$$

if the winning PE is in the correct class as defined by the training set, or

$$W_{ij}(t) - \eta_2(x - W_{ij}(t)) \qquad (14)$$

if it is not in the correct class. η_1 and η_2 are step sizes.

There are several modifications to these equations that were used in my implementation but they will not be described in detail here. These refinements, known as LVQ2 and extended LVQ, refine the solution by adjusting the second-best PE if it is in the correct class when the winning PE is not.

LVQ is a very fast algorithm, but it has the disadvantage of only outputting the integers 0 and 1 unlike FL which has floating point (real) outputs. The advantage of the floating point output is the ability to assign a "confidence" in the result based on nearness to 0 or 1.

METHOD

As previously reported, a total of 80 samples were chemically assayed, including 44 samples from nine known lithologic units, five from the Abrigo, Martin, Escabrosa, Horquilla, Colina, Epitaph, and Rainvalley Formations, three from the Scherrer, and six from the Concha. The remaining 36 samples were collected within the Mission pit or from drill core within the project area where the stratigraphic name assignments of the unit(s) were unknown. The samples were analyzed by induced neutron activation (INAA) and induction-

coupled plasma mass spectrometry (ICP) by XRAL Activation Services, Inc., and with two independent XRF analyses, one by Arizona Portland Cement, and the other by the Mission Unit assay lab. The 80 samples had 81 total analyses for 51 different elements with 30 of the analyses being replicated (Tables 1-9). In the neural network analysis, the first decisions to be made concerned the number of training samples to use and the number of elements to be included in the input pattern. Using Soulie's rule of thumb (Soulie et al, 1987), I decided to train the neural networks with three of five samples from each formation and two of three from the Scherrer formation for a total of 26 training samples. I tried to select analyses of samples from each formation that contained as many high and low values of the various elements as possible.

For the first attempt, I used all elemental analyses in the input pattern vector. A backpropagation network with 81 input PEs (the analyses), 9 output PEs (the number of formations), and a range of hidden layer PEs from 10 to 30 was tried. The network became trapped in a local error minimum and all attempts to move it failed (Fig. 20).

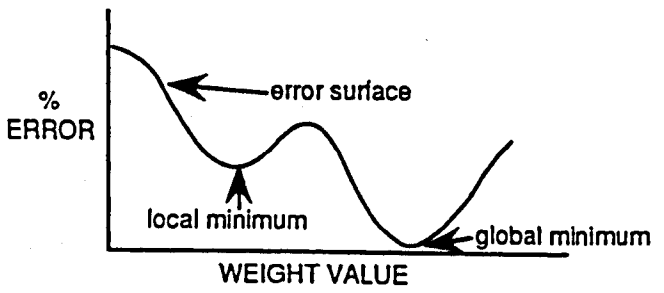

Figure 20. Illustration of local vs. global error minimum

I then designed a learning vector

quantization network with the same numbers of input and output PEs as the backpropagation network and with five PEs in the Kohonen layer dedicated to each output class. The convergence criteria for the network was an RMS error of zero, meaning that all training samples were correctly classified. The network converged in 1,563 iterations. Total training time was 19 seconds. The weights were frozen and the entire set of 44 known samples was shown to the network. The network correctly classified only 5 of the 18 samples not used for training. The poor performance could have been due to the use of too few training samples, the use of too many elements, or poor network choice. I re-trained the network on all 44 known samples, which were learned perfectly. I then removed samples one by one from each formation to determine how many samples were required to train for each formation. The results indicated that with the amount of variability in the assays, I needed three of the five samples for the Escabrosa, Martin, Rainvalley, Epitaph, and Colina formations, four of five for the Horquilla and Abrigo formations, two of three for the Scherrer formation, four of six for the Concha formation.

I next had to determine the optimum number of elements to use in the input pattern vector. Three approaches were tried: selecting elements I believed to be most diagnostic based on variation within and between formations, examining the results of the functional link network to glean insight on the most

useful elements, and finally using discriminant analysis to select elements.

I selected 24 elemental analyses to be most important based on the intra- and inter-formation variability. These, in the order inputted, were INAA CaO, XRF1 CaO, ICP Al_2O_3, XRF1 Al_2O_3, XRF1 SiO_2, XRF2 SiO_2, ICP Fe_2O_3, XRF1 Fe_2O_3, INAA As, ICP MgO, ICP MnO, ICP Ba, INAA Ce, ICP Cr, ICP Li, ICP Sc, INAA Sc, ICP Sr, ICP Pb, ICP Zr, INAA Eu, INAA Th, INAA U, and INAA Yb. An LVQ network that was trained using the 24 elements and 29 samples correctly classified 40 of the 44 known samples (12 of the 15 samples not used for training).

I attempted some variations of the inputs, including re-ordering the elements to determine if the shape of the input pattern had any effect on the network's ability to correctly classify, and using logarithmic values of the elemental assays in an attempt to increase the network's accuracy in classifying the known samples. Re-ordering the elements had no effect on the results, indicating that the network was using the individual inputs (the elemental assays) to make its classifications rather than the pattern created by the order of elements inputted. Using logarithmic values of the assays did not achieve the desired effect, increasing the classification accuracy; rather it had the reverse effect: only 36 of the 44 samples were correctly learned.

Using discriminant analysis, 26 elements were selected

using the direct method; 31 using the Mahal distance; and 33 using the maximum minimum f value. The LVQ network again correctly classified 40 of the 44 known samples. As I believed that this was the best accuracy (91 percent) that I could achieve, I then ran the 36 unknown samples through the LVQ network. The classifications were then noted on the prepared cross-sections from the project area to determine their stratigraphic believability.

GEOLOGY OF THE MINERAL HILL AREA

Within the project area, four major structural blocks exist (Fig. 21), and the geology of each will be discussed separately, as well as how they are connected.

Structural block I

Structural block I contains the upper portion of the section found within the Mission pit. The section is covered by approximately 60 meters (200 feet) of Quaternary (?) alluvium. Directly beneath the alluvium is very fine-grained chocolate-brown argillite of the Rodolfo Formation (Himes, 1973), which varies from 70 meters thick in drill hole M-350 (Fig. 2), the westernmost of the drill holes in which the argillite occurs, to 40 meters thick in M-437, the easternmost of the drill holes in which it occurs. This argillite is similar to that described from the Mission pit. The base of the argillite is a disconformity, probably a fault contact, as indicated by the drill logs and the steepness of the contact when seen in N-S cross-sections (Figs.22-23). Figures 24 and 25 show the position of the argillite in the Mineral Hill area in plan view. The upper 5 to 15 meters of the argillite is oxidized, with fracture-controlled sulfides altered to limonite and jarosite and copper mineralization occurring as chrysocolla with minor malachite and azurite. In the Mineral Hill area the

Figure 21.

STRUCTURAL BLOCKS- MINERAL HILL AREA, MISSION MINE

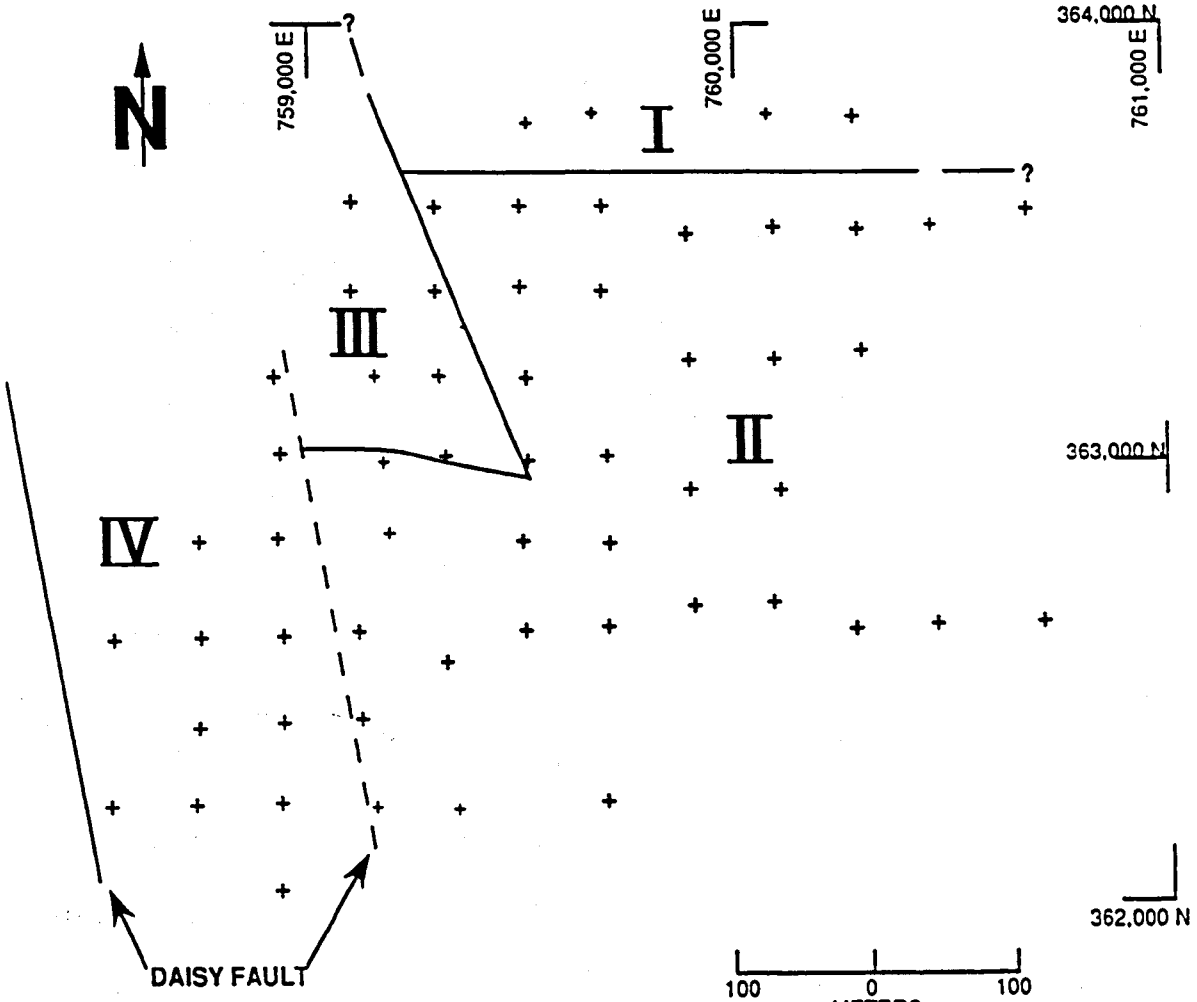

EXPLANATION

+ DRILL HOLE LOCATIONS

——— CONTACTS BETWEEN BLOCKS *

* DASHED LINES INDICATE WHERE FAULT INTERSECTS BASEMENT
SOLID LINES INDICATE SURFACE EXPRESSION

Structural block IV is footwall block west of Daisy fault

note: the faults on the S and E margin of Block III end in the SE due to intrusion of the quartz monzonite

Figure 22

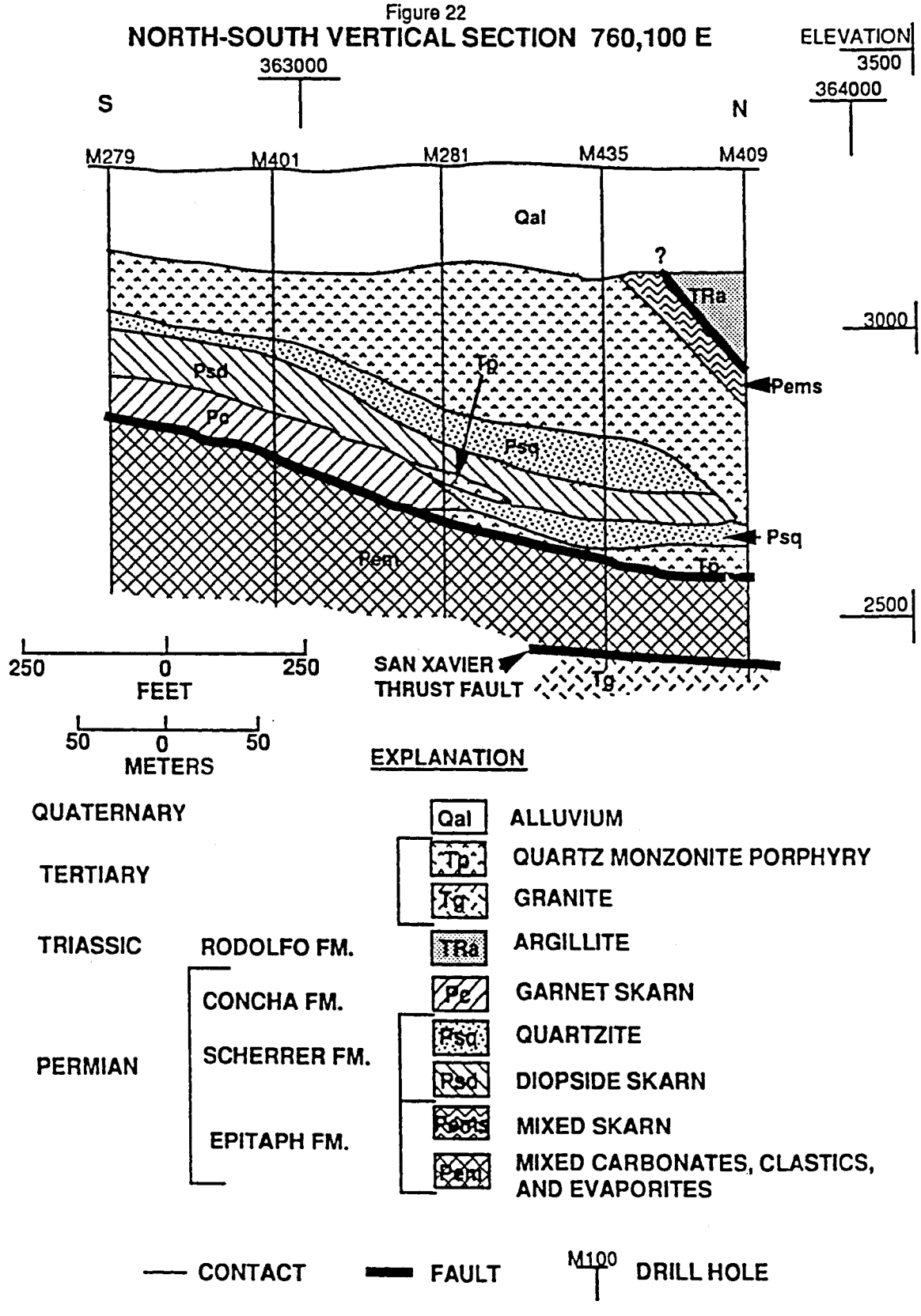
NORTH-SOUTH VERTICAL SECTION 760,100 E
ELEVATION
3500
3000
2500
363000
364000
S
N
M279
M401
M281
M435
M409
Qal
?
TRa
Pems
Psd
Pc
Tp
Psq
Pem
Tg
SAN XAVIER
THRUST FAULT
250
0
250
FEET
50
0
50
METERS
EXPLANATION
QUATERNARY
TERTIARY
TRIASSIC
RODOLFO FM.
PERMIAN
CONCHA FM.
SCHERRER FM.
EPITAPH FM.
Qal
ALLUVIUM
Tp
QUARTZ MONZONITE PORPHYRY
Tg
GRANITE
TRa
ARGILLITE
Pc
GARNET SKARN
Psq
QUARTZITE
Psd
DIOPSIDE SKARN
Pems
MIXED SKARN
Pem
MIXED CARBONATES, CLASTICS, AND EVAPORITES
CONTACT
FAULT
M100
DRILL HOLE

Figure 23

NORTH-SOUTH VERTICAL SECTION 759,500 E

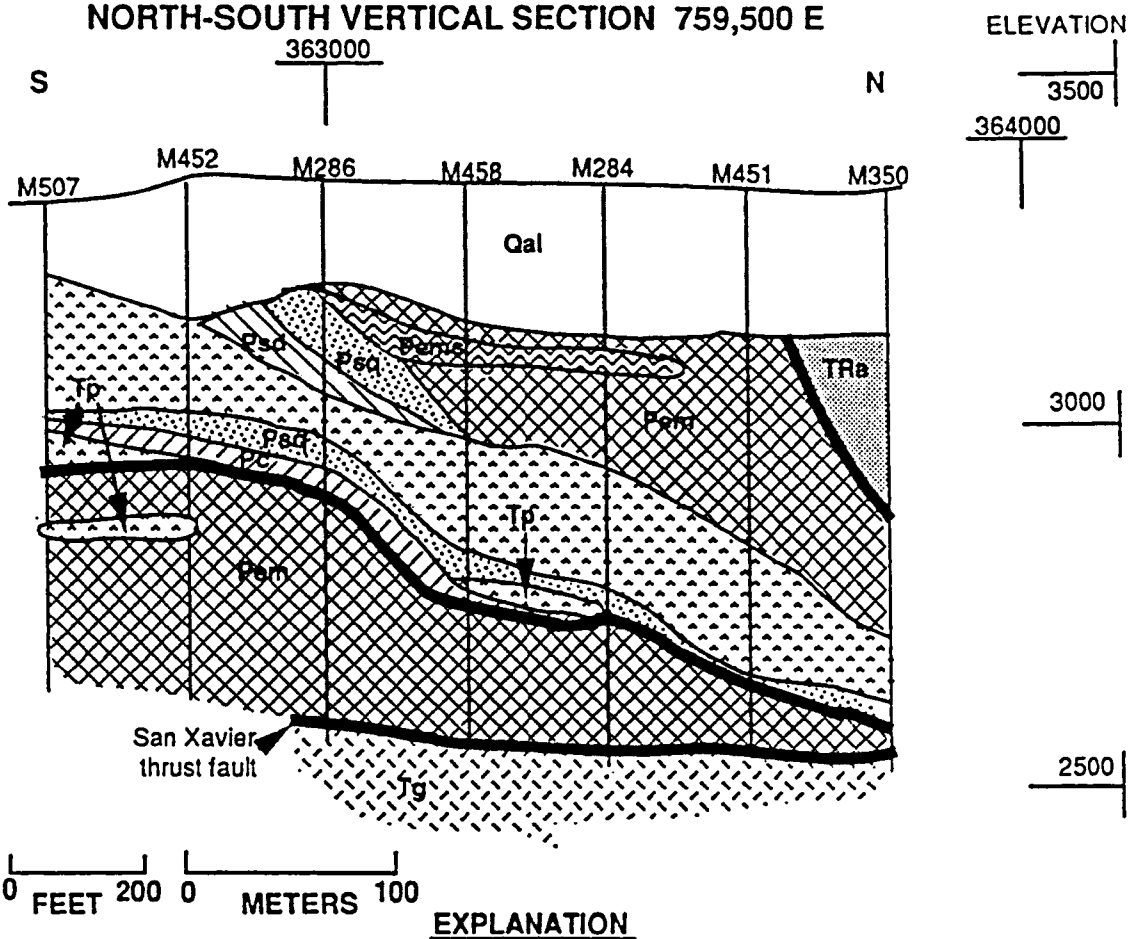

EXPLANATION

QUATERNARY		Qal	ALLUVIUM
TERTIARY		Tp	QUARTZ MONZONITE PORPHYRY
		Tg	GRANITE
TRIASSIC	RODOLFO FM.	TRa	ARGILLITE
PERMIAN	CONCHA FM.	Pc	GARNET SKARN
	SCHERRER FM.	Psq	QUARTZITE
		Psd	DIOPSIDE SKARN
	EPITAPH FM.	Pems	MIXED SKARN
		Pem	MIXED CARBONATES, CLASTICS, AND EVAPORITES

CONTACT — FAULT — M100 DRILL HOLE

Figure 24

PLAN MAP - MINERAL HILL AREA, MISSION MINE

ELEVATION 3090 FEET

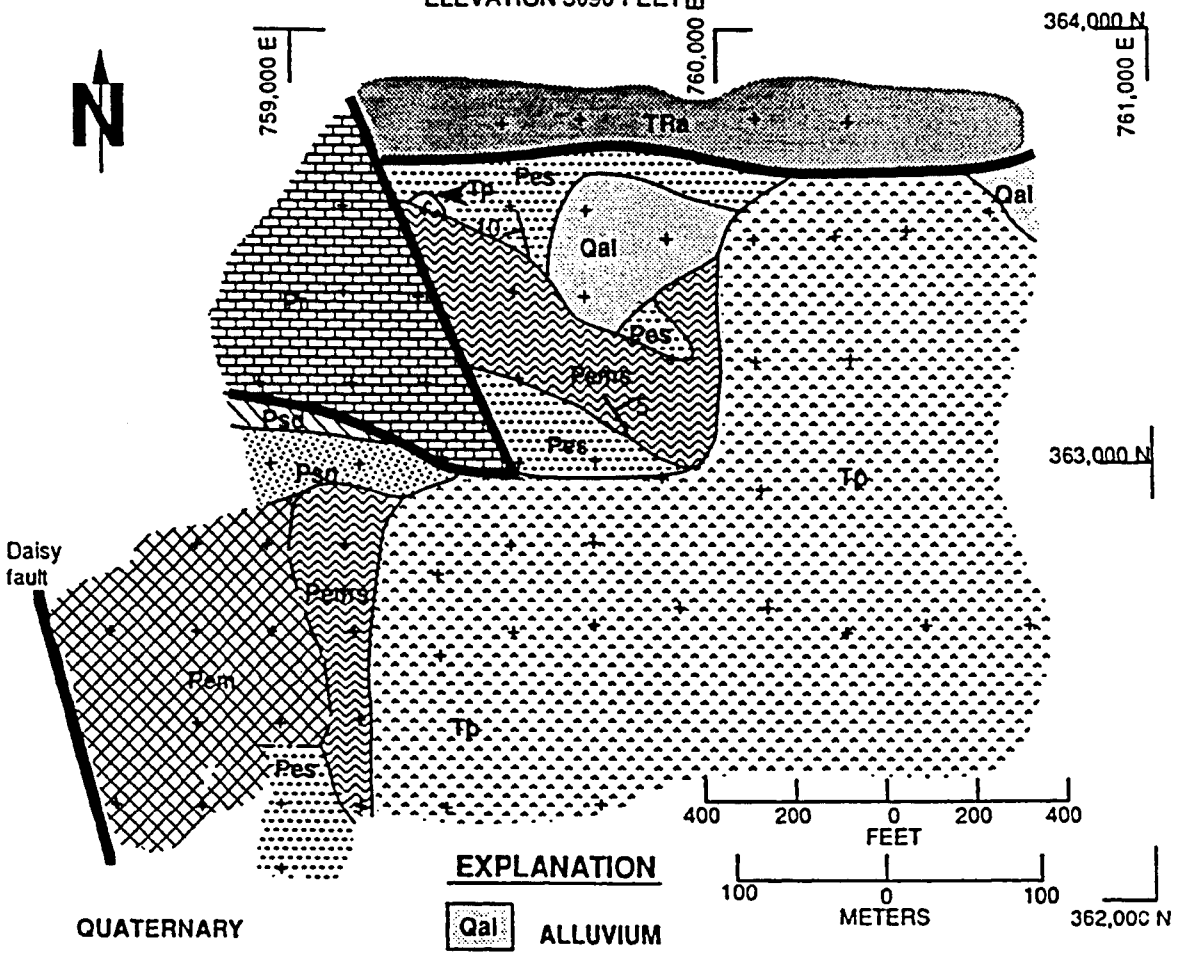

EXPLANATION

QUATERNARY		Qal	ALLUVIUM
TERTIARY		Tp	QUARTZ MONZONITE PORPHYRY
TRIASSIC	RODOLFO FM.	TRa	ARGILLITE
PERMIAN	RAINVALLEY FM.?	Pz	MARBLE
	CONCHA FM.	Pc	GARNET SKARN
	SCHERRER FM.	Psq	QUARTZITE
		Psd	DIOPSIDE SKARN
	EPITAPH FM.	Pes	SILTSTONE
		Pems	MIXED SKARN
		Pem	MIXED CARBONATES, CLASTICS, AND EVAPORITES

+ DRILL HOLE LOCATIONS — CONTACT — FAULT — 5 APPROXIMATE STRIKE AND DIP

Figure 25

PLAN MAP - MINERAL HILL AREA, MISSION MINE

ELEVATION 2970 FEET

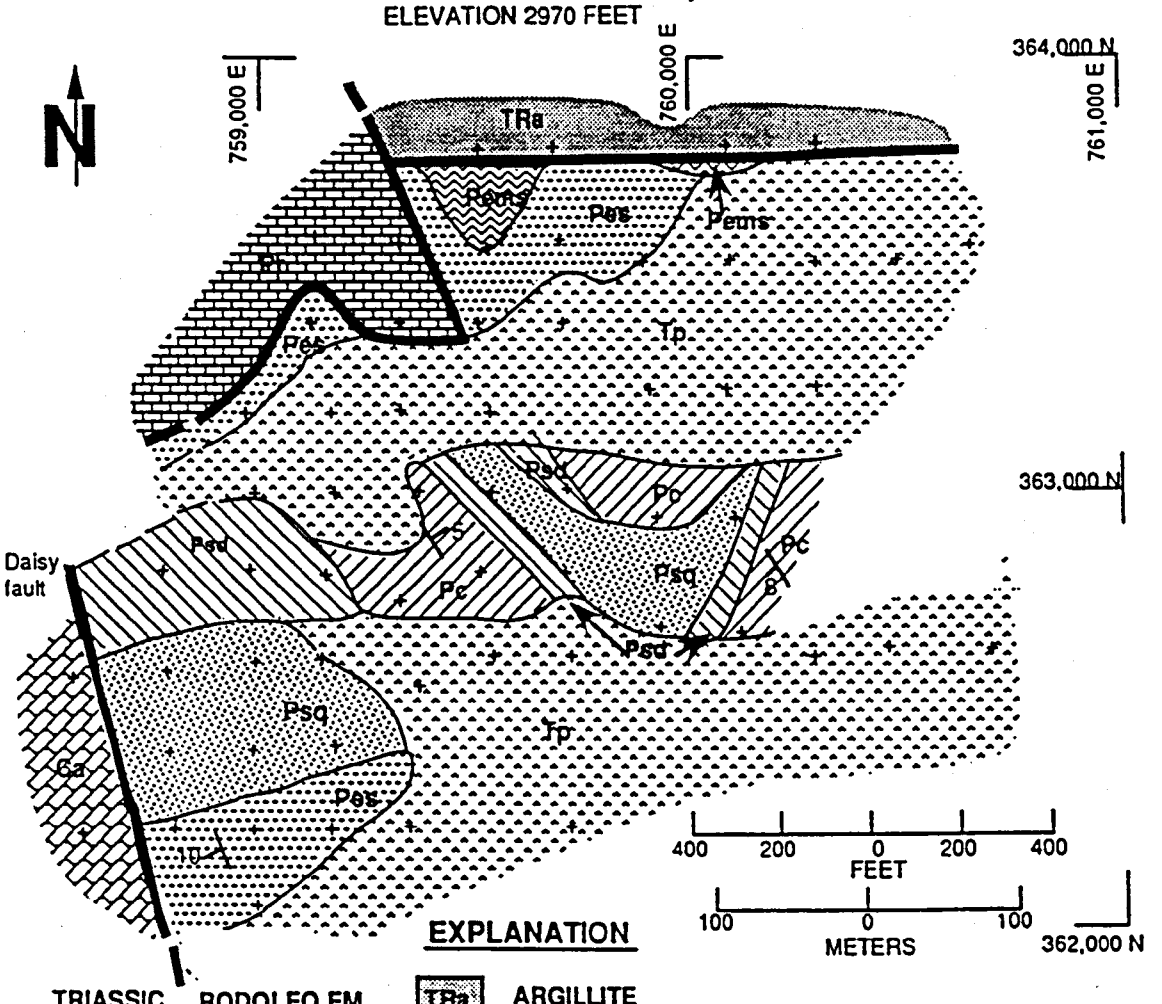

EXPLANATION

TRIASSIC	RODOLFO FM.	TRa	ARGILLITE
TERTIARY		Tp	QUARTZ MONZONITE PORPHYRY
PERMIAN	RAINVALLEY FM. ?	Pr	MARBLE
	CONCHA FM.	Pc	GARNET SKARN
	SCHERRER FM.	Psq	QUARTZITE
		Psd	DIOPSIDE SKARN
	EPITAPH FM.	Pes	SILTSTONE
		Pens	MIXED SKARN
CAMBRIAN	ABRIGO FM.	Ca	CARBONATES AND ALTERED CARBONATES

\+ DRILL HOLE LOCATIONS — CONTACT — FAULT 5 APPROXIMATE STRIKE AND DIP

argillite only rarely contains intercepts of ore-grade material, generally averaging between 0.10 % and 0.20 % Cu.

Beneath the argillite is green-brown siltstone and interbedded siltstone-anhydrite of the Epitaph Formation, the upper portion of which is approximately 60 meters thick to the west in drill hole M-350, thinning to the east to 15 meters in drill hole M-409, where an increase in limey/dolomitic interbeds cause the unit to be mainly diopside and garnet skarn interbedded with anhydrite. In this structural block, the Epitaph Formation strikes N-NW and dips 5-10° NE. The upper portion of the unit pinches out entirely farther east, and the base of the argillite contacts with quartz monzonite porphyry in drill hole M-437. In structural block I, the intrusion of the quartz monzonite porphyry is entirely within the Epitaph Formation. Several "fingers" of the quartz monzonite intrude the Epitaph Formation in this section, with sections of garnet/diopside skarn-anhydrite and siltstone-anhydrite occurring above, within, and below the sill-like intrusion of quartz monzonite porphyry (Fig. 22). The quartz monzonite "sill" apparently is continuous from the outcropping found in the western portion of the Mission pit,and dips approximately 15° to the NW in this block, and varies from 30 meters thick in the west (drill hole M-350) to 125 meters thick in the east (drill hole M-473).

Below the porphyry, the Epitaph Formation consists of

interbedded siltstone-anhydrite, garnet/diopside skarn, and fine-grained gray marble with thin bands of serpentine. It has been noted that where this banding effect occurs within limestone the calc-silicate alteration has resulted in garnet bands, and where it occurs within dolomite or high-magnesium limestone the calc-silicate alteration resulted in serpentine.

The lower contact of the Epitaph Formation in structural block I is the Tertiary San Xavier thrust fault at an elevation of 2530 feet in drill hole M-350 in the west, dipping approximately 10° E to an elevation of 2380 feet in drill hole M-437. In drill core the San Xavier fault generally occurs as 0-1 meters of broken or brecciated upper unit, followed by 0-1 meters of fault gouge, followed by broken or brecciated lower-plate Tertiary granodiorite believed to be the Ruby Star Granodiorite of Cooper (1960), which becomes progressively less broken downward. The micas in this granodiorite are intensely chloritized in the vicinity of the fault, becoming less altered downward.

Structural block II

Structural block II contains the same overturned Paleozoic metasedimentary sequence as is found in the Mission pit, namely the Epitaph, Scherrer, and Concha Formations, intruded by the Tertiary quartz monzonite porphyry. The section is overlain by 10 to 60 meters of Quaternary (?) alluvium. The

upper portion of the Mission sequence, the Triassic Rodolfo Formation argillite, does not occur in structural block II. In block II, the Permian metasedimentary units strike N-NW and dip 5-10° NE to 5-10° SW. The quartz monzonite porphyry sill that intrudes the sequence is irregular, but generally dips to the north and west at a shallow angle. On Figures 24-28 this feature is expressed by the porphyry advancing to the north and west further downsection. The porphyry sill is thickest to the east with a maximum thickness of 120 meters in drill hole M-436, thinning to the east to 45 meters in drill hole M-466 (Fig. 29).

Above the quartz monzonite porphyry sill, the Paleozoic sequence consists of up to 90 meters of Epitaph Formation siltstone, carbonates, and minor interbedded garnet and diopside skarn (Figs. 29-31). Below the porphyry the upper (stratigraphically lower) Scherrer Formation orthoquartzite reaches a maximum thickness of 45 meters in drill hole M-385 (Fig. 30), thinning to the east and west. Below the quartzite is the middle Scherrer diopside skarn, approximately 18 meters at its thickest point. Underlying the diopside skarn is up to 40 meters of Concha Formation garnet skarn and marble, thickest to the east, that pinches out to the west against the porphyry intrusive or is cut off by a low-angle fault. This fault could be a thrust, pre-existing or contemporaneous with the San Xavier fault, which caused the Scherrer and Concha

Figure 26

PLAN MAP - MINERAL HILL AREA, MISSION MINE

ELEVATION 2850 FEET

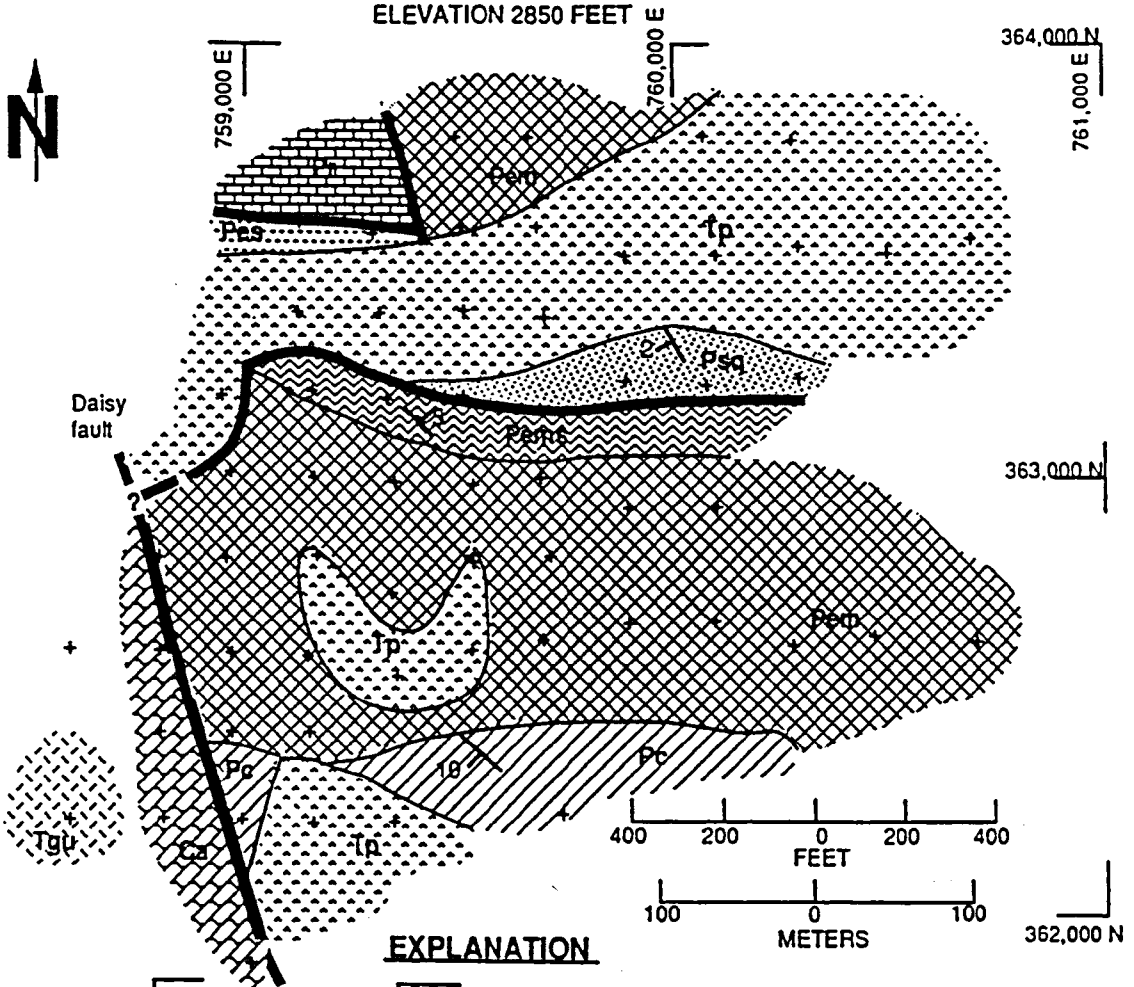

EXPLANATION

TERTIARY	Tp	QUARTZ MONZONITE PORPHYRY
	Tgu	GRANITE (UPPER PLATE)
PERMIAN	RAINVALLEY FM.? Pr	MARBLE
	CONCHA FM. Pc	GARNET SKARN
	SCHERRER FM. Psq	QUARTZITE
	EPITAPH FM. Pes	SILTSTONE
	Pcm	MIXED SKARN
	Pem	MIXED CARBONATES, CLASTICS, AND EVAPORITES
CAMBRIAN	ABRIGO FM. Ca	CARBONATES AND ALTERED CARBONATES

+ DRILL HOLE LOCATIONS — CONTACT — FAULT — 45 APPROXIMATE STRIKE AND DIP

Figure 27

PLAN MAP - MINERAL HILL AREA, MISSION MINE

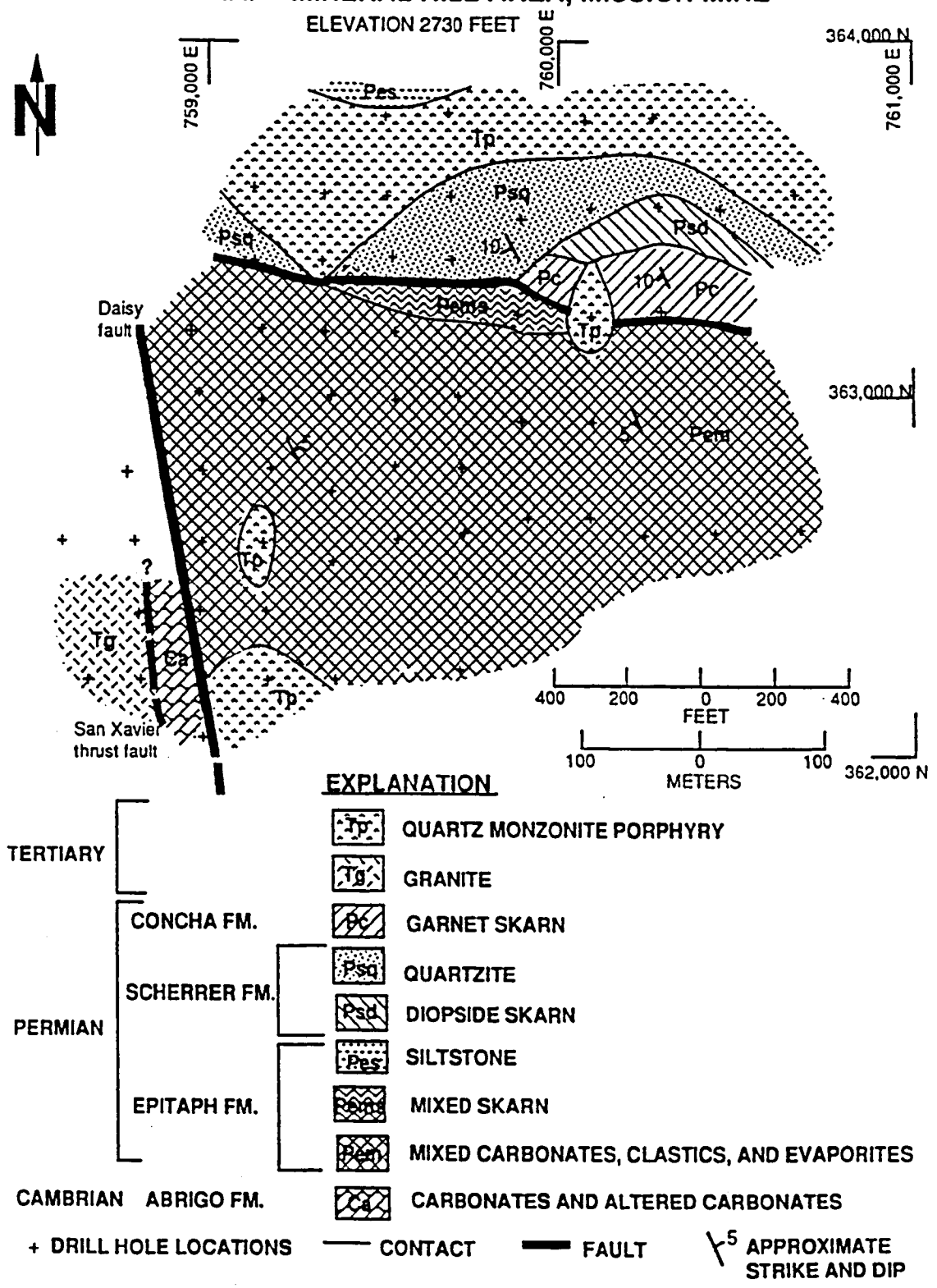

Figure 28

PLAN MAP - MINERAL HILL AREA, MISSION MINE

ELEVATION 2610 FEET

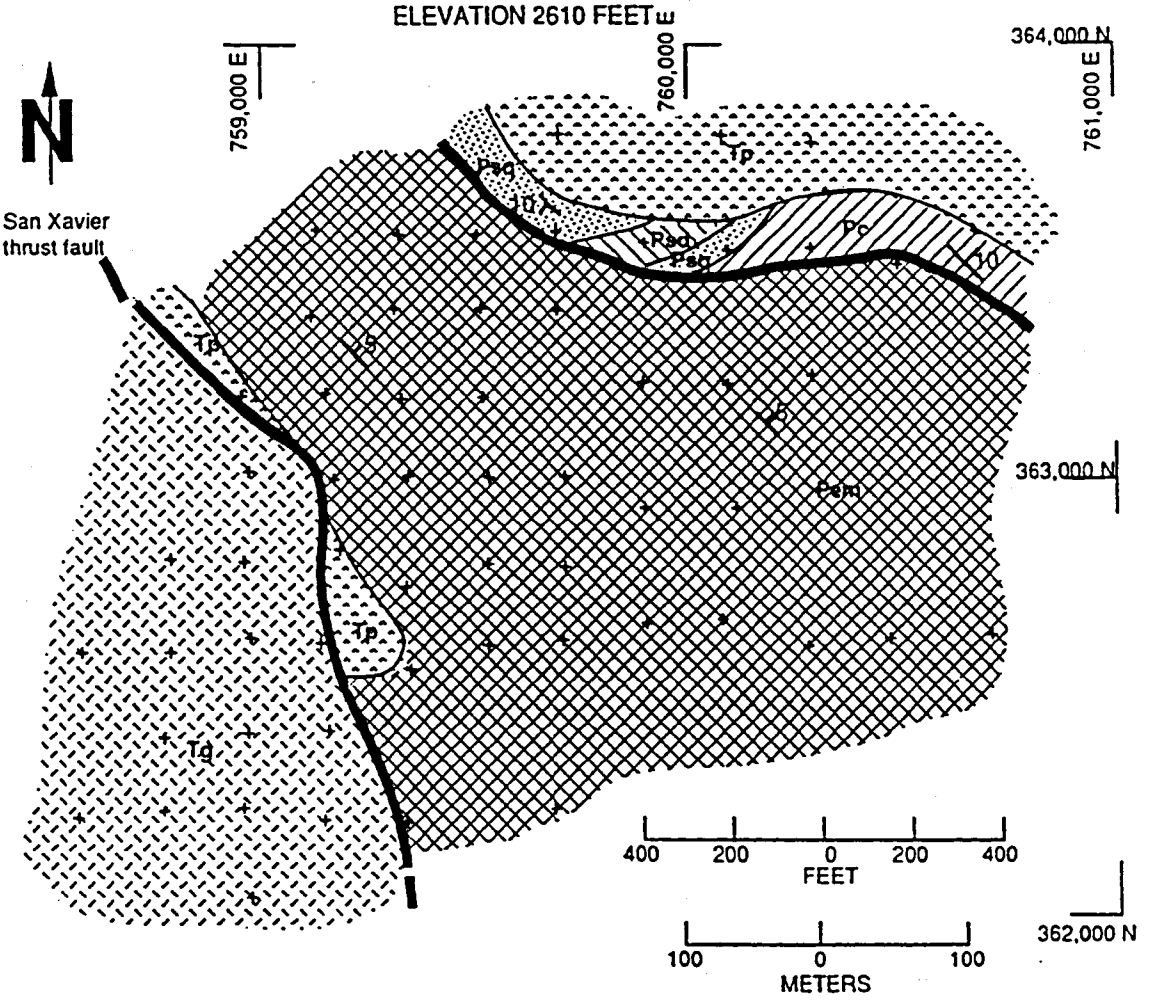

EXPLANATION

TERTIARY	Tp	QUARTZ MONZONITE PORPHYRY
	Tg	GRANITE
PERMIAN — CONCHA FM.	Pc	GARNET SKARN
PERMIAN — SCHERRER FM.	Psq	QUARTZITE
	Psd	DIOPSIDE SKARN
PERMIAN — EPITAPH FM.	Pem	MIXED CARBONATES, CLASTICS, AND EVAPORITES

+ DRILL HOLE LOCATIONS — CONTACT — FAULT — 5 APPROXIMATE STRIKE AND DIP

Figure 30

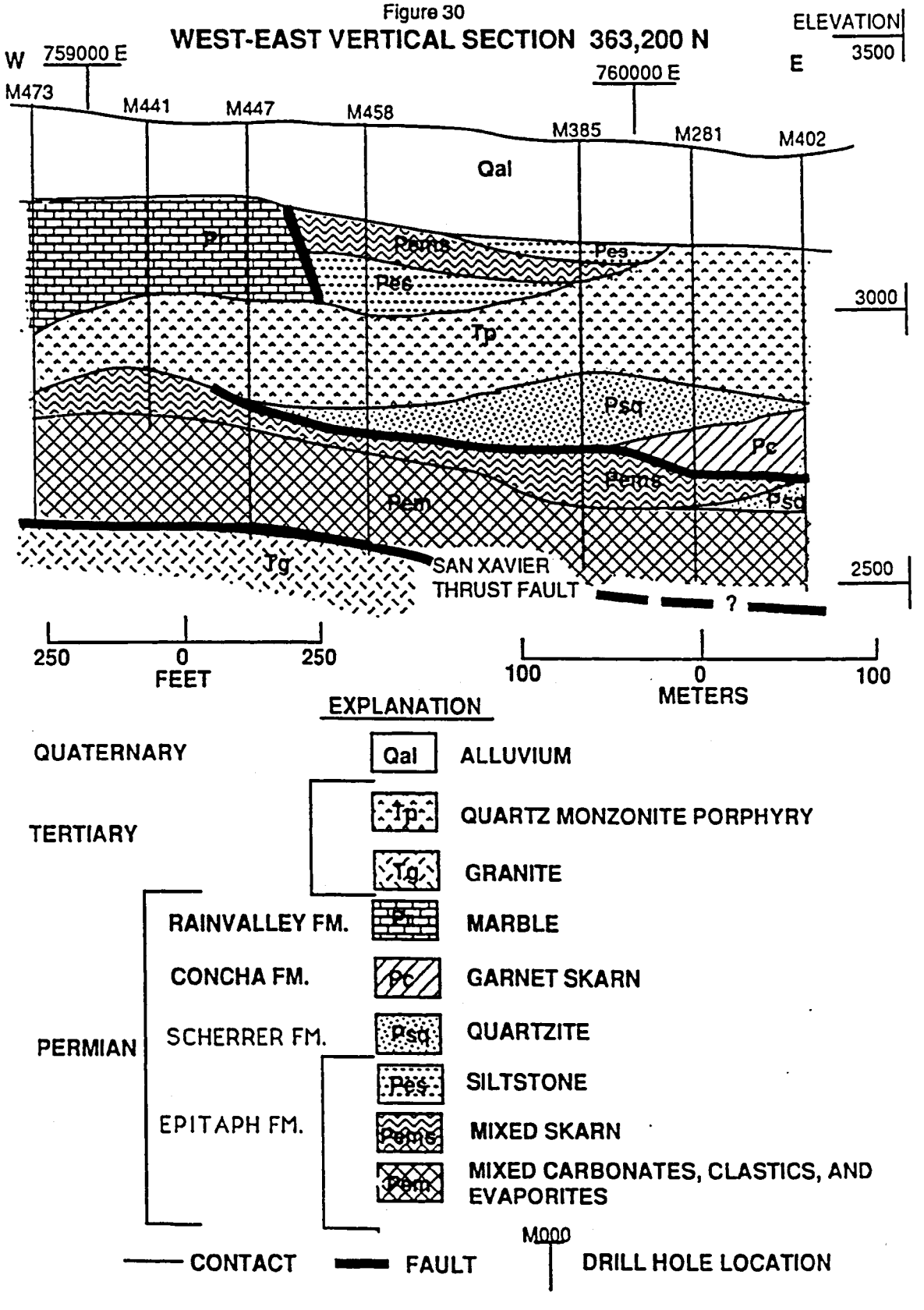
WEST-EAST VERTICAL SECTION 363,200 N
ELEVATION
3500
3000
2500
W
759000 E
760000 E
E
M473
M441
M447
M458
M385
M281
M402
Qal
Pr
Pems
Pes
Pes
Tp
Psq
Pc
Pems
Psq
Pem
Tg
SAN XAVIER
THRUST FAULT
?
250
0
250
FEET
100
0
100
METERS
EXPLANATION
QUATERNARY
Qal
ALLUVIUM
TERTIARY
Tp
QUARTZ MONZONITE PORPHYRY
Tg
GRANITE
RAINVALLEY FM.
Pr
MARBLE
CONCHA FM.
Pc
GARNET SKARN
PERMIAN
SCHERRER FM.
Psq
QUARTZITE
Pes
SILTSTONE
EPITAPH FM.
Pems
MIXED SKARN
Pem
MIXED CARBONATES, CLASTICS, AND EVAPORITES
M000
CONTACT
FAULT
DRILL HOLE LOCATION

Figure 31

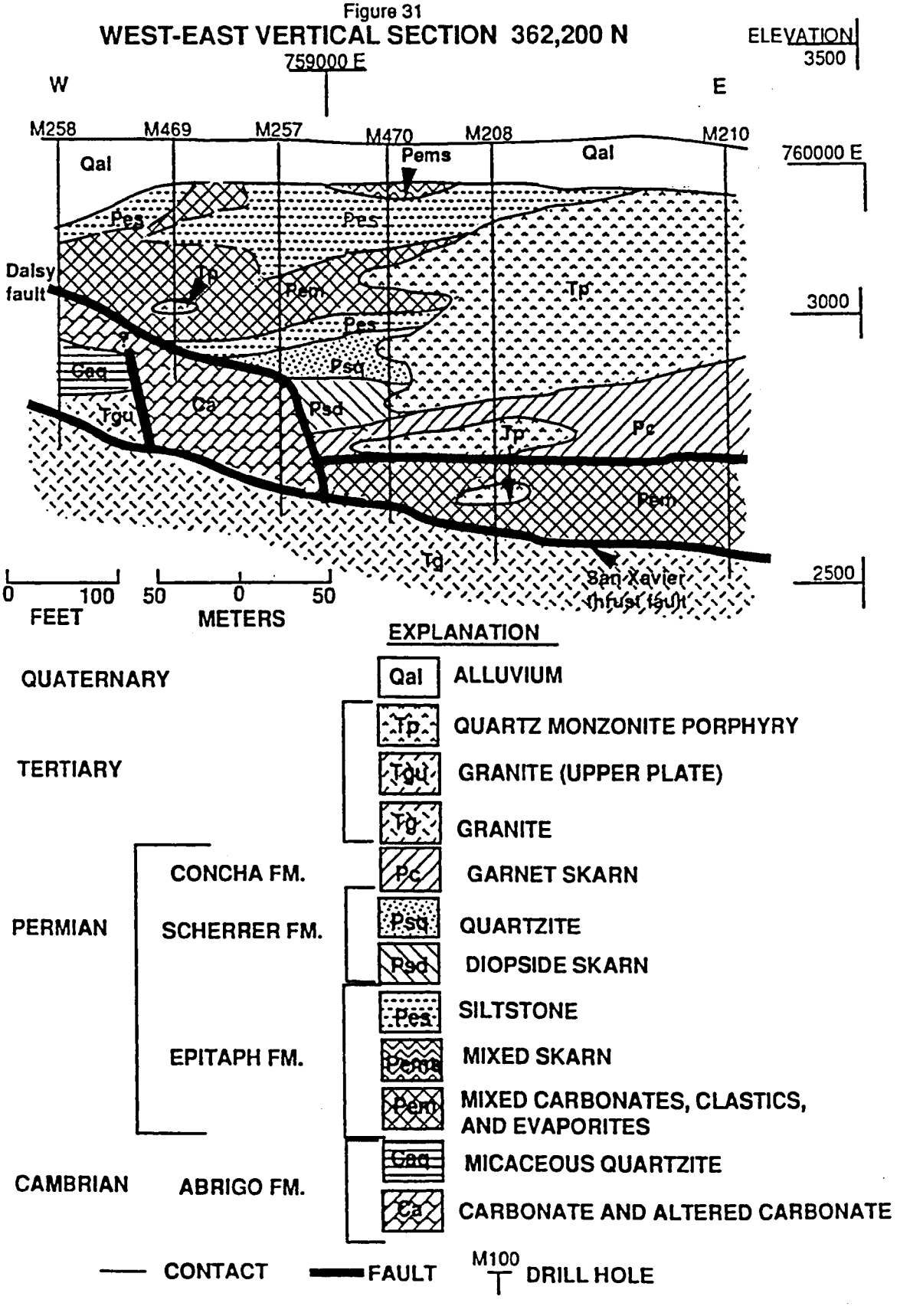
WEST-EAST VERTICAL SECTION 362,200 N
ELEVATION
3500
759000 E
W
E
M258
M469
M257
M470
M208
M210
760000 E
Qal
Pems
Qal
Pes
Pes
Dalsy fault
Tp
Pem
Tp
3000
Pes
?
Psq
Ceq
Ca
Tgu
Psd
Tp
Pc
Pem
Tg
San Xavier thrust fault
2500
0
100
50
0
50
FEET
METERS
EXPLANATION
QUATERNARY
Qal
ALLUVIUM
Tp
QUARTZ MONZONITE PORPHYRY
TERTIARY
Tgu
GRANITE (UPPER PLATE)
Tg
GRANITE
CONCHA FM.
Pc
GARNET SKARN
PERMIAN
SCHERRER FM.
Psq
QUARTZITE
Psd
DIOPSIDE SKARN
Pes
SILTSTONE
EPITAPH FM.
Pems
MIXED SKARN
Pem
MIXED CARBONATES, CLASTICS, AND EVAPORITES
Ceq
MICACEOUS QUARTZITE
CAMBRIAN
ABRIGO FM.
Ca
CARBONATE AND ALTERED CARBONATE
CONTACT
FAULT
M100
DRILL HOLE

Formation sequences to be emplaced atop the Epitaph Formation, but more likely is a splice or drag fault associated with the San Xavier faulting event, which caused the underlying block to be re-overturned. Below this structure is a sequence of siltstone, siltstone-anhydrite, and altered carbonates of the Epitaph Formation. This sequence has a maximum thickness of approximately 45 meters, and is underlain by the San Xavier fault at an elevation of 2300 to 2600 feet, dipping shallowly to the east (Figs.29-30). Below the San Xavier fault is Tertiary granodiorite as previously described.

Structural block III

In structural block III, the sequence of Paleozoic rock units is different than in blocks I and II and in the Mission pit. Below the 30-60 meters of Quaternary (?) alluvium, which thins to the south, is a dense black marble unit approximately 100 meters thick. This black marble, thermally altered with little or no visual evidence of hydrothermal alteration, belongs to a Paleozoic unit whose identity has previously been unknown. This unit is fault-bounded to the east, west, and below. To the east is a high-angle normal (?) fault which dips approximately 55° E (Figs. 24-26, 29, 30, 32), emplacing carbonates, altered carbonates, and siltstone of the Epitaph Formation against the black marble. To the west, at an uncertain distance due to lack of drill hole or outcrop data,

this block is bounded by the Daisy fault (Fig. 21). The black marble is underlain, apparently on fault contact, by Epitaph Formation mixed skarn and siltstone, or by the quartz monzonite porphyry intrusive. The intrusive cuts off the block to the south and east.

Black marble which appears to be from the same unit as that in structural block III is also found in the southern portion of the Mission Complex pit (the old Pima pit) in small fault-bounded blocks ranging in elevation from approximately 2400 to 2200 feet. Unpublished studies commissioned by ASARCO in the mid-1980s found no index fossils or other features that would allow identification of this unit, and up until now, ASARCO geologists have had nothing upon which to base a unit classification. My neural networks study included samples from two drill holes which intersect this unit, M466 and M473 (Fig. 2), as well as three samples from the blocks found in the old Pima pit. The neural networks classified samples from both of these drill holes, as well as those from Pima, as belonging to the Rainvalley Formation. This will be discussed more fully in the results section on the neural networks, but in summary, this classification is tentatively accepted as correct.

The east-bounding fault, which emplaced Epitaph Formation rocks to the east against Rainvalley Formation rocks to the west, must predate the quartz monzonite porphyry intrusion,

Figure 32

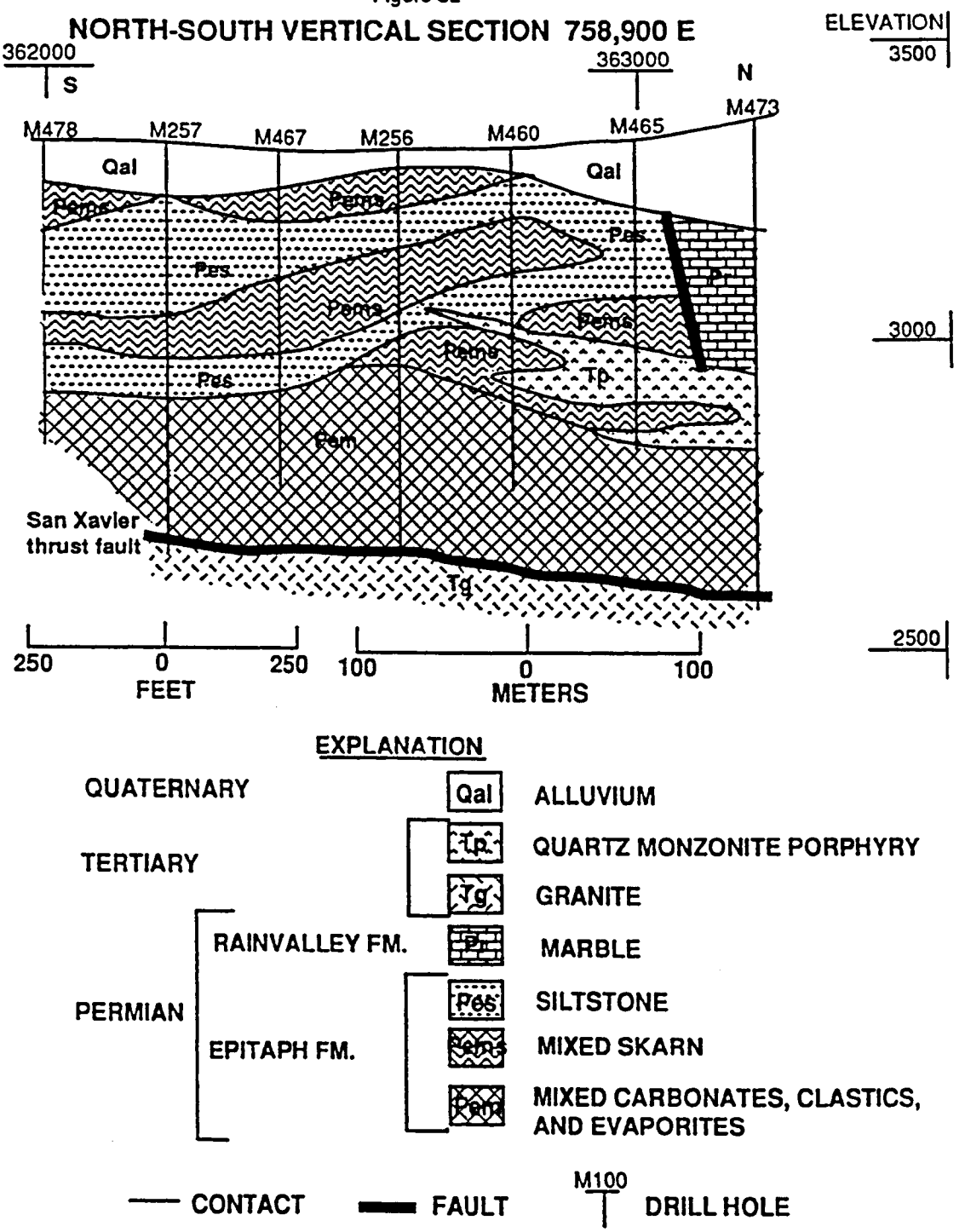
NORTH-SOUTH VERTICAL SECTION 758,900 E
ELEVATION
3500
3000
2500
362000
S
363000
N
M473
M478
M257
M467
M256
M460
M465
Qal
Qal
Penps
Pems
Pes
Pes
Pems
Pems
Pems
Pems
Tp
Pes
Pem
San Xavier
thrust fault
Tg
250
0
250
FEET
100
0
100
METERS
EXPLANATION
QUATERNARY
Qal
ALLUVIUM
TERTIARY
Tp
QUARTZ MONZONITE PORPHYRY
Tg
GRANITE
RAINVALLEY FM.
Pr
MARBLE
PERMIAN
Pes
SILTSTONE
EPITAPH FM.
Pems
MIXED SKARN
Pem
MIXED CARBONATES, CLASTICS, AND EVAPORITES
CONTACT
FAULT
M100
DRILL HOLE

since the underlying porphyry is not faulted. Also, the intrusion apparently caused an unknown amount of lateral movement in the overlying block, since the fault does not continue in the meta-sediments below the porphyry (Figs. 29-30, 32).

In structural block III, as in blocks I and II, the quartz monzonite porphyry intrusion has a sill-like configuration, dipping at low angles to the north, thickening and thinning irregularly, with an average thickness of 50-60 meters (Figs. 29-30). Below the porphyry sill, the rocks consist of mixed garnet-diopside skarn, siltstone and siltstone-anhydrite, and carbonates of the Epitaph Formation. The porphyry-Epitaph contact appears to be the splice or drag fault, described in the section on structural block II, associated with the Tertiary San Xavier fault that apparently re-overturned the Epitaph Formation rocks below. The Epitaph Formation sequence varies from approximately 100 meters thick in the south of the block at 363,000 N, to only 15 meters thick in the north at 363,600 N. This is due to the shallow northward dip of the quartz monzonite intrusion, and the nearly flat San Xavier fault, which cuts off the Epitaph Formation sequence at between 2610 and 2650 feet elevation. Below the San Xavier fault is Tertiary (Ruby Star?) granodiorite or granite.

Structural block IV

Structural block IV is in the far west of the project area, beneath and to the west of the Daisy fault (Figs. 21, 25-27, 31). The Paleozoic sequence in this block is different than that of the other structural blocks and the Mission sequence, consisting of a carbonate/altered carbonate unit which in M258 (Fig. 31) consists of marble, silty marble, and altered marble, underlain by micaceous quartzite. The lithology of the units indicates that the predominant unit to the west and beneath the fault is the Abrigo Formation. Within the Paleozoic section such sequences occur only in the Abrigo and Epitaph Formations. The Epitaph is not known to contain any quartzite beds but does contain abundant evaporites not found in the drill core. Second, within the metamorphosed carbonate, thin bands of garnet which occur marginal to thin siltstone beds within the limestone commonly appear. This feature, informally referred to by Mission geologists as "banded gar-marble" can also be seen on hills to the south of the project area where the Abrigo Formation outcrops. Micaceous quartzite from the lower Abrigo Formation can also be found on these hills. Therefore, my tentative conclusion, backed up by some neural network confirmation, is that the sequence of rocks found in the drill holes to the west and below the Daisy fault is the Abrigo Formation. The sequence of carbonates and altered carbonates is from the middle Abrigo siliciclastic-

carbonate unit, and the underlying micaceous quartzite is from the lower Abrigo siliciclastic mudstone. In drill hole M258 (Fig. 31), below the micaceous quartzite, an upper plate granite 15 meters in thickness occurs. The granite and overlying micaceous quartzite units do not occur in holes to the east (M469 and M257) and north (M462), leading to the conclusion that a previously unrecognized fault must exist (Fig. 31). The exact attitude of this fault is unknown, since it does not intersect and drill holes and does not intersect the surface, being cut off by the Daisy fault. Below the granite in M258 and lower-middle Abrigo Formation elsewhere, at an elevation of between 2700 and 2500 feet is the San Xavier fault (Figs. 27, 28, 31), dipping approximately 10° to the east. Below the San Xavier fault is the previously described Tertiary granite or granodiorite.

Drill hole data indicates that in this area, the Daisy fault strikes approximately N10W and dips between 30° and 70° NE.

RESULTS

SEDNORM

Unfortunately, the SEDNORM program proved to be of minimal value in this endeavor. Although the program worked well, there was not enough variation in the major mineral and element compositions to be useful in identifying the unknowns. As the ternary diagrams (Figs. 5-13) show, there is a great deal of overlap between formations in the fields in which the major element and mineral compositions plot. Also, the internal variations within some of the formations is high enough that their average compositions (Table 10) can not be considered representative of the formation, thus making them unsuitable for comparison to the unknowns. Although several formations have features which can distinguish them, such as the Escabrosa Group plots (Fig. 7), in which all samples plot at ≥90 % CaO, other formations have samples which also plot in the >90 % CaO range, thus making the plots of little use in identifying unknowns. Similarly, some of the Epitaph Formation (Fig.10) samples plot with a higher SiO_2 value than the other formations, but the middle and lower end of the SiO_2 range from the Epitaph Formation samples is within the SiO_2 ranges of several other formations.

After studying the both ternary plots and Table 10, I could find no major mineral or element values that are distinctive

enough for a single formation to make them useful in identifying the unknown metasediments at Mineral Hill.

NEURAL NETWORKS

Known lithologic units

Using three-fifths of the samples for training, several formations were consistently classified with 100 percent accuracy. These were the Escabrosa, Martin, Rainvalley, and Colina formations. The Abrigo and Horquilla formations, however, required a fourth training sample to achieve 100 percent accuracy.

In the case of the Horquilla, the one sample that was being mis-classified was added to the training set. This sample was then correctly learned as Horquilla, giving 100 percent accuracy for the formation. However, adding this fourth Horquilla sample to the training set inexplicably caused one of the three Scherrer formation samples, which previously had been classified correctly, to be mis-classified. This error was remedied by adding the third Scherrer sample to the training set.

The neural network mis-classified both of the Abrigo formation samples not used for training. Adding one of the two samples to the training set caused both to be classified correctly, giving 100 percent accuracy for the Abrigo formation samples.

That the two Concha formation samples that were mis-classified by the network were classified as Rainvalley formation was not surprising since the formations are geologically and, as the study showed, geochemically similar. Early attempts at network training, using different elemental suites, had shown this propensity for mis-classification between the Concha and Rainvalley formations. Since the elemental values for the mis-classified samples appeared to be typical of all the Concha formation samples, no attempt was made to correct this mis-classification before running the unknowns through the network for classification. This will be addressed more fully in the Discussion section.

The remaining known sample mis-classified by the neural network was from the Epitaph formation. All attempts to correct this mis-classification, including adding a fourth training sample, failed. Reasons for this will be considered in the Discussion section.

One of the shortcomings of the neural networks is its inability to communicate exactly which elements, groups of elements, or elemental ratios were the most important in learning the training set. This leaves the user unsure of why the network mis-classified a given sample.

Unknowns

Although for some units the neural network classifications of the unknowns can be accepted with a high degree of

confidence, its overall success was far below what I had hoped for. Possible reasons for this will be considered in the Discussion section.

The neural network had two fundamental types of errors: 1) confusion between units that are geologically, and as it turned out, geochemically similar, and 2) mis-classification based on local geochemical variation within a unit, commonly caused by metamorphism. The first error type was noted in the training sessions: as previously reported, the network had difficulty distinguishing between the upper Permian Concha and Rainvalley Formations. This error also occurred in the unknown samples from drill-hole M-473. Two analyzed samples from different depths within the same apparent lithologic unit were assigned different classifications, one Concha and one Rainvalley. However, this error was neither surprising nor unexpected, since, as previously stated, these units are geologically and geochemically similar. Also, this did not impede and indeed helped to confirm the classification of this unit as the Rainvalley Formation, since the neural networks never mis-classified other knowns as Concha or Rainvalley, and the hand samples collected from these intervals, which are dense, black marble, more closely approximate descriptions of the Rainvalley Formation than the Concha or any other formation. Also, drill-hole M-466, which contained four samples in the same stratigraphic horizon, universally

classified all four samples as Rainvalley. Further confirmation comes from three samples collected from within the old Pima pit in black marble which appears visually and geochemically nearly identical to the samples from drill holes M473 and M466. The neural network identified two of these samples as being Rainvalley and one as being Concha, therefore I find the Rainvalley to be tentatively acceptable classification.

The second and much more common type of error, mis-classification based on local geochemical variation within a formation, was first noted in this study from samples collected within the Mission pit. Four samples were collected and analyzed from different elevations on the north face of the "marble knob", which is believed to be the topographically lower but stratigraphically higher portion of the Concha Formation (Jansen, 1982; Cummings, pers. comm.,1991). One sample of light-colored coarse-grained marble collected near the top of the knob was classified as Concha. A similar sample collected approximately 50 meters lower was classified as Rainvalley. Two samples were also collected near the base of the knob (50 meters lower) in marble that contains alternating bands 3-20 centimeters thick, of light-colored coarse-grained, and dark grey to black fine-grained marble, one sample each from the light and dark bands. The light-colored sample was classified, as expected, as being

from the Concha Formation. However, the dark-colored sample was mis-classified as being from the Martin formation. A similar situation occurred to the east of the "marble knob" where faulting has made unit identification less certain but where the unit is still believed to be Concha Formation. A comparison of elemental values from the Concha, the Martin, and the samples collected from the "marble knob" and to the east leads to the conclusion that lowered SiO_2 and MnO values in the dark-colored samples were likely the reason that the samples were classified as Martin Formation rather than the correct Concha classification, since in this case most of the other elemental values of the unknowns fall within acceptable ranges of both formations.

Mineral Hill area unknowns

Based on cross-section and lithologic data, many of the unknowns from the Mineral Hill project area can be classified with a high degree of certainty as being from a particular formation. These fall within structural blocks I and III (Fig. 13) to the east of the major high-angle normal faults. The previously discussed samples from drill-holes M466 and M473 (Fig.2) are accepted as belonging to the Rainvalley Formation. However, within block III, sample 63 from drill-hole M473 was mis-classified as Abrigo Formation by the neural networks when cross-section and drill-log data indicate that it is almost certainly from the Epitaph Formation. Comparison

of the geochemical analysis of this sample to the knowns from the Abrigo and Epitaph Formations indicate that the mis-classification was caused by CaO, As, K_2O, MgO, and MnO values more in line with those from the Abrigo than the Epitaph.

Within structural block I, "unknown" samples 64-67 from drill-hole M468 can also be classified with a high degree of certainty. Sample 64 was most probably correctly classified as Rainvalley, being from a thin fault slice emplaced upon the Epitaph Formation, apparently associated with the faulting which emplaced Rainvalley atop of Epitaph in structural block III. This feature will be discussed in the chapter on the geology of the Mineral Hill area. Samples 65, 66, and 67, however, were incorrectly classified. Samples 65 and 66 were classified as being from the Abrigo Formation, and sample 67 as being from the Rainvalley Formation. All three are almost certainly from the Epitaph Formation. Sample 65 was apparently mis-classified due to high Fe_2O_3 and Ni contents, which although higher than that found in either the Abrigo or Epitaph analyses, is closer to the range of the Abrigo analyses, and also due to high MnO content which is in the Abrigo range, higher than that found in the Epitaph. Sample 66 was apparently mis-classified due to high MnO and Ni content, as sample 65 was, and also due to high As and low MgO contents more in line with the Abrigo Formation analyses than the Epitaph. Sample 67 was incorrectly classified as

Rainvalley, apparently due to its high CaO and SiO_2 and low Al_2O_3 and K_2O contents that more closely fit Rainvalley analyses than Epitaph.

Within structural block IV, to the west of the Daisy fault (Figs. 21, 24-27, 31), the identity of the unknowns is less certain based on cross-section and lithologic data. However, neural network analyses plus lithologic features described in the section on the geology of the Mineral Hill area, structural block IV, lead to the conclusion that this sequence is from the lower and middle Abrigo Formation.

Geochemical analyses were performed on samples from three drill holes in block IV, drill holes M461, M462, and M476 (Fig. 2). In M461, the five samples from top to bottom were classified as Rainvalley, Concha, Epitaph, Martin, and Martin Formations. Stratigraphic data indicates that the upper three samples are from above the Daisy fault, from the Epitaph formation, and the lower two are below the fault, from the Martin Formation. Sample 75 was apparently mis-classified due to CaO values more in line with those of the Rainvalley than the Epitaph, and also Lu and Sm values in the range found in the Rainvalley, lower than that of the Epitaph. However, many values were closer in range to the Epitaph than the Rainvalley, notably Al_2O_3, MgO, and SiO_2, and the network may have assigned this sample to the Rainvalley Formation by default without a high confidence. Sample 76 appears to have

been missed due to ICP Al_2O_3, Sr, and Sm values which more closely approximate those found in the Concha than the Epitaph Formations. Sample 77 was correctly classified as belonging to the Epitaph Formation. Directly below sample 77 was a fault zone (the Daisy fault), and the rocks below I believe to be from the Martin Formation. Samples 78 and 79 were correctly classified as being from the Martin Formation. In drill hole M462, all three samples, numbers 72-74, were classified as Martin Formation. Stratigraphic and geologic data indicates that sample 72 is from the Martin, and samples 73 and 74 are from the underlying Abrigo Formation. Samples 73 and 74 were apparently classified as Martin Formation rather than Abrigo due to CaO values below the range found in the Abrigo training set, as well as high Al_2O_3 and SiO_2 values. In hole M476, the upper two samples, 80 and 81, were correctly classified as Abrigo formation. However, the lower two samples, 82 and 83, were missed, 82 being classified as Concha and 83 as Epitaph. In sample 82 the misclassification was apparently due to low CaO and Sr values and high MgO. In sample 83, low CaO as well as high SiO_2 and K_2O values caused the mis-classification.

Discriminant analyses were run on the unknowns using the direct method, the maximum-minimum f value, and the Mahal distance method to determine how successful discriminant analysis would be in correctly classifying the unknowns. All

three methods were less successful in correctly classifying the unknowns than the neural networks. Neural network analysis correctly classified 15 of the 32 "unknowns" whose formation can be confidently ascertained from geologic and stratigraphic data. The maximum-minimum f value method of discriminant analysis correctly classified 7 of the 32, the direct method correctly classified 8 of the 29, and the Mahal distance method correctly classified 6 of the 32 unknowns. More importantly, the only samples correctly classified by the discriminant analyses came from the Rainvalley and Concha Formations, while the neural networks were successful in correctly classifying not only the Rainvalley and Concha samples, but also had some success classifying Epitaph and Abrigo formation samples correctly.

GEOLOGY OF THE MINERAL HILL AREA

Structural block I contains the same sequence found in the Mission pit, with a few notable differences. The contact between the Triassic Rodolfo Formation argillite and the underlying Permian Epitaph Formation appears from its attitude to be a fault contact (Fig. 23), although this is uncertain. In the Mission pit, the contact is a disconformable one due to erosion/nondeposition following the overturning of the Permian section until the time the Rodolfo Formation was deposited. Also, the Epitaph Formation sequence is thicker (approximately

90 meters)
in the Mineral Hill area than the Epitaph sequence in the Mission pit, 75 meters as reported by Jansen (1982). The units that underlie the Epitaph Formation rocks in Mission, the Scherrer and Concha Formations, do not exist in this structural block due to the San Xavier fault, which is higher up in the section westward, dipping at a low angle to the east.

In structural block II, the sequence is also similar to that in the Mission pit, except that the Rodolfo Formation does not exist, Quaternary (?) alluvium directly overlying the Epitaph Formation or the quartz monzonite porphyry. The three Permian units occur in their expected sequence, Epitaph overlying Scherrer followed by Concha Formation; however, the Concha Formation is much thinner than in Mission pit, truncated downward by the roll-over fault which disrupts the normal sequence and emplaced Epitaph Formation rocks below the Concha Formation.

In structural block III, the sequence is different from that found in the Mission pit. The uppermost unit below the alluvium, a dense black marble, is not found in the Mission pit except in small fault-bounded blocks deep in the southern portion of the pit (old Pima). Neural network analysis identified this unit as being Rainvalley Formation, an acceptable conclusion, since the neural networks learned the

Rainvalley Formation training samples without trouble, and since the Rainvalley Formation typically contains dark gray to black marble where it outcrops throughout southern Arizona. Below the Rainvalley is either a fault contact with the Epitaph Formation, or an intrusive contact with the quartz monzonite porphyry. The faulting episode that placed the Rainvalley in its present stratigraphic position predated the intrusion of the quartz monzonite, as the porphyry is not faulted. Some lateral movement is also indicated, as the major fault between the Rainvalley and Epitaph Formations at the eastern edge of structural block III (Figs, 21, 24-26) does not continue beneath the porphyry intrusion. The timing of this lateral movement is unknown. Emplacement of Rainvalley Formation rocks against the Epitaph Formation indicates a minimum vertical displacement of 425 meters along this structure. Below the porphyry intrusion the sequence is either typical of the Mission sequence or disrupted by the shallow splice or drag fault with Epitaph Formation rocks below.

Structural block IV, west of and below the Daisy fault, contains a sequence of rocks belonging to the Martin Formation, the underlying Abrigo Formation, and upper plate Tertiary granitic rocks. The Martin Formation rocks consist of metamorphosed magnesian carbonates, silty carbonates, and serpentinized carbonates. The Abrigo Formation rocks consist

of a metamorphosed sequence of carbonates, silty carbonates, and altered carbonates belonging to the lower-middle Abrigo Formation, locally underlain by micaceous quartzite (Fig. 31) of the lower Abrigo. In the Martin Formation, calc-silicate alteration products are generally serpentine, and garnet is the predominant alteration product in the Abrigo Formation.

With the emplacement of Abrigo Formation rocks to the west against Epitaph Formation to the east, the minimum displacement on the Daisy fault must be over 1000 meters.

DISCUSSION

SEDNORM

The Sednorm analyses were of little or no use in the attempt to classify the unknowns by formation, largely due to the fact that the analyses used only the major elements to determine normative mineral compositions, and the variability within formations and the overlap between formations was too great. The nature of the samples, all carbonate rocks even if the formation they were collected from is known to contain clastics or evaporites, of necessity caused the great amount of overlap between formations, rendering the Sednorm approach unusable for this study. The samples were collected primarily for the neural networks research, hopefully allowing me to identify unknown carbonate units within the project area, and the intentional similarity of major element compositions in the samples doomed the Sednorm analysis from the beginning. Nevertheless, this study was useful in testing the ability of the Sednorm program to perform its stated function, determining normative mineral compositions quickly and easily, and in this it performed extremely well. In a study that required only percentages of major minerals, this program would be extremely valuable.

NEURAL NETWORKS

The overall success of the neural networks in classifying the lithologic units was disappointing, correctly classifying 40 of 44 knowns (91 %) and 18 of 32 of the unknowns (56 %) whose formation classification can be confidently ascertained by geologic means. This was chiefly due to the fact that, due to funding constraints, a very limited training set was available, far less than previous neural network researchers have deemed appropriate. Since all samples were carbonate rocks, many assay values overlap in the different formations, and a larger training set might have defined typical elemental value ranges more precisely, thus giving better results.

Of the known samples that were missed, the network confusion between the Concha and Rainvalley Formations can be explained by their geochemical similarity. The other formations with which the network had the most trouble, the Abrigo and Epitaph Formations, are extremely heterogeneous in nature, especially in comparison with the other formations, and possibly it is not realistic to expect the neural networks to be able to establish a distinct pattern of elemental values for these formations in order to correctly classify them. The fact that the neural networks often mis-classified Abrigo "unknowns" as Epitaph and vice-versa lends credence to the idea that the heterogeneity of the two formations is too great for the networks to overcome without a much larger training

set, if at all. The neural networks also often mis-classified both Abrigo and Epitaph formation samples as Martin Formation, probably due to overlap of elemental values and the heterogeneity of the Abrigo and Epitaph Formations.

One mis-classification whose cause is puzzling was previously described: when a fourth Horquilla Formation sample was added to the training set to give the network 100% accuracy for the Horquilla, the network then mis-classified the one Scherrer formation sample not used for training. If the network had mis-classified it as Horquilla Formation, this may have been explainable, but it was mis-classified as belonging to the Colina Formation, and I have no reasonable explanation as to why this occurred.

Another of the chief causes for mis-classification of the unknowns is the condition of the samples themselves: all of these rocks have undergone metamorphism. The metasedimentary unknowns from the Mineral Hill area are generally enriched in Cu, Fe, Mo, Zn, Pb, As, Sr, and W in comparison to the sedimentary and metasedimentary knowns used for training the neural networks. Known samples were purposely collected within the district when possible to minimize elemental variation, and the metallic elements were intentionally omitted from the elemental suite given to the neural networks for classification. While care was taken to select samples that visually appear to have undergone only thermal

alteration, the possibility of hydrothermal alteration with addition and/or subtraction of mobile elements is a possibility, and this would almost certainly cause severe difficulty in classification for the neural networks. Many elements which upon inspection of the results appeared to have caused the mis-classifications are mobile elements, such as Si, Mn, Mg, As, and Sr.

GEOLOGY OF THE MINERAL HILL AREA

The major geologic and stratigraphic differences that exist between the Mission pit and the Mineral Hill area are the result of three major faults. These are the high angle normal (?) fault that emplaced Rainvalley Formation rocks above and to the west of the Epitaph Formation rocks in structural block III, the splice or drag fault which caused Epitaph Formation rocks to be re-overturned and emplaced below Scherrer and Concha Formation rocks in structural blocks I, II, and III, and the Daisy fault, which placed rocks of the Abrigo and Martin Formations directly below and to the west of Epitaph Formation rocks. Of these, the splice or drag fault appears to be contemporaneous with the San Xavier fault, causing a small block to detach and overturn during the movement of the allocthonous upper plate of the San Xavier fault. The timing of the other two faulting episodes in the Mineral Hill project area is unknown, although post-mineralization movement along

the Daisy fault is probable.

The Paleozoic section is thinner in the Mineral Hill area than to the east due to the dip of the San Xavier fault, and this, along with the offset of Paleozoic strata along the Daisy fault, causes the stratigraphically lower ore-bearing units in the Mission pit, the Concha and Scherrer Formations, to be much less important in terms of ore mineralization. Conversely, a much greater thickness of the Epitaph Formation exists in the Mineral Hill area than to the east, therefore a much larger percentage of ore mineralization exists in the Epitaph Formation than in the other formations found in the Mineral Hill area.

CONCLUSIONS

NEURAL NETWORKS

Neural networks appear to be a tool that can have great success in future geochemical applications and research. The problems that caused the lack of success in this study could be easily overcome by (1) providing a more adequate training set, and (2) by providing the networks with a set of unknowns to be classified which have not undergone the degree of metasomatic alteration of those used in this investigation. The considerable success that the networks did achieve, especially in learning the training set, is a hopeful indication that future researchers attempting this type of application should be able to expect a very high probability of success.

GEOLOGY OF THE MINERAL HILL AREA

Although many of the rock units in the Mineral Hill project area and in the Mission pit are the same, the overall geology/stratigraphy is quite different, primarily due to the major faults that exist in the area. The westward up-dip of the San Xavier fault causes the Paleozoic section to be progressively thinner to the west, and the resulting missing strata, especially the Concha Formation, are an important factor in terms of future mining operations as it is one of

the primary hosts to high-grade copper ore at the Mission Complex. The flat fault believed to have caused a roll-over of a small basal piece of the allocthonous block during the San Xavier faulting events also cuts off the Concha Formation, replacing it with a re-overturned section of Epitaph Formation rocks.

The other two major faults in the project area, the high-angle structure that is the eastern boundary of structural block III and the Daisy fault, both caused rock units not present in significant volume in the Mission pit to be emplaced in the Mineral Hill area. In the case of the unnamed high-angle structure east-bounding structural block III, Upper Permian rocks of the Rainvalley Formation were emplaced adjacent to rocks of the Epitaph Formation, a vertical displacement of at least 425 meters. The Daisy fault emplaces rocks of the Cambrian Abrigo Formation and Devonian Martin Formation below and west of the Epitaph Formation, a displacement of 1000 meters minimum.

Another major difference between the Mineral Hill area and the Mission pit rocks may or may not have been caused by faulting. One of the major hosts to ore at the Mission Complex by volume, the Triassic Rodolfo Formation argillite, is missing in the Mineral Hill area except for a small fault (?) wedge in structural block I (Fig. 21). Whether this omission is due to erosion predating the deposition of the

Quaternary alluvium or by an unrecognized faulting episode that removed the section is unknown.

The question of whether the Daisy fault may be correlated with the Twin Buttes fault 10 kilometers to the south is a complex one. The Paleozoic strata at Twin Buttes are vertical, while at Mission they are overturned in a more horizontal configuration, although deformed into broad, gentle, NW-trending folds. The folding and overturning of the units at Mission is believed to have occurred before the major faulting episodes. The strike of the Daisy is approximately 90° different from the Twin Buttes fault, which strikes N60E-N70E while the Daisy strikes N10W-N20W, and the dip is also much different on these two faults, the Twin Buttes fault being vertical while the Daisy dips between 30° and 70°NE. The change in attitude of the bedding due to the folding could in large part account for these differences, and attitude differences could also be due to movement of the San Xavier fault. Despite these major differences, the fact that vertical displacement along these two faults is essentially identical as well as their similar locations in the west of the respective orebodies are strong arguments for the correlation of the Daisy fault as the upsection continuation of the Twin Buttes fault. I believe that this hypothesis is true, although it may be impossible to prove.

REFERENCES

Anderson,J., and Rosenfeld, E., 1989, Neurocomputing: Foundations of Research: M.I.T. Press.

Armstrong, A.K., 1962, Stratigraphy and paleontology of the Mississippian System in southwestern New Mexico and southeastern Arizona: New Mexico Bureau of Mines and Mineral Resources Memoir 8, 95 p.

Barter, C.F., and Kelley, J.L., 1982, Geology of the Twin Buttes Mineral Deposit, Pima mining district, Pima County, Arizona: in Titley, S.R., ed., Advances in the Geology of Porphyry Copper Deposits, Southwestern North America: University of Arizona press, p. 407-431.

Blakey, R.C., and Knepp, R., 1989, Pennsylvanian and Permian Geology of Arizona: in Jenney, J.P., and Reynolds, S.J., eds., Geologic Evolution of Arizona: Arizona Geological Society Digest 17, p. 313-347.

Bryant, D.L., 1968, Diagnostic characteristics of the Paleozoic formations of southeastern Arizona, in Titley, S.R., ed., Southern Arizona Guidebook III: Tucson, Arizona Geological Society, p. 33-47.

Bryant, D.L., and McClymonds, N.E., 1961, Permian Concha Limestone and Rainvalley Formation, southeastern Arizona: AAPG Bulletin, v. 45, p. 1324-1333.

Carpenter, G., and Grossberg, S., 1987, ART2: self-organization of stable category recognition codes for analog input patterns: Applied Optics, 26, p. 4919-4930.

Caudill, M., 1988, Neural Networks Primer, Part IV. AI Expert, August, p. 61-67.

Cohen, D., and Ward, C.R., 1991, Sednorm- A program to calculate a normative mineralogy for sedimentary rocks based on chemical analyses: Computers and Geosciences Vol. 17, No. 9, p. 1235-1253.

Cooper, J.R., 1960, Some geologic features of the Pima mining district, Pima County, Arizona: U.S. Geologic Survey Bulletin 1112-C, p. 63-101.

Cooper, J.R., 1971, Mesozoic stratigraphy of the Sierrita Mountains, Pima County, Arizona: U.S. Geologic Survey Prof. Paper 658-D, 42 p.

Dayhoff, J., 1989, Neural Network Architectures: Van Nostrand Reinhold.

Einaudi, M.T., 1982, Description of skarns associated with porphyry copper plutons, in Titley, S.R., ed., Advances in Geology of Porphyry Copper Deposits, Southwestern North America: University of Arizona press, p. 139-181.

Gale, R.E., 1965, Geology of the Mission Copper Mine, Pima mining district, Arizona: unpublished Ph.D. Dissertation, Stanford University, 140 p.

Geman, S., Bienenstock, E., and Doursat, R., 1992, "Neural networks and the bias/variance dilemma": Neural Computation, Vol. 4, p.1-58.

Gilluly, J., Cooper, J.R., and Williams, J.S., 1954, Late Paleozoic stratigraphy of central Cochise County, Arizona: U.S. Geologic Survey Prof. Paper 266, 49 p.

Hayes, P.T., 1978, Cambrian and Ordovician rocks of southeastern Arizona and southwestern New Mexico: New Mexico Geological Society Guidebook, 29th Field Conference, p. 165-173.

Hayes, P.T., and Cone, G.C., 1975, Cambrian and Ordovician rocks of southern Arizona and New Mexico and westernmost Texas: U.S. Geological Survey Prof. Paper 873, 98 p.

Hayes, P.T., and Landis, E.R., 1965, Paleozoic stratigraphy of the southern part of the Mule Mountains, Arizona: U.S. Geological Survey Bulletin 1201-F, 43 p.

Hecht-Nielsen, R., 1990, Neurocomputing: Addison-Wesley Publ. Co.

Himes, M.D., 1973, Mineralization and alteration at Pima mine- a complex porphyry copper deposit: AIME Trans., v. 254, p. 166-174.

Jansen, L.J., 1982, Stratigraphy and structure of the Mission copper deposit, Pima mining district, Pima County, Arizona: in Titley, S.R., ed., Advances in Geology of Porphyry Copper Deposits, Southwestern North America: University of Arizona press, p. 467-474.

Kohonen, T., 1988a, Self-organization and Associative Memory: Springer-Verlag New York, Inc.

Kohonen, T., 1988b, "Learning Vector Quantization": Abstract of the First Annual INNS Meeting, Boston, MA, p. 303.

Lapedes, A., and Farber, R., 1987, Nonlinear signal processing using neural networks: prediction and system modeling: Los Alamos Report LA-UR-87-2662.

Luepke, G., 1971, A re-examination of the type section of the Scherrer Formation (Permian) in Cochise County, Arizona, in McCullough, E.J., ed.,: Tucson, Arizona Geological Society Digest, v. 9, p. 245-257.

Middleton, L.T., 1989, Cambrian and Ordovician depositional systems in Arizona: in Jenney, J.P., and Reynolds, S.J., Geologic Evolution of Arizona: Tucson, Arizona Geological Society Digest 17, p. 273-286.

Norby, R.D., 1971, Conodont biostratigraphy of the Mississippian rocks of southeastern Arizona: Tempe, Arizona State University, unpublished M.S. thesis, 195 p.

Pao, Y., 1989, Adaptive Pattern Recognition and Neural Networks: Addison-Wesley Publ. Co.

Parker, D.B., 1982, "Learning Logic", Invention Report S81-64, File 1, Office of Technology Licensing, Stanford University.

Poulton, M., and Zaverton, K., 1992, Comparison of neural network paradigms for classification of TM images, 23rd International Symposium on the Application of Computers and Operations Research in the Minerals Industry, p. 37-46.

Ransome, F.L., 1904, Geology and ore deposits of the Bisbee Quadrangle, Arizona: U.S. Geological Survey Prof. Paper 21, 168 p.

Rumelhart, D., Hinton, G., and McClelland, J., 1986, A general framework for parallel distributed processing, in Rumelhart, D., and McClelland, J., Eds., Parallel distributed processing, Vol. 1: M.I.T. Press, p. 45-76.

Shafiqullah, M., and Langlois, J.D., 1978, The Pima mining district, Arizona- A geochronologic update: Land of Cochise, New Mexico Geologic Society, 29th Field Conference Guidebook, p. 321-327.

Soulie, F., Gallinari, P., Le, C., and Thiria S., 1987, Evaluation of neural network architectures on test learning tasks: 1st International Conference of Neural Networks, IEEE, p. 653-660.

Tiechert, C., 1965, Devonian rocks and paleogeography of central Arizona: U.S. Geological Survey Prof. Paper 464, 181 p.

Wasserman, P., 1989, Neuralcomputing: Theory and Practice: Van Nostrand Reinhold.

Werbos, P., 1974, Beyond regression: new tools for prediction and analysis in the behavioral sciences, unpublished Ph.D. Dissertation, Harvard University.

Wilt, J.C., 1969, Petrology and stratigraphy of the Colina Limestone (Permian) in Cochise County, Arizona: University of Arizona, Tucson, unpublished M.S. thesis, 117 p.

11 33976 MAIN: TH
10 U/A 02/09/95 5601-